



© Copyright by Preston J. Hartzell 2016

All Rights Reserved

**ACTIVE AND PASSIVE SENSOR FUSION FOR TERRESTRIAL  
HYPER SPECTRAL IMAGE SHADOW DETECTION AND RESTORATION**

A Dissertation

Presented to

the Faculty of the Department of Civil and Environmental Engineering

University of Houston

In Partial Fulfillment

of the Requirements for the Degree

Doctor of Philosophy

in Geosensing Systems Engineering and Sciences

by

Preston J. Hartzell

May 2016

**ACTIVE AND PASSIVE SENSOR FUSION FOR TERRESTRIAL  
HYPERSPPECTRAL IMAGE SHADOW DETECTION AND RESTORATION**

---

Preston J. Hartzell

Approved:

---

Chair of the Committee  
Craig L. Glennie, Ph.D.  
Assistant Professor  
Civil & Environmental Engineering

Committee Members:

---

Ramesh L. Shrestha, Ph.D.  
Hugh Roy & Lillie Cranz Cullen  
Distinguished Professor  
Civil & Environmental Engineering

---

Hyongki Lee, Ph.D.  
Assistant Professor  
Civil & Environmental Engineering

---

Shuhab D. Khan, Ph.D.  
Professor  
Earth & Atmospheric Sciences

---

Christopher E. Parrish, Ph.D.  
Associate Professor  
Civil & Construction Engineering  
Oregon State University

---

Suresh K. Khator, Ph.D.  
Associate Dean  
Cullen College of Engineering

---

Craig L. Glennie, Ph.D.  
Geosensing Systems Engineering &  
Sciences Program Director

## ACKNOWLEDGEMENTS

*~ those who made it possible ~*

Craig Glennie

David Finnegan

Ramesh Shrestha

*~ those who pointed in the right direction ~*

Brian Naberezny

Charles Ghilani

Vernon Hartzell

*~ fellow pioneers of the GSES graduate program ~*

Darren Hauser, Arpan Kusari, Zhigang Pan

Hongzhou Wang, Ting Yuan, Xiao Zhang

*Dedicated to my wife, Kari, for the courage to leave one life behind to begin another,*

*with gratitude to my children, Jonathan and Lillie, for their sacrifice of time.*

**ACTIVE AND PASSIVE SENSOR FUSION FOR TERRESTRIAL  
HYPERSPPECTRAL IMAGE SHADOW DETECTION AND RESTORATION**

An Abstract

of a

Dissertation

Presented to

the Faculty of the Department of Civil and Environmental Engineering

University of Houston

In Partial Fulfillment

of the Requirements for the Degree

Doctor of Philosophy

in Geosensing Systems Engineering and Sciences

by

Preston J. Hartzell

May 2016

## **Abstract**

Acquisition of hyperspectral imagery (HSI) from cameras mounted on terrestrial platforms is a relatively recent development that enables spectral analysis of dominantly vertical structures such as geologic outcrops. Although solar shadowing is prevalent in terrestrial HSI due to the vertical scene geometry, automated shadow detection and restoration algorithms have not yet been applied to this technique. This dissertation investigates the fusion of terrestrial laser scanning (TLS) spatial information with terrestrial HSI for geometric shadow detection on a vertical outcrop and examines the contribution of radiometrically calibrated TLS intensity, which is resistant to the influence of solar shadowing, to HSI shadow restoration.

The proposed method for shadow detection in the terrestrial HSI leverages an accurately georeferenced, high density point cloud acquired with a TLS sensor to geometrically solve for the presence of shadows in the fused HSI. In contrast to traditional methods applied to airborne imagery, the analysis requires a fully 3D mesh representation of the outcrop rather than a 2.5D surface model. The inclusion of radiometrically calibrated TLS intensity in several existing image shadow restoration techniques is examined, and a direct combination of the active TLS and passive HSI radiometric products proposed and evaluated.

Qualitative assessment of the shadow detection results indicates pixel level accuracy, which is indirectly validated by shadow restoration improvements when sub-pixel shadow detection is used in lieu of single pixel detection. The inclusion of TLS intensity in existing shadow restoration algorithms was found to have a marginal positive influence on restoring shadow spectrum shape, while the proposed combination of TLS intensity with passive HSI

spectra boosts restored shadow spectrum magnitude precision by up to 40%, and band correlation with respect to a truth image by up to 45% compared to existing methods.

The findings demonstrate that sub-pixel shadow detection in terrestrial HSI can be achieved with geometric methods using standard TLS and HSI field collection practices, and the inclusion of TLS intensity can improve restored HSI spectral characteristics. Simulations incorporating multiple laser wavelengths suggest more robust and computationally efficient methods of combining active and passive spectral data for restoring shadow pixel spectra are possible.

# Table of Contents

<b>Abstract</b> .....	<b>vii</b>
<b>Table of Contents</b> .....	<b>ix</b>
<b>List of Figures</b> .....	<b>xiii</b>
<b>List of Tables</b> .....	<b>xviii</b>
<b>1 Introduction</b> .....	<b>1</b>
1.1 Background.....	3
1.1.1 Shadow Detection .....	3
1.1.2 Shadow Restoration .....	5
1.2 Contributions.....	7
1.3 Dissertation Outline .....	9
<b>2 Light Detection and Ranging</b> .....	<b>11</b>
2.1 Time-of-Flight Lidar and Laser Scanning .....	11
2.2 Lidar Radiometry .....	13
2.2.1 Theory .....	14
2.2.2 Radiometric Correction.....	16
2.2.3 Radiometric Calibration.....	18
2.2.4 Hotspot Effect .....	20
<b>3 Hyperspectral Imaging</b> .....	<b>23</b>
3.1 Hyperspectral Sensors and Spectroscopy .....	24
3.1.1 Dispersive Sensors .....	24

3.1.2	Spectroscopy .....	25
3.2	Radiometric Calibration.....	27
3.2.1	At Sensor Radiance Sources .....	27
3.2.2	Calibration Methods.....	29
<b>4</b>	<b>Site, Sensors and Data .....</b>	<b>31</b>
4.1	Site .....	31
4.2	Sensors and Data.....	32
4.2.1	Lidar.....	32
4.2.1.1	Point Cloud Registration and Georeferencing .....	33
4.2.1.2	3D Triangulated Mesh .....	34
4.2.2	Hyperspectral Imagery.....	36
4.2.3	Analysis Area Selection.....	38
<b>5</b>	<b>Lidar and Hyperspectral Image Radiometric Calibration .....</b>	<b>40</b>
5.1	Lidar Radiometric Calibration .....	40
5.1.1	Leica HDS3000.....	40
5.1.2	Riegl VZ-400 .....	41
5.1.2.1	Technique.....	42
5.1.2.2	Evaluation .....	43
5.1.2.3	Adjustment.....	44
5.1.3	Calibration Uncertainty.....	46
5.2	Hyperspectral Image Radiometric Calibration .....	46
<b>6</b>	<b>Active and Passive Data Fusion .....</b>	<b>50</b>
6.1	Camera Model.....	51

6.1.1	Basic Model .....	52
6.1.1.1	Object Space to Camera Space .....	52
6.1.1.2	Camera Space to Image Space .....	53
6.1.1.3	Image Space to Pixel Space .....	54
6.1.2	Additional Parameters.....	55
6.1.2.1	Linear Array Tilt - $\gamma$ .....	55
6.1.2.2	Pixel Affinity - $S$ .....	56
6.1.2.3	Radial Lens Distortion - $k1$ and $k2$ .....	56
6.1.3	Model Summary.....	57
6.2	Model Calibration and Image Registration.....	57
6.2.1	Model Calibration .....	57
6.2.2	Image Fusion.....	59
6.3	Fusion Products.....	60
6.3.1	Co-Registered HSI.....	60
6.3.2	Rasterized and Segmented Active Reflectance.....	62
<b>7</b>	<b>Hyperspectral Image Shadow Detection and Restoration .....</b>	<b>65</b>
7.1	Shadow Detection .....	65
7.2	Shadow Restoration .....	69
7.2.1	Improvement Metrics.....	69
7.2.1.1	Spectral Shape and Spectral Scale .....	69
7.2.1.2	Band Correlation.....	72
7.2.1.3	Classification Consistency .....	72
7.2.2	Existing Restoration Methods.....	73

7.2.2.1	Pixel-Based Restoration.....	73
7.2.2.2	Region-Based Restoration .....	76
7.2.2.2.1	Methods.....	76
7.2.2.2.2	Similar Material Region Selection.....	78
7.2.2.2.3	Results.....	80
7.2.2.3	Summary Conclusions .....	86
7.2.3	Proposed Direct Scale Method.....	87
7.2.3.1	Single Wavelength.....	87
7.2.3.2	Multiple Wavelengths.....	92
7.2.3.3	Summary Conclusions .....	97
7.2.4	HSI Classification .....	97
7.2.4.1	Classifiers.....	98
7.2.4.2	Endmember and Training Pixel Extraction.....	99
7.2.4.3	Classification Results.....	100
<b>8</b>	<b>Conclusions and Recommendations.....</b>	<b>106</b>
8.1	Conclusions.....	106
8.2	Recommendations.....	108
	<b>References.....</b>	<b>112</b>

## List of Figures

3.1	Sources of radiance received by a camera .....	28
4.1	(a) Site location map. (b) Aerial view of the quarry with instrument locations .....	31
4.2	True color VNIR HSI band combination of the east quarry wall in full shade, partial sun, and maximum sun conditions (top to bottom). The scale bar is approximate due to image distortion.....	32
4.3	Small portion of the 3D mesh product. A hillshade has been applied to the mesh lines to improve visual interpretation .....	36
4.4	VNIR (background) and SWIR (foreground) HSI cameras attached to a tripod-mounted rotation stage. The cameras can be rotated vertically as well as horizontally .....	37
4.5	Maximum sun SWIR 1549 nm band image (top), and the same image masked to the analysis extents (bottom) .....	39
5.1	Leica HDS3000 radiometric calibration curves.....	41
5.2	Reflectance produced by the VZ-400 factory calibration compared to the quoted Spectralon panel reflectance .....	43
5.3	Factory radiometric calibration adjustment using an updated calibrated amplitude for the white reference. The 2013b dataset is shown. The shaded area indicates the range interval of interest .....	44
5.4	Spline interpolation of sparse calibrated amplitudes to reconstruct complete curve.....	45

5.5	(a) Original calibrated SWIR-shade 1549 nm band; (b) adjusted SWIR-shade 1549 nm band; (c) SWIR-sun 1549 nm band .....	48
6.1	(a) VNIR and SWIR (foreground) HSI cameras and rotation stage. (b) Illustration of the disk swept by the VNIR camera projection center (PC) as it revolves around the rotation center (RC). Linework is not to scale .....	51
6.2	(a) Object ( $X Y Z$ ), camera ( $\bar{X} \bar{Y} \bar{Z}$ ) and image ( $x' y'$ ) coordinate systems. (b) Pixel ( $u v$ ) coordinate system. Linework is not to scale .....	52
6.3	Transformation from camera space to horizontal image space ( $x'$ ). The computation of $d_{PC}$ is shown for subsequent use in the vertical transformation computations in Figure 6.4. Linework is not to scale .....	54
6.4	Transformation from camera space to vertical image space ( $y'$ ). Computations for $d_{PC,3D}$ and $h$ are required for the linear array tilt corrections given in Figure 6.5. Linework is not to scale .....	54
6.5	(a) Vertical and (b) horizontal components of linear array tilt additional parameter in image space.....	56
6.6	(a) VNIR calibration residuals. (b) SWIR calibration residuals .....	59
6.7	532 nm passive (a) and 532 nm active (b) reflectance images. 1549 nm passive (c) and 1550 nm active (d) reflectance images. Mean shift segmented 1550 nm active reflectance image is shown in (e) using spatial and spectral (8-bit image) bandwidths of 20 and 1, respectively.....	63
7.1	(a) SWIR-sun 1549 nm band. (b) Fractional (1/4 increment) shade determination. (c)-(e) Detail locations 1-3 as indicated in (a) and (b). (f)-(h)	

	Matching shadow computation for detail locations 1-3, where the gray value corresponds to the shadow fraction (white = full sun and black = full shade) .....	67
7.2	(a) SWIR-partial binary shade image. (b) Original shadow regions. (c) Split shadow regions. White indicates sunlit areas .....	68
7.3	(a) Original SWIR-partial 1549 nm band. (b) Shadows corrected via matching pixels selected using the 532 nm and 1550 nm active reflectance information. (c) Shadows corrected via matching pixels selected using active reflectance information and the spectral shape metric .....	75
7.4	Region selection methods: (a) union of active reflectance segments, (b) active reflectance segments, segment by segment, (c) cast shadow far edge buffer (arrows indicate solar ray direction) and (d) shadow boundary buffer.....	79
7.5	SWIR-partial HSI shadow restoration metrics. AR=Active Reflectance, AR-S=Active Reflectance-Segment by segment, EB=Edge Buffer, BB=Boundary Buffer .....	81
7.6	(a) Detail location. Shadow restoration: (b) mean scale, (c) mean scale, segment by segment, (d) linear correlation correction, (e) linear correlation correction, segment by segment, (f) mean scale with binary shade and (g) mean scale with fractional shade. ....	82
7.7	Mean correlation (a) and spectral shape median (b) with respect to pixel shadow fraction computation for the SWIR HSI.....	84

7.8	VNIR-partial HSI shadow restoration metrics. AR=Active Reflectance, AR-S=Active Reflectance-Segment by segment, EB=Edge Buffer, BB=Boundary Buffer .....	85
7.9	Sample comparison of (a) SWIR and (b) VNIR passive and direct scaled pixel spectra. The vertical lines indicate the TLS laser wavelengths .....	87
7.10	Spectral shape and spectral scale metrics illustrating the influence of indirect, direct and combined direct and indirect shadow restoration methods for the SWIR HSI .....	89
7.11	Spectral shape and spectral scale metrics illustrating the influence of indirect, direct and combined direct and indirect shadow restoration methods for the VNIR HSI .....	90
7.12	(a) Band correlation of passive, restored passive, scaled and restored scaled SWIR-partial HSI. (b) Same as (a), but for the VNIR-partial HSI. The vertical gray lines indicate the TLS laser wavelengths.....	91
7.13	SWIR (a) spectral shape and (b) spectral scale median (solid lines) and median notch (bounding areas) versus number of direct adjustment wavelengths, limited to those wavelengths available in commercial lidar systems. VNIR metrics shown in (c) and (d). .....	94
7.14	Comparison of direct scaled and direct shifted shade spectrum to matched sun spectrum using one, two and three wavelength locations. The left column is from the SWIR HSI; the right column is from the VNIR HSI .....	95

7.15 SWIR (a) spectral shape and (b) spectral scale median (solid lines) and median notch (bounding areas) metrics as a function of an increasing number of uniformly spaced direct adjustment wavelength locations. VNIR metrics are shown in (c) and (d).....	96
7.16 (a) VNIR and (b) SWIR endmembers. The spectra are not labeled since they do not refer to specific rock types.....	100
7.17 Classified VNIR maximum sun images corresponding to endmember spectra given in Figure 7.15: (a) SAM (same for passive and scaled), (b) passive MD, (c) scaled MD, (d) passive ML and (e) scaled ML.....	102
7.18 Classified SWIR maximum sun images corresponding to endmember spectra given in Figure 7.15: (a) SAM (same for passive and scaled), (b) passive MD, (c) scaled MD, (d) passive ML and (e) scaled ML.....	103

## List of Tables

4.1	TLS system specifications .....	33
4.2	VNIR and SWIR hyperspectral camera specifications .....	37
6.1	Camera model parameter summary .....	58
7.1	Common HSI and TLS laser wavelengths.....	93
7.2	Percentages of pixels with unchanged class assignments generated by the SAM, MD and ML classifiers. Restored image percentages are shown in parentheses.....	101

# Chapter 1

## Introduction

The standard method for remotely sensing topographic features with high spectral and spatial resolution is passive hyperspectral imaging (HSI). HSI data is characterized by hundreds of spectrally narrow (5-10 nm) and contiguous bands in the visible to shortwave infrared (400-2500 nm) portion of the electromagnetic spectrum (Schaepman et al., 2009). Since their development three decades ago (Goetz, 2009), HSI sensors have traditionally been deployed from aircraft in nadir viewing geometry, e.g., the Airborne Visible/Infrared Imaging Spectrometer (AVIRIS) developed by the Jet Propulsion Laboratory and similar commercial systems. Deployment of HSI cameras from terrestrial platforms for Earth remote sensing has only emerged in the past decade, and is often fused with dense lidar (light detection and ranging) point cloud data acquired with terrestrial laser scanning (TLS) instruments to create 3D models of dominantly vertical scenes containing rich structural and spectral information (Buckley et al., 2013; Kurz et al., 2013).

The majority of literature dealing with fused terrestrial laser scanning and HSI information is geologic in application. Examples include digital outcrop modeling for hydrocarbon reservoir analogue creation (Kurz et al., 2011, 2013; Buckley et al., 2013) and open pit mine face modeling for quantitative mineral content analysis (Kurz et al., 2012; Murphy et al., 2014). The inclusion of high resolution spectral information in these applications has the potential to enhance automatic identification of outcrop lithology through a variety of standard image processing and classification techniques (Kurz et al., 2011; Murphy et al., 2012) as well as expert systems that identify unique electronic and

vibrational spectral absorption features only detectable with HSI (Clark, 1999; van der Meer et al., 2012). For sufficiently curved outcrops, the exposed linear interfaces between spectrally identified lithologies can be used to create planar surfaces extending into the outcrop interior for 3D volumetric analyses (Buckley et al., 2010), such as geocellular reservoir modeling for simulating hydrocarbon fluid flow (Alexander, 1992).

Given the dominantly vertical and geometrically rugged nature of geologic outcrop formations, terrestrial HSI often contains a high proportion of shadowed pixels, even when collected during optimal sunlight conditions. Unless restored to direct sunlight conditions, shadows can reduce the amount of HSI information, e.g., shadowed areas are masked out (Kurz et al., 2013), or reduce the effectiveness of the HSI for material identification by deteriorating classification or target identification accuracy (Murphy et al., 2012; Ientilucci, 2013). Numerous studies have examined shadow restoration in airborne HSI, e.g., Adler-Golden et al. (2002), Friman et al. (2011) and Schläpfer et al. (2013), but the topic has yet to be addressed for HSI captured from a terrestrial modality. This is due in part to the relatively recent emergence of terrestrial HSI and also to the fact that the radiative transfer models (RTMs) employed in many restoration techniques are not designed to accommodate a horizontally viewing sensor.

This dissertation therefore examines shadow detection and restoration techniques in terrestrially acquired HSI of a vertical outcrop. The HSI is fused with TLS point cloud data for geometric shadow detection methods and also to leverage the relative invariance of the backscattered laser energy, i.e., lidar intensity, to solar illumination conditions in order to enhance existing shadow restoration methods and propose new techniques. Existing shadow

detection and restoration methods are reviewed in the subsequent sections, followed by a summary of the dissertation contributions and the structure of the remaining document.

## **1.1 Background**

### **1.1.1 Shadow Detection**

In order to restore HSI shadow spectra, the shadowed areas must first be identified in the imagery. Although the human eye can easily detect shadows in simple scenes, this is not a trivial task to digitally automate for geometrically complex structures such as rock outcrops. Shadow detection methods can be broadly divided into two groups: those based purely in image space and those employing supporting structural information of the scene acquired from photogrammetry or lidar measurements.

Image space methods appear to be more common as they do not require any external information. Methods include histogram thresholding (Dare, 2005), region growing (Xia et al., 2009), color invariance techniques that separate chromaticity from intensity (Tsai, 2006), matched filters using dark endmembers (Adler-Golden et al., 2002), unsupervised and supervised classification algorithms (Tolt et al., 2011; Adeline et al., 2013b) and empirical HSI band indices (Schläpfer et al., 2013). The wide variety of methods reflects the difficulty in consistently achieving high accuracy results. Low reflectance targets in sunlit regions, particularly water, and high reflectance targets in shadowed regions are problematic. Flat specular surfaces can also be mistakenly identified as shadows in sunlit regions when incident irradiance is reflected away from the camera direction (Adeline et al., 2013b). A recent review of image-based shadow detection by Adeline et al. (2013b) found that image space shadow detection methods produce typical accuracies in the range of 85-98% with

some dependence on the imaged scene, e.g., urban vs rural. Among the methods tested, a histogram threshold method using a linear mixture of visible and near infrared bands originally presented in Nagao et al. (1979) was found to perform best.

Ray tracing occlusion analysis, i.e., line-of-sight analysis, with respect to a 2.5D digital surface model (DSM) is a common structural shadow detection method found in current remote sensing literature (Adeline et al., 2013b). Other methods include the Z-buffer algorithm of Rau et al. (2002) and the combination of hillshade products and object segmentation (Zhan et al., 2005). Regardless of the method, the accuracy of structural shadow detection is directly correlated with the density and accuracy of the geometric model used for occlusion analysis and the quality of the registration between the structural and image information (Adeline et al., 2013b). Furthermore, in order to correctly locate the sun position relative to the scene geometry, high accuracy georeferencing information and exact image exposure times are required. It is often noted, e.g., Tolt et al. (2011) and Schläpfer et al. (2013), that these requirements are unavailable or insufficiently met for imagery collected from airborne platforms. Indeed, inferior results were produced in the comprehensive shadow detection review of Adeline et al. (2013b) due to insufficient DSM spatial density. However, structural methods are advantageous given their insensitivity to material reflectance and scattering characteristics, thereby eliminating errors due to dark sunlit regions, bright shadowed regions and specular surfaces (Adeline et al., 2013b). With careful data collection and processing and an appropriate HSI camera model, the requirements for accurate shadow detection using structural methods are hypothesized to be achievable with standard terrestrial data collection techniques. A structural method employing ray tracing occlusion analysis is therefore used in this dissertation. A key difference between existing

ray tracing methods found in the remote sensing literature and that employed in this dissertation is the use of a fully 3D model of the vertical outcrop structure rather than a 2.5D DSM.

### **1.1.2 Shadow Restoration**

Correct restoration of shadowed HSI pixel spectra is not a straightforward task since the spectrum of irradiance incident on shadowed surfaces is not simply a scaled version of that in direct sunlight (Adler-Golden et al., 2002; Ientilucci, 2013). The proportional influence of radiance scattered by the atmosphere and adjacent topographic features is greater in shadows than in sunlight (Lachérade et al., 2008). Therefore, the performance of the well-known spectral angle mapper (SAM) classifier, which is invariant to spectrum magnitude, is not as effective as would be expected for a simple attenuated spectrum (Murphy et al., 2012, Ientilucci 2013). Support vector machine (SVM) classifiers, which are increasingly common and have been shown effective for HSI analysis (Pal and Mather, 2004), also struggle to reliably identify materials in shadows when trained on materials in direct sunlight, or vice versa (Murphy et al., 2012).

Similar to shadow detection techniques, shadow restoration algorithms that do not employ RTMs can be divided between those based purely on image space statistics and those that incorporate knowledge of the environment's physical structure. Image space methods utilized in the remote sensing literature are dominated by companion area intensity mapping techniques that transfer pixel intensity histogram characteristics from illuminated areas to adjacent shadowed areas. Examples include histogram matching (Sarabandi et al., 2004), linear correlation correction (mean and variance transformation) (Sarabandi et al., 2004; Dare, 2005) and gamma control mapping (Li et al., 2005). Note that these methods operate

under the assumption that the companion areas contain a similar distribution of materials. Shadow restoration methods utilizing knowledge of the physical environment use a 2.5D DSM to compute the fraction of sky viewable from each pixel with respect to the complete overlying hemisphere. This fraction is incorporated into algorithms that parameterize the spectral ratio of solar irradiance to sky irradiance (resulting from atmospheric scattering) in order to restore shadowed pixel spectra (Friman et al., 2011; Zhang et al., 2013). These methods require selection of illuminated and shadowed pixels containing a common material in order to solve for the spectral irradiance ratio.

Physics-based scattering methods based on RTMs that trace solar irradiance from the top of the atmosphere to each image pixel do not require common materials in sun and shade pixels. However, these algorithms tend to be quite complex, iterative, and require spatial and spectral information of adjacent areas in order to model topographic scattering (Lach erde et al., 2008; Adeline et al., 2013a). They are also highly dependent on accurate absolute calibration of the HSI sensor data to physical units of radiance (Eismann, 2012), which is not available for the HSI sensors used in this dissertation. To date, no RTM solution for HSI acquired from a terrestrial sensor viewing a vertical structure from a horizontal perspective has been demonstrated.

A shared theme in many of the shadow restoration algorithms summarized above is the requirement to identify pixels, or regions of pixels, referring to common materials in sun and shade. Given the absence of any additional information, spatial proximity is often the only tool available; however, this can be a weak correlator in heterogeneous natural and urban environments, and many of the algorithms proposed in the literature resort to manual selection of sun and shade pixels representing common materials, e.g., Friman et al. (2011)

and Zhang et al. (2013). In contrast to passive HSI, lidar sensors use a laser as the source of electromagnetic radiation, i.e., they are active sensors, and the backscattered laser energy is resistant to the influence of solar position. Lidar intensity may therefore provide additional information for automated identification of materials common to both sun and shaded areas. In order to use lidar intensity for this purpose, the point cloud and HSI data must be precisely registered and the lidar spatial sampling must be sufficiently dense such that each HSI pixel contains one or more lidar points; these requirements are met for the TLS and HSI data collected for this dissertation.

Therefore, rather than ignoring lidar intensity information or examining it as a standalone characteristic as in Franceschi et al. (2009) or Burton et al. (2011), this dissertation proposes to utilize radiometrically calibrated lidar intensity contained in fused TLS and HSI datasets to improve restoration of shadowed areas in the passive HSI. Restoration techniques examined include direct scaling of shadow HSI pixel spectra with calibrated lidar intensity at their common wavelength in the reflectance domain and several indirect methods where lidar intensity is used to identify common materials existing in sunlit and shaded areas.

## **1.2 Contributions**

There are two primary contributions in this dissertation. The first is shadow detection and restoration performed in remote sensing HSI captured from a non-standard, i.e., terrestrial, modality. The second is the inclusion of active radiometric information, i.e., lidar intensity, in existing and new shadow restoration techniques. To date, shadow restoration has not been applied to terrestrial HSI, and the inclusion of lidar spectral information in image shadow restoration has not been considered in any modality. The overall objective of the work is to

restore the spectral shape and magnitude of shadowed pixels existing in terrestrial HSI to that of sunlit conditions.

A unique aspect of the structural shadow detection method used in this dissertation is the use of a fully 3D representation of the geologic outcrop surface. Standard remote sensing methods use 2.5D DSMs or mesh products that are not able to “fold” with respect to a fixed reference plane. However, the rugged, vertical and often curving nature of geologic outcrop formations requires a 3D model to adequately determine shadows at the high spatial resolution captured by close-range terrestrial HSI. The shadow detection method used in this dissertation also relies on a unique panoramic camera model adapted from the computer vision field to correctly represent the geometry of a dual camera stage that is capable of rotation about both the vertical and horizontal axes.

Current applications of fused lidar and HSI do not consider the spectral content of the lidar data. Instead, lidar points are colorized – or derived mesh products are draped – with several HSI bands or classification results. However, lidar intensity is not subject to solar illumination constraints and, for the rough surfaces typical of rock outcrops, is also resistant to the reduction in backscattered intensity predicted for inclined targets with Lambertian scattering characteristics (Franceschi et al., 2009; Hartzell et al., 2014). Both of these properties support consistent lidar intensity levels regardless of whether a surface exists in the sun or in the shade and are therefore exploited in this dissertation by augmenting several existing image shadow restoration methods and proposing a new method that directly combines the lidar intensity and HSI products.

### 1.3 Dissertation Outline

The basic principles of lidar and HSI are reviewed in Chapters 2 and 3, respectively, with a focus on radiometric calibration of the spectral content, i.e., conversion of the reported dimensionless digital numbers (DNs) to reflectance values. A greater amount of attention is given to the radiometric calibration of lidar intensity because lidar intensity is generally considered secondary to lidar spatial information and therefore radiometric calibration methods are less well known.

Chapter 4 describes the outcrop chosen for analysis, the TLS and HSI camera instruments and data collection methods, and registration and georeferencing of the TLS point clouds. The creation of the 3D mesh that is used for shadow detection and image co-registration is also detailed. The specific radiometric calibration methods applied to the active lidar intensity and passive HSI products follow in Chapter 5.

The fusion of the lidar spatial and spectral information with the HSI data requires a geometric model of the HSI cameras in order to project 3D points into 2D image space or, alternatively, to project rays from the 2D pixels into 3D object space. Chapter 6 begins with a derivation of an offset cylindrical camera model and calibration of the fixed interior orientation parameters. The results from registering, i.e., fusing, each HSI with the lidar spatial data is reviewed, followed by a description of the method used to co-register all HSI to a common pixel coordinate system. Last, the method used to generate a rasterized active lidar reflectance image in the common pixel coordinate system is reviewed and a technique for segmenting the active reflectance image described.

With the radiometric calibration and fusion of the active and passive datasets complete, shadow detection and restoration methods and results are discussed in Chapter 7. With

regard to shadow restoration, the use of active lidar reflectance to identify common materials in the sun and shade to augment existing shadow restoration algorithms is covered first, followed by a proposed method of directly combining the active reflectance data with the passive HSI spectra. In addition to metrics defining improvement in the restored shadow pixel spectra, the chapter concludes with several image classification results illustrating the influence of the shadow restoration algorithms. Finally, Chapter 8 summarizes the main results and conclusions and presents several recommendations for future research.

## Chapter 2

### Light Detection and Ranging

Range determination via measurements of electromagnetic energy in the optical spectrum, i.e., light detection and ranging, stems from nineteenth and early twentieth-century efforts to accurately measure the speed of light,  $c$ . Phase measurements of amplitude modulated continuous emission of light were used to determine travel time,  $t$ , to and from a reflecting target positioned at a known range,  $r$ . The speed of light was then computed as  $c = 2r/t$ . This basic relationship implied that if  $c$  were accurately known, target ranges could be readily computed from measured travel times. In 1948, a prototype range determination instrument, termed a geodimeter, and initial results with accuracies suitable for geodetic applications were presented by Dr. Erik Bergstrand (Bergstrand, 1949a, 1949b). Early geodimeters used a focused visible light source, such as a tungsten lamp and lens system, and a phototube for detection (Wolf and Ghilani, 2001). With the arrival of lasers in 1960 (Hecht, 2010), geodimeters were outfitted with this new light source for improved daylight operation and extended ranging capabilities (NOAA, 2012), thus forming the basic elements of modern lidar sensors. This chapter briefly reviews time-of-flight (TOF) lidar ranging and laser scanning, followed by a more in-depth discussion of lidar radiometry principles relevant to the radiometric calibration of lidar intensity.

#### 2.1 Time-of-Flight Lidar and Laser Scanning

Although many current TLS systems employ an amplitude modulated continuous wave laser for phase-based range measurements similar to the early geodimeters, their maximum

unambiguous range is limited by the longest wavelength modulated onto the carrier signal (Shan and Toth, 2008). For this reason, most modern long-range lidar sensors, including those employed in this dissertation, utilize pulsed lasers with a TOF ranging technique. Time-of-flight lidar relies on direct measurements of the emission and return times of a brief pulse of laser light directed at a reflecting target. A small portion of the emitted pulse is extracted with a beamsplitter and directed to a photodetector. A measure of the resultant signal, such as a threshold or constant fraction of peak amplitude, is used to mark the time of emission. Photons reflected by the illuminated target are collected by receiver optics having a field of view overlapping that of the emitted laser pulse and again focused on a photodetector to mark the return time. The target range is computed as  $r = ct/2$ , where  $t$  is the difference between emission and return times and the value of  $c$  has been adjusted for the refractive index of air.

The laser light source used for TOF lidar provides temporally short, powerful, narrow-band and highly collimated pulses of light with repetition rates on the order of 100's of kHz (Vosselman and Maas, 2010). The high power and narrow spectral bandwidth qualities provide long distance ranging capability and the short temporal duration and high collimation influence ranging accuracy, precision and the ability to resolve closely spaced targets. Although not employed in this dissertation, the energy backscattered from a target can be digitized at a very high frequency, typically around 1 GHz, and recorded in a technique termed "full waveform" lidar. Post-acquisition analysis of the recorded waveforms can produce additional return detections as well as improved range precision and target resolution in cluttered environments (Jutzi and Stilla, 2006; Parrish et al., 2011).

Laser scanning is a natural extension of lidar ranging. In its simplest form, emitted laser pulses are deflected in regular angular increments by a scanning mechanism, such as an oscillating or rotating mirror. With the addition of translational or rotational movement, a systematic pattern of lidar observations covering an areal, rather than linear, extent is created. At the time of each emitted laser pulse, the position and orientation of the scanning mechanism and the angle of the oscillating mirror are measured. These measurements are combined with the lidar range to generate 3D coordinates of the observed target. Terrestrial laser scanning systems are statically positioned, e.g., mounted on a tripod, and use the rotation of the scanning mechanism about a vertical axis to collect a uniform angular sampling of the targeted scene. Compared to airborne laser scanning systems, which are often mounted on rapidly moving fixed wing aircraft, TLS systems are able to produce much higher point densities, on the order of hundreds of points per square meter.

## **2.2 Lidar Radiometry**

In addition to range information, modern lidar sensors report a measure of backscattered laser energy, referred to as intensity, and reported in dimensionless DNs. Since the amount of backscattered energy is an indicator of target physical and chemical properties, correction and calibration of these DNs is an active research area. In this dissertation, radiometric correction refers to the normalization of intensity DNs so their relative magnitude is influenced only by target characteristics (Höfle and Pfeifer, 2007). Radiometric calibration will refer to methods that attempt to reliably transform reported DNs to a physical quantity descriptive of the target (Kashani et al., 2015), such as reflectance or cross-section.

### 2.2.1 Theory

Two physical theories are used to describe the scattering process: radiative transfer theory and electromagnetic theory (Wagner, 2010). Radiative transfer theory characterizes targets in terms of reflectance and centers around the bidirectional reflectance distribution function (BRDF), with biconical reflectance being the quantity measured by lidar sensors. Electromagnetic theory is built around the target cross-section property and considers the coherent nature of the emitted laser energy as well as fractional laser pulse returns, arguably making it the more appropriate theory for lidar radiometric measurements (Wagner, 2010). However, since methods for calibrating both passive and active radiometric measurements to reflectance are well established, particularly for passive measurements, reflectance is used in this dissertation as the bridge between the raw sensor radiometric measurements. The following derivation of the amount of optical power detected by a lidar sensor is based on the cross-section radiometric quantity but introduces several simplifications to re-parameterize the final expressions in terms of reflectance. A rigorous examination of how both radiative transfer and electromagnetic theory relate to lidar radiometry, as well as the benefits of using digitized full waveform lidar information, is given in Wagner (2010). Rather than repeat this extensive information, a more direct derivation following Wagner et al. (2006) is reviewed.

Assuming a circular laser beam cross-section, the footprint illuminated by the laser on an orthogonal target is

$$A_f = \frac{\pi R^2 \beta^2}{4}, \quad (2.1)$$

where  $R$  is the target range and  $\beta$  is the laser beam divergence expressed in radians. Note that  $R\beta$  is the diameter of the laser footprint. The average power density within the footprint is then

$$S_f = \frac{P_t}{A_f} = \frac{4P_t}{\pi R^2 \beta^2}, \quad (2.2)$$

where  $P_t$  is the transmitted laser power. Assuming an opaque target, the total power scattered is a function of target reflectivity and area,

$$P_s = S_f \rho A_s = \frac{4P_t}{\pi R^2 \beta^2} \rho A_s, \quad (2.3)$$

where  $\rho$  is the target reflectivity and  $A_s$  is the scattering area of the target. If we assume the scattered power is distributed uniformly into a cone of solid angle  $\Omega$ , and that  $\Omega$  intercepts the lidar receiver, the power density at the receiver is

$$S_r = \frac{P_s}{\Omega R^2} = \frac{4P_t}{\pi R^2 \beta^2} \rho A_s \frac{1}{\Omega R^2}. \quad (2.4)$$

The receiver aperture area controls the power entering the receiver which leads to

$$P_r = S_r \frac{\pi D_r^2}{4} = \frac{4P_t}{\pi R^2 \beta^2} \rho A_s \frac{1}{\Omega R^2} \frac{\pi D_r^2}{4}, \quad (2.5)$$

where  $D_r$  is the diameter of a circular aperture. The standard form of the radar equation used for lidar, e.g., Jelalian (1992), Wagner et al. (2006) and Wagner (2010), is obtained by separating out those terms relating to the target characteristics of size, reflectivity and scattering directionality, i.e., the target cross-section, and is given as

$$P_r = \frac{P_t D_r^2}{4\pi R^4 \beta^2} \sigma, \quad (2.6)$$

where  $\sigma$  is the target cross-section and is given as

$$\sigma = \frac{4\pi}{\Omega} \rho A_s. \quad (2.7)$$

If we assume an extended Lambertian target, then the following statements are true:

1.  $A_s = A_f$ ,
2.  $\sigma$  is decreased by a factor of  $\cos(\theta)$ , where  $\theta$  is the incidence angle (Lambert's cosine law), and
3. the scattering solid angle  $\Omega$  is equal to  $\pi$  (Jelalian, 1992; Wolfe, 1998).

Equation (2.7) then becomes

$$\sigma = \pi R^2 \beta^2 \rho \cos(\theta). \quad (2.8)$$

Substituting Equation (2.8) into Equation (2.6) produces

$$P_r = \frac{P_t D_r^2 \rho \cos(\theta)}{4R^2}. \quad (2.9)$$

The final form of the laser radar equation under the assumption of extended Lambertian targets and parameterized in terms of reflectance is produced by introducing coefficients for atmospheric attenuation and system efficiency,  $\eta_{atm}$  and  $\eta_{sys}$ , which results in

$$P_r = \frac{P_t D_r^2 \rho \cos(\theta)}{4R^2} \eta_{atm} \eta_{sys}. \quad (2.10)$$

Note that lidar systems do not deliver  $P_r$  in physical units, but rather as dimensionless DN's that are typically related to the maximum amplitude of the detected signal power (Joerg et al., 2015) and generically referred to as intensity. This raw intensity will be referred to as  $I_{raw}$ .

### 2.2.2 Radiometric Correction

Whereas  $P_r$ , or, equivalently,  $I_{raw}$ , represents a measure of the backscattered optical power, it is not an appropriate indicator of target reflectance due to the non-static nature of

the following parameters:  $R$ ,  $\theta$ ,  $\eta_{atm}$ , and  $P_t$ . Raw lidar intensities must therefore be normalized, or corrected, for each of these variable parameters in order to be comparable (Höfle and Pfeifer, 2007; Kaasalainen et al., 2011b; Joerg et al., 2015). The parameter normalizations are as follows:

1. Range ( $R$ ): Lidar intensities are inversely proportional to the square of range. Raw intensities are normalized by applying the factor  $R^2/R_{ref}^2$ , where  $R_{ref}^2$  is an arbitrary reference range.
2. Incidence Angle ( $\theta$ ): For a Lambertian surface, backscattered optical power decreases with the cosine of the incidence angle. Given an estimated surface normal direction at each observed lidar point, an inverse cosine factor  $1/\cos(\theta)$  is applied to the raw intensity value. Note that alternate correction factors can be applied for non-Lambertian surfaces (Joerg et al., 2015).
3. Atmospheric Attenuation ( $\eta_{atm}$ ): Scattering and absorption by atmospheric molecules attenuate received lidar optical power in a nonlinear manner inversely proportional to range. Given an atmospheric attenuation coefficient  $a$  in decibels (dB) per kilometer, lidar intensities can be corrected using the factor  $10^{2 \cdot R \cdot a / 10000}$  (Höfle and Pfeifer, 2007). Note that  $R$  must be in meters for this expression.
4. Transmitted Power ( $P_t$ ): A measure of transmitted power for each laser pulse is generally not available for commercial lidar sensors. Therefore, it is typically assumed stable, although Kaasalainen et al. (2011b) and Roncat et al. (2012) have shown that pulse power can vary stochastically from shot to shot as well exhibit bias and drift between and within ALS campaigns. Laser pulse power is often dependent on pulse repetition frequency (PRF), with higher PRF rates producing lower power

laser pulses. If nominal power information with respect to different PRFs is available, raw intensities at a particular power level  $P_{PRF}$  can be normalized to an arbitrary PRF power level  $P_{ref}$  using the factor  $P_{ref}/P_{PRF}$  (Kaasalainen et al., 2011b; Joerg et al., 2015).

A single expression for corrected lidar intensity  $I_{corr}$  is produced by combining the corrections summarized above and is given as

$$I_{corr} = I_{raw} \cdot \frac{R^2}{R_{ref}^2} \cdot \frac{1}{\cos(\theta)} \cdot 10^{2 \cdot R \cdot \frac{a}{10000}} \cdot \frac{P_{ref}}{P_{PRF}}. \quad (2.11)$$

### 2.2.3 Radiometric Calibration

Once corrected, lidar intensities can be interpreted with respect to their relative magnitude; returns with relatively large corrected intensities indicate targets with higher reflectance or larger cross-section properties than those with lower corrected intensities. However, a direct correlation to a target's radiometric properties in physical units requires lidar intensities to be radiometrically calibrated. To accomplish this, the static terms in Equation (2.10) can be grouped into a single calibration constant,  $C_{cal}$ , and  $P_r$  recast as

$$P_r = C_{cal} \frac{P_t \rho \cos(\theta)}{R^2} \eta_{atm}, \quad (2.12)$$

where  $C_{cal} = D_R^2 \eta_{sys}/4$ . For the work in this dissertation, two TLS systems are employed at constant power levels and short ranges. Therefore, both  $P_t$  and  $\eta_{atm}$  can be considered constant and included in  $C_{cal}$  leading to a further simplification,

$$P_r = C_{cal} \frac{\rho \cos(\theta)}{R^2}. \quad (2.13)$$

Solving for  $\rho$  we obtain

$$\rho = \frac{P_r R^2}{C_{cal} \cos(\theta)}. \quad (2.14)$$

Note that  $P_r = I_{raw}$  for our purposes.

Equation (2.14) is deceptively simple for two reasons. First, it assumes the raw intensities are linearly related to the received optical power. This is not the case for many TLS systems due to optical defocusing at close ranges (Biavati et al., 2011; Fang et al., 2015) and pulse power compression characteristics (Ullrich and Pfennigbauer, 2011; Pfennigbauer et al., 2013) that exist in some lidar sensors to accommodate the very high dynamic range of received optical power. Note that both of these issues can be considered unique to TLS as opposed to ALS where short ranges are not observed and sensor linearity is prevalent, which has traditionally been at the forefront of lidar radiometric calibration techniques. The second simplification in Equation (2.14) is the assumption of extended Lambertian targets. For geologic outcrop modeling, the assumption of extended targets is acceptable; however, Franceschi et al. (2009) and Hartzell et al. (2014) have demonstrated that rock outcrop surfaces do not exhibit Lambertian scattering characteristics.

Radiometric calibration can also be accomplished by purely empirical methods, where a target of nearly 100% reflectance is observed at a series of ranges and the resulting raw intensities stored in a look up table (LUT) (Kaasalainen et al., 2009; Kaasalainen et al., 2011a). Subsequent raw intensity observations are converted to a relative reflectance value by dividing the observed intensity value by the LUT intensity that was observed at the same range. This is useful for systems which report raw intensities linearly proportional to received optical power but do not follow the radar equation at close ranges due to optical defocusing. It is noted here that Fang et al. (2015) recently introduced a rigorous physical model for optical defocusing, but calibration of the model parameters requires observations

of reflectance standards at multiple ranges, resulting in an effort not dissimilar to that required for a purely empirical calibration.

Lidar sensors with nonlinear sensor response characteristics can be empirically calibrated by observing multiple targets with reflectance values ranging from very low to very high at a series of ranges encompassing the LiDAR system's operational envelope (Hartzell et al., 2014, 2015). The resulting range, peak amplitude, and target reflectance values are stored in a three dimensional LUT (raw intensity, range, reflectance). Calibrated reflectance values are then interpolated from the LUT for subsequent intensity and range measurements. This method is generic for any sensor and is similar to that employed by Riegler V-line TLS systems, which are able to directly report calibrated reflectance quantities for each lidar return under the assumption of extended Lambertian targets at normal incidence (Pfennigbauer and Ullrich, 2010).

#### **2.2.4 Hotspot Effect**

The influence of the hotspot effect, or opposition surge, is important to understand when comparing passive imagery and active lidar intensity products. The hotspot effect is a sharp increase in observed backscattered energy when the geometric alignment of an energy source and optical detector is coincident, or nearly so (Kaasalainen et al., 2005; Papetti et al., 2007). This is the natural geometry for lidar sensors, but not for passive optical imagery, which leads to disparities between their radiometric products for common targets. The surge in backscattered optical radiation is quantified as the ratio between the intensities observed in the direct backscatter direction and an off-axis direction just outside the hotspot region, which is typically no more than a few degrees. Hotspot ratios range between 0 and 2 and

have been shown to be dependent on laser wavelength and polarization (Papetti et al., 2007) and aperture diameter (Kaasalainen and Kaasalainen, 2008).

Two theories exist to explain the hotspot effect. The first is a function of surface roughness and is called shadow hiding. Because shadows caused by surface roughness are only observable from an off-source viewing geometry, the surface appears brighter when viewed in line with the energy source. The second theory is coherent backscattering. When considering the dual wave-particle nature of optical radiation, photons reflected from a surface self-interfere constructively when directly backscattered to the emission source location (Corey, 1995). This is analogous to the concept in Young's double slit experiment where photons are detected at discrete locations on a screen located behind two slits, but the photon location pattern is predicted by wave interference. In this case, the observed magnification is explained by constructive interference of the wave nature of photons as they traverse the same path in opposite directions. The constructive interference is only observed when the viewing direction is approximately the same as the incident photon direction, with a theoretical power factor of 2.0 at exact backscatter geometry (Papetti et al., 2007).

The hotspot effect complicates efforts to radiometrically calibrate lidar intensities to reflectance values directly comparable to their passive counterparts. Use of direct backscatter measurements rather than passive measurements (such as those obtained with portable spectroradiometers) for lidar radiometric calibration techniques based on the physical models developed in Equations (2.6) and (2.10) has been proposed in Briese et al. (2008) and Lehner and Briese (2010) as a more appropriate measure for natural calibration targets. Direct backscatter measurements are also naturally used in empirical calibration methods. However, given the variable and generally unknown nature of the hotspot effect for different materials,

including calibration materials, current lidar radiometric calibration methods produce reflectance values that can differ from their passive counterparts by up to 10% for some rock types (Hartzell et al., 2014).

## **Chapter 3**

### **Hyperspectral Imaging**

The origins of hyperspectral imaging sensors applied to Earth remote sensing tasks is traced to the development of the experimental Airborne Imaging Spectrometer at the Jet Propulsion Laboratory in the early 1980s, followed by the development of the AVIRIS instrument (Goetz et al., 1985; Schaepman et al., 2009). Numerous commercial manufacturers exist today, such as ITRES, HySpex and SPECIM, with most Earth remote sensing applications deploying the sensors from airborne platforms. Acquisition of vertical features with terrestrially mounted HSI sensors, which is examined in this dissertation, is a relatively recent development that provides spectral information on a spatial scale between that of airborne and laboratory based sensors.

This chapter briefly reviews the basic design of hyperspectral sensors, spectroscopy and HSI radiometric calibration methods. The content is not intended to serve as a source of in-depth information, but rather to summarize the basic concepts underpinning hyperspectral remote sensing in order to provide context for the fusion of active and passive spectral products. Much of the information is sourced from Eismann's (2012) text on hyperspectral remote sensing, which provides a thorough review of hyperspectral imaging concepts including spectroscopy, sensor design, sensor and image calibration, and image feature extraction and classification.

### **3.1 Hyperspectral Sensors and Spectroscopy**

The term hyperspectral imaging is often used interchangeably with imaging spectroscopy or imaging spectrometry (Schaepman et al., 2009) and refers to the simultaneous collection of spatially registered images, with the set of images collected from narrow, contiguous wavelength bands. This is in contrast to traditional photography, which records electromagnetic energy in three broad bands (red, green and blue) in the visible portion of the spectrum, and multispectral imagery, which is characterized by relatively broad and non-contiguous bands located within the visible and infrared regions. Each spatial pixel of the composite set of images, termed a cube since it is a 3D structure, forms a spectrum of observed optical energy across the sensor wavelength range at a particular scene location. The data in an HSI spatial pixel is therefore similar to that obtained with traditional point spectrometer instruments.

#### **3.1.1 Dispersive Sensors**

In order to record the spectrum of electromagnetic energy radiating from a discrete spatial location, i.e., the field of view of a single HSI camera pixel, the incoming radiation is dispersed such that it is focused at differing physical locations according to wavelength. For a camera with a field of view limited to a linear array of spatial pixels (by way of a slit), the dispersed energy can be focused onto a 2D focal plane array having both a spatial and spectral dimension. In order to form a cube with two spatial dimensions and one spectral dimension, which is the natural form of HSI data, it is necessary to record multiple exposures of the spectrally dispersed line of spatial pixels while changing the camera field of view in a

regular fashion. For example, the HSI data cubes used in this dissertation were constructed using camera rotation to change the field of view.

The light entering an imaging spectrometer is spectrally dispersed by way of refraction or a combination of diffraction and interference (Eismann, 2012). Prisms use refraction to disperse light, where the change in refractive index between the prism and its surroundings causes the passing light to bend at differing rates depending on wavelength (Snell's Law). In practice, most sensors disperse light by way of a diffraction grating, which is a periodic structure of surface transmission or reflection with the features spaced on the order of the optical wavelengths. Each periodic structure acts as a point light source through diffraction. This results in phase interference that is dependent on the distance from each grating element, thus spectrally dispersing the incoming light to different spatial locations. Although not discussed further here, dispersive spectrometer performance is characterized by resolving power (a measure of the minimum wavelength difference able to be detected), spectral range, optical throughput, spatial and spectral distortion on the focal plane array and radiometric sensitivity (Eismann, 2012).

### **3.1.2 Spectroscopy**

Dispersive sensors enable the wavelength dependent interaction of electromagnetic energy with matter to be studied, i.e., the science of spectroscopy. Each HSI pixel spectrum enables the estimation of material type, or mixture of materials, by analysis of the spectrum features. Given the complex atomic and molecular composition and surface roughness characteristics typical of most materials, practical remote sensing is largely based around empirical observations of apparent material properties, such as spectral reflectance and transmission, rather than measurement of intrinsic spectral properties derived from physical

models, such as the complex index of refraction (Eismann, 2012). In general, materials absorb or reflect electromagnetic energy as a function of molecular vibration and rotation or atomic and molecular electronic transitions. Each of these physical characteristics is wavelength dependent and thus contributes to a material's apparent spectral reflectance signature. For minerals, observed spectral characteristics in the visible to near infrared wavelengths are influenced primarily by electronic transitions and charge transfer processes whereas molecular vibrational features are more influential in the short wave infrared region (Eismann, 2012).

The content of an HSI data cube is therefore a collection of spectroscopic measurements of apparent surface reflectance that enable estimation of material content in each pixel. The pixel spectra can be directly used in geometric classifiers such as the SAM or minimum distance (MD) methods, where the only requirement is selection of "endmember" spectra that represent spectrally unique materials. Alternatively, features can be extracted from the HSI cube by transforming the data into a space that maximizes the information content while reducing data dimensionality, e.g., principal component analysis (PCA). Features from pixels representative of each desired class are then used to train a statistical classifier such as the maximum likelihood (ML) method. Conversely, HSI data can be projected into higher dimensions for the purpose of determining a space where the desired classes are linearly separable, which is the method of support vector machine (SVM) classifiers. A review of the SAM, MD, ML and SVM classifiers as well as PCA and other transformations can be found in Eismann (2012).

## 3.2 Radiometric Calibration

As with lidar sensors, radiometric calibration refers to the conversion of the dimensionless DNs reported by HSI sensors to physical units such as radiance or reflectance. Conversion of DNs to radiance is typically performed by the manufacturer or a specialized facility having a calibrated light source with traceable spectral irradiance characteristics and an integrating sphere to provide a uniform irradiance source for the camera. Conversion of DNs to reflectance, however, can be accomplished with in situ reflectance standards. The different sources of radiance observed by an HSI sensor are reviewed first, followed by a description of two common radiometric calibration methods which accommodate the radiance sources while estimating surface reflection.

### 3.2.1 At Sensor Radiance Sources

Figure 3.1 illustrates the primary sources of radiance received by a sensor according to Eismann (2012), which are as follows:

1. direct solar irradiance reflected off the surface and transmitted to the sensor,
2. indirect solar irradiance scattered by the atmosphere, reflected by the surface and transmitted to the sensor,
3. irradiance reflected by surrounding objects, reflected by the surface and transmitted to the sensor,
4. irradiance reflected by the ground or surrounding objects, scattered by the atmosphere, reflected by the surface and transmitted to the sensor (this source is known as the adjacency effect), and
5. path radiance scattered by the atmosphere and transmitted directly to the sensor.

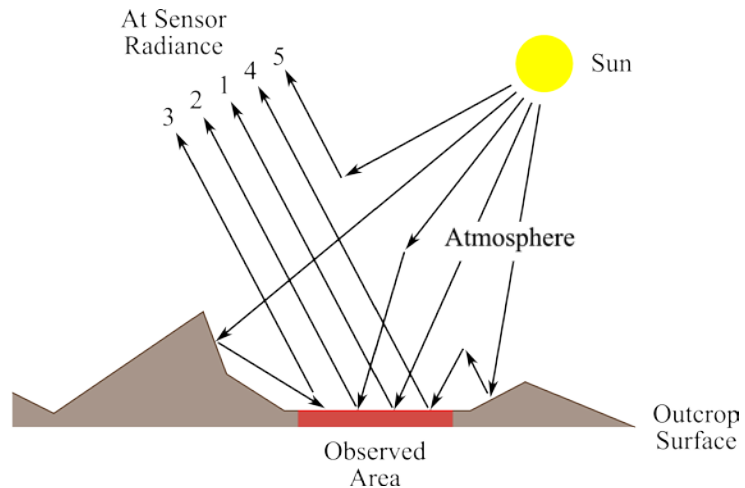


Figure 3.1: Sources of radiance received by a camera.

This list is not exhaustive, as Lachérade et al. (2008) notes a few more sources; however, the additional sources originate from combinations of reflected and atmospherically scattered radiance, making their impact relatively small. According to Lachérade et al. (2008), the main radiance sources when viewing dominantly sunlit areas are the direct and atmospherically scattered irradiance sources that do not depend on neighboring objects or surfaces (sources 1, 2 and 5). For shadowed areas, irradiance originating from reflection by the surrounding environment is important.

Not all signal output from a sensor's photodetector is due to the radiance collected by the sensor optics; self-emission of electromagnetic energy from the internal camera components and dark current resulting from thermally excited electrons in the detector material are both signal sources independent of the observed radiance (Eismann, 2012). Both of these signals are a function of temperature and are the reason why HSI cameras are often cooled. For example, the short wave infrared camera used in this dissertation is cooled to less than 200 K (-73°C) to mitigate dark current (Spectral Imaging Ltd., 2014).

### 3.2.2 Calibration Methods

The empirical line (EL) calibration method, which is based on in situ observations of targets with known spectra, and model-based methods, which describe the radiative transfer of sunlight as it interacts with the atmosphere and reflecting surfaces (Clark et al., 2002), are described below. Scene-based methods, such as flat field correction (Carrere and Abrams, 1988) and internal average reflectance (Kruse, 1988), are not reviewed given their limitations in obtaining high fidelity reflectance spectra (Clark et al., 2002).

The EL method relies on naturally occurring or synthetic in situ calibration targets with known reflectance spectra. A linear instrument response is assumed and a simple gain and offset transformation used to obtain reflectance from the sensor DNs. The EL transformation is given as

$$\rho = DN \times g + o, \quad (3.1)$$

where  $\rho$  is reflectance,  $g$  is the gain factor and  $o$  is the offset. The gain and offset parameters are solved using pixel DNs of at least two different in situ targets of known reflectance, with a least squares regression used if three or more reference targets are available. Unique parameters are solved and applied to each HSI wavelength band. Note that the gain variable accommodates not only the sensor-specific range of DNs, but also all sources of irradiance incident on the reflecting calibration targets (sources 1-4 in Figure 3.1); the offset variable accommodates path radiance (source 5). Since the in situ targets occupy only a small portion of the image, the EL method assumes the scene irradiance sources are space invariant, e.g., no shadows, smooth terrain and uniform path radiance and scattering from adjacent topography (Eismann, 2012).

Model-based methods for calibrating HSI to reflectance utilize radiative transfer principles to estimate atmospheric transmission, absorption and scattering characteristics. With knowledge of local topography, solar angle at the time of HSI acquisition and top of atmosphere solar irradiance, it is possible to estimate surface reflectance from the radiance observed by the camera. Note that this method requires the HSI sensor to be absolutely calibrated in units of radiance. Model-based methods can, in principle, better estimate surface reflectance because they constrain the estimation to realistic atmospheric and illumination characteristics (Eismann, 2012), i.e., they do not rely on space invariant illumination assumptions. However, they are more complex, require user familiarity with RTMs and are susceptible to errors in sensor absolute calibration; if the at-sensor radiance values are not accurate, the model will predict incorrect surface reflectance even if the atmospheric parameters are perfectly known. As an example of complexity, one of the most commonly used RTMs (MODTRAN) exceeds 80,000 lines of code (Brazile et al., 2008). Although model-based calibration methods can be used to restore shadowed imagery when augmented with topographic information, their complexity motivates our exploration of alternative methods for shadow restoration, with a focus on augmenting existing non-RTM methods with calibrated lidar intensity and investigating direct combinations of lidar and HSI reflectance data.

## Chapter 4

### Site, Sensors and Data

#### 4.1 Site

An interdisciplinary research team from the University of Houston's Civil Engineering and Geoscience departments visited an abandoned quarry located 6 km northeast of Huntsville, Arkansas on May 4, 2015 to collect high resolution spatial and spectral observations of the vertical quarry walls. The quarry is rectangular in shape with the four walls roughly oriented along the cardinal directions (Figure 4.1). TLS and HSI observations were collected in mostly sunny conditions, with the HSI collection restricted to periods of full sunlight. The east wall is the focus of the analysis since HSI was captured with the wall in full shade, partial shade, and maximum sun conditions (Figure 4.2). The full shade and

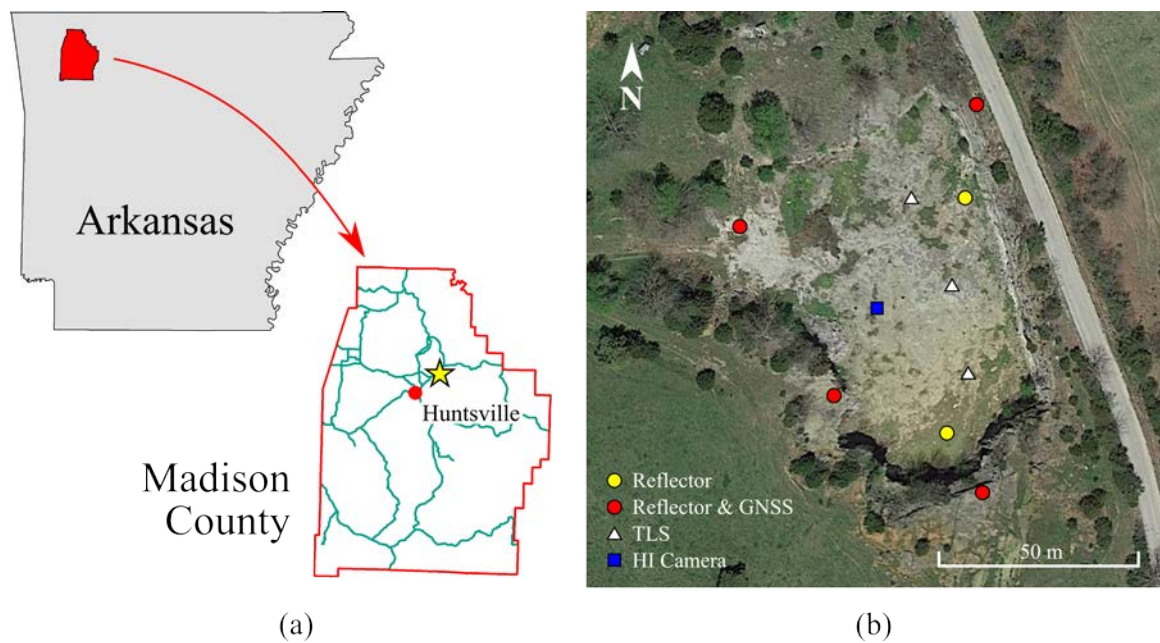


Figure 4.1: (a) Site location map. (b) Aerial view of the quarry with instrument locations.

maximum sun HSI are used to quantify the effectiveness of the shadow restoration techniques applied to the partial shade HSI in Chapter 7.

## 4.2 Sensors and Data

### 4.2.1 Lidar

The east quarry wall was measured with a 1550 nm laser wavelength Riegl VZ-400 TLS

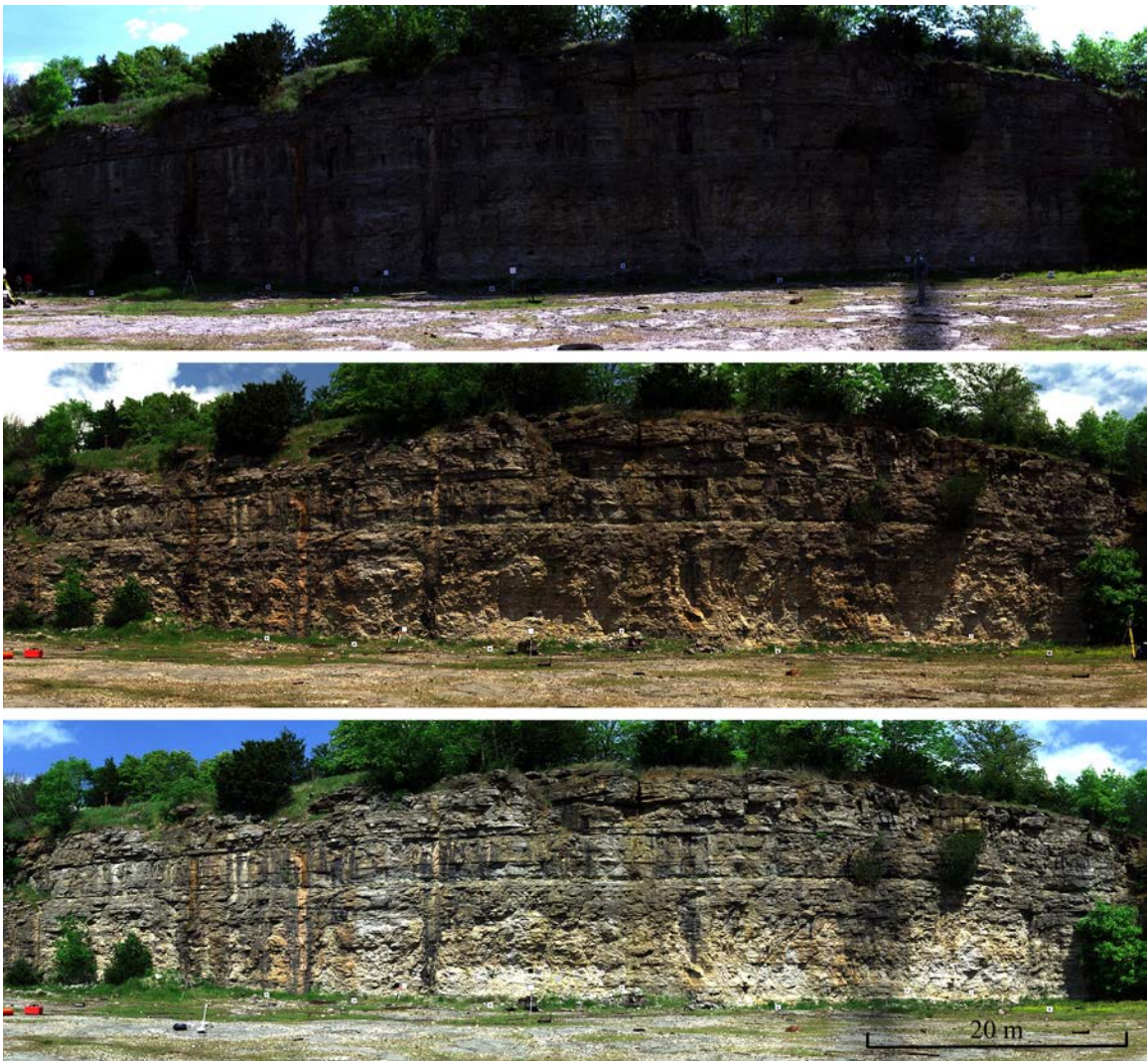


Figure 4.2: True color VNIR HSI band combination of the east quarry wall in full shade, partial sun, and maximum sun conditions (top to bottom). The scale bar is approximate due to image distortion.

and a 532 nm laser wavelength Leica HDS3000 TLS from three scan positions offset approximately 16 m from the outcrop face. TLS system specifications are given in Table 4.1. Point spacing was less than 5 mm with the VZ-400, and less than 20 mm with the HDS3000. The relatively coarse resolution of the HDS3000 is due to its much lower pulse repetition rate.

#### 4.2.1.1 Point Cloud Registration and Georeferencing

The VZ-400 scans were initially co-registered using common observations to 6 retroreflective cylindrical targets. This was followed by a fine registration technique which minimizes the distance between matching planar features found in the separate point clouds via least squares. Approximately 40,000 planar features were automatically extracted and used in the adjustment. The differences between adjusted matching planar features produced a standard deviation of 2.4 mm. Riegl’s RiSCAN PRO processing software (Riegl LMS GmbH 2015) was used for all scan registration tasks. The HDS3000 scans were also imported into RiSCAN PRO and registered in the same manner with similar results.

The registered point clouds were georeferenced to the WGS84(G1762) datum using post-processed static GNSS observations from antennas collocated with four of the retroreflective cylinder targets surrounding the project area (See Figure 4.1). The GNSS data was collected

Table 4.1: TLS system specifications.

<b>Property</b>	<b>Leica HDS3000</b>	<b>Riegl VZ-400</b>
Laser wavelength	532 nm	1550 nm
Beam divergence or spot size	<6 mm at 50 m	0.35 mrad
Maximum range	300 m	400 m
Pulse repetition frequency	4 kHz	300 kHz
Range accuracy	4 mm	5 mm at 100 m

with Trimble NetR9 receivers and Zephyr Geodetic antennas and processed against the Continuously Operating Reference Station (CORS) CTA1 using Novatel's Waypoint GrafNet software. The  $1\sigma$  estimated errors in the final adjusted coordinates were 7 mm or less in all components (North, East and Up). In a final step, the georeferenced point clouds were transformed to a local geodetic system having an origin at the approximate center of the quarry floor to support shadow computation methods that utilize local solar zenith and azimuth angles.

#### 4.2.1.2 3D Triangulated Mesh

A triangulated mesh is used as the basis of occlusion analysis for shadow determination and HSI camera visibility of individual TLS points. However, creation of mesh products in 3D space from TLS point cloud data is not straightforward, particularly for merged point clouds generated from multiple scan positions (Buckley et al., 2008). Conventional triangulation algorithms applied to airborne lidar datasets, such as 2D Delaunay triangulation, assume that only a single  $z$  value can exist for any  $x$ - $y$  coordinate pair, i.e., a surface is not allowed to fold over on itself with respect to the  $x$ - $y$  plane. This is clearly not the case for vertical outcrops with overhanging ledges and, given the roughness and curvature typical of outcrops, is invariably violated regardless of the orientation of the 2D plane against which the triangulation is performed.

An additional complexity exists when meshing TLS point clouds with point spacing finer than typical range noise or scan registration accuracy. Triangulation of such a point cloud produces a mesh surface that represents the error sources rather than surface shape at very fine scales, which can cause incorrect shadow and camera visibility determinations. For the VZ-400 measurements of the east quarry wall, range noise was estimated from several best

fit planes to flat targets to be  $\pm 4$  mm and, as stated previously, scan registration error was  $\pm 2$  mm, both at  $1\sigma$ . The average point spacing for the combined scans is  $\sim 2$  mm, indicating the outcrop is sampled beyond individual point positioning accuracy. An obvious solution is to decimate the scan to mitigate the problem. However, although the point clouds were decimated to 4 mm spacing to produce a consistent surface point density, further decimation is undesirable since the fine lidar point spacing provides redundant active intensity information that is valuable for estimating surface active reflectance.

To address these challenges, a mesh surface reconstruction algorithm developed by Kazhdan and Hoppe (2013) and implemented in the open source CloudCompare point cloud software (CloudCompare, 2015) was used. The algorithm is capable of creating a 3D mesh that follows complex, undulating surfaces from a point cloud by using surface normal directions estimated at each point. Rather than directly interpolating the points, the algorithm generates new mesh vertices that form a smoothed representation of the original point cloud. The amount of smoothing is controlled by a weighting factor that balances the influence of the estimated point normals and the point locations. A weighting factor of 4 was used per the findings in Kazhdan and Hoppe (2013). An example is given in Figure 4.3. After creation of the mesh, the mesh and original point cloud were simultaneously visualized and the distance between the points and mesh qualitatively assessed and found to be within 5 mm for most points, which was deemed acceptable in light of the range noise and registration errors. The lidar points were then projected to the closest location on the smooth mesh, thereby reducing the impact of noise and registration errors on subsequent shadow computations. Note that this algorithm works well on bare outcrop surfaces, but is only a coarse representation of

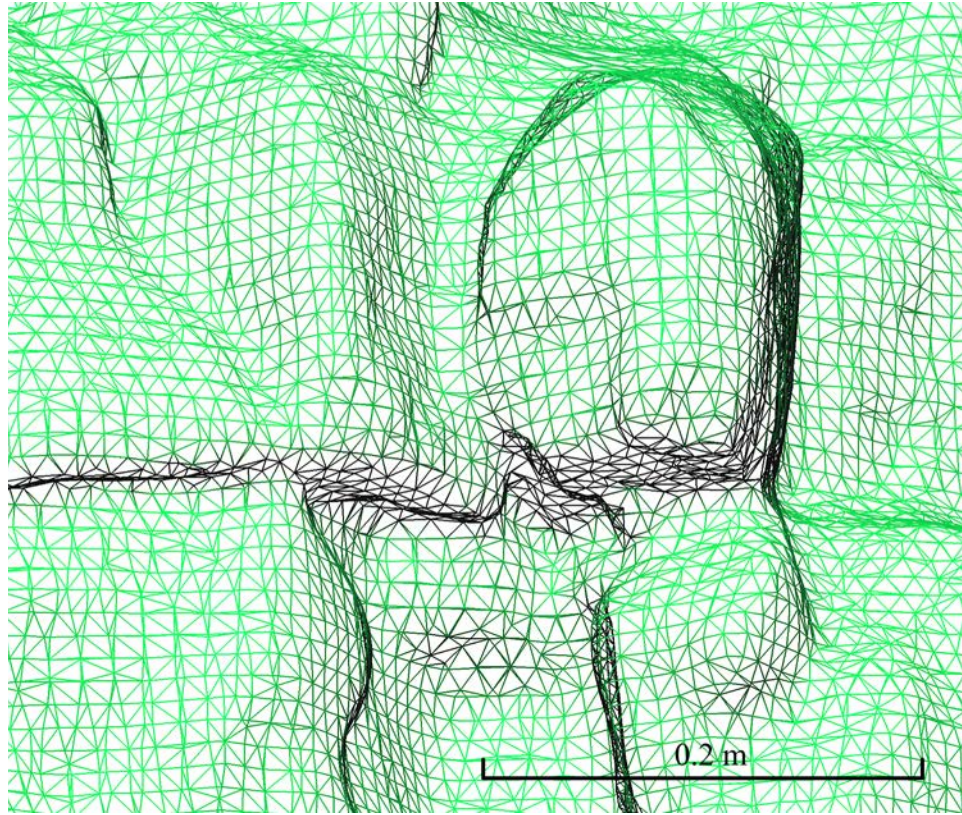


Figure 4.3: Small portion of the 3D mesh product. A hillshade has been applied to the mesh lines to improve visual interpretation.

vegetation, which is characterized by complex volumes of points not well represented by a mesh.

#### 4.2.2 Hyperspectral Imagery

The outcrop was imaged with the following two hyperspectral linear array cameras manufactured by Spectral Imaging, Ltd.: a visible to near infrared (VNIR) camera operating in the 400-1000 nm wavelength range and a short wave infrared (SWIR) camera operating in the 970-2500 nm wavelength range. Relevant camera specifications are given in Table 4.2. Both cameras were mounted simultaneously on a rotating stage (Figure 4.4) with the linear array oriented vertically and the stage rotation and camera exposure rates selected such that

Table 4.2: VNIR and SWIR hyperspectral camera specifications.

Property	VNIR	SWIR
Wavelength range	400-1000 nm	970-2500 nm
Spectral resolution	2.8 nm	10 nm
Spectral pixel count	840	240
Spectral sampling	0.72 nm/pixel	6.3 nm/pixel
Pixel pitch	7.4 $\mu\text{m}$	30 $\mu\text{m}$
Spatial pixel count	1600	320
Camera output	12 bit	14 bit
Lens focal length	23 mm	22.5 mm



Figure 4.4: VNIR (background) and SWIR (foreground) HSI cameras attached to a tripod-mounted rotation stage. The cameras can be rotated vertically as well as horizontally.

approximately square pixels were created, i.e., the instantaneous field of view of each pixel neither overlapped nor left voids between successive linear array exposures. Given the differing spatial resolutions of the cameras, which is a function of the linear array pixel size and lens focal length, images with each camera were acquired sequentially using different stage rotation rates. Further details regarding the camera and stage geometry are given in Chapter 6. The cameras were positioned approximately 41 m from the east quarry wall, which equates to minimum pixel sizes of 13 mm and 55 mm for the VNIR and SWIR cameras. The quarry wall was imaged in the morning, mid-day, and afternoon to capture the wall in full shade, partial shade, and maximum sun exposure conditions. These 6 images will be referred to as VNIR-shade, VNIR-partial, VNIR-sun, SWIR-shade, SWIR-partial and SWIR-sun hereafter. All images were collected at full spatial resolution. The VNIR imagery was collected at half spectral resolution to reduce the file sizes. One hundred frames (a frame is a single linear array exposure) were collected with the lens cap installed immediately following each image acquisition to record dark current levels for removal during image calibration.

### **4.2.3 Analysis Area Selection**

Since the primary interest is the outcrop surface, the point and mesh products were trimmed to exclude the vegetation growing on top of the outcrop and to exclude the floor of the quarry. The left edge of the analysis area was chosen to align with the location where all images had stabilized (the camera stage vibrates on startup) and the right edge chosen based on the minimum termination location of all the images. Figure 4.5 shows the complete SWIR-sun 1549 nm band image and the same image masked to match the analysis area. The

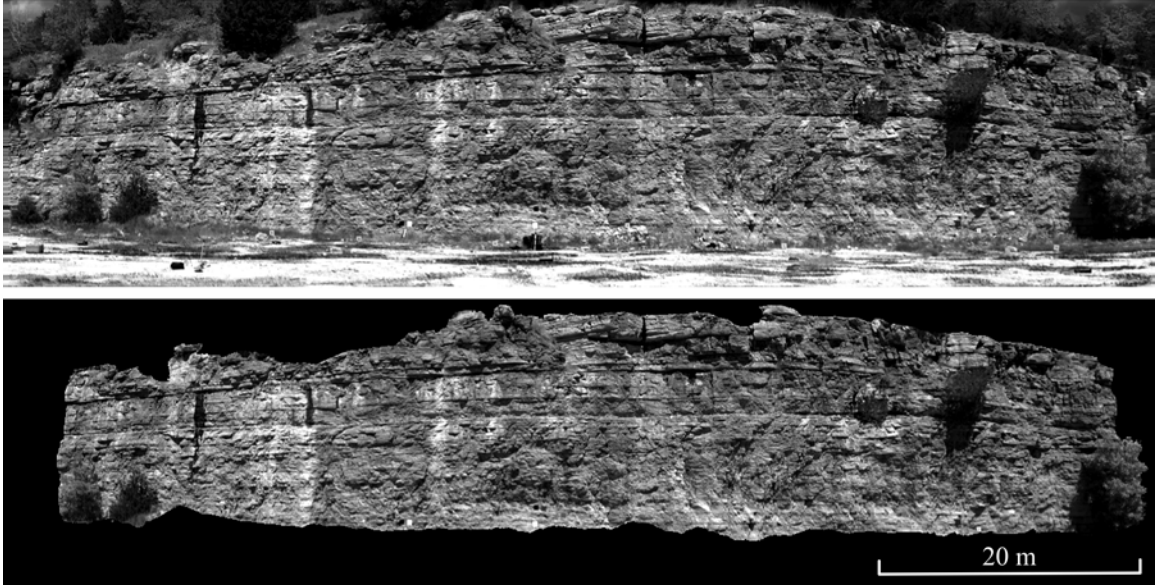


Figure 4.5: Maximum sun SWIR 1549 nm band image (top), and the same image masked to the analysis extents (bottom).

portion of the outcrop contained within the analysis area is approximately 78 m in length and 14 m in height.

## **Chapter 5**

### **Lidar and Hyperspectral Image**

#### **Radiometric Calibration**

The active lidar point intensities and passive HSI were converted to common units of reflectance percentages, enabling their direct combination in shadow restoration algorithms. The lidar radiometric calibration methods are reviewed first, with both the Leica HDS3000 and Riegl VZ-400 calibrations utilizing empirical observations of multiple reflectance standards. The observations form the sole basis of the HDS3000 calibration, but are incorporated into an existing onboard factory calibration for the VZ-400. The HSI radiometric calibration is then reviewed, with the primary step consisting of an EL conversion from DN to reflectance percentages using in situ observations of multiple reflectance standards.

### **5.1 Lidar Radiometric Calibration**

#### **5.1.1 Leica HDS3000**

Square Spectralon (Labsphere 2013) panels measuring 12 in on each side with nominal reflectance values of 2%, 20%, 50% and 99% were observed at normal incidence at 14 ranges spanning 5-90 m. Per the paperwork accompanying the Spectralon panels, the hemispherical reflectance values of the panels at 532 nm (HDS3000 laser wavelength) are 1%, 20%, 48% and 99%. The average range and raw intensity of the lidar points falling on each target were stored in a LUT along with the target reflectance, allowing a reflectance to be interpolated for any subsequent range and intensity measurement. Curves for the average

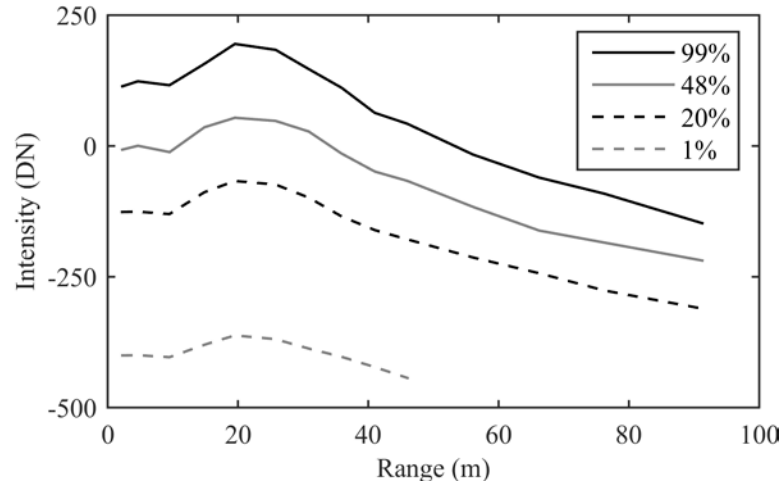


Figure 5.1: Leica HDS3000 radiometric calibration curves.

intensities and ranges are plotted in Figure 5.1. While the lower reflectance targets (1%, 20% and 48%) produce attenuated intensity curves that are symmetric with the 99% curve, the curves are not linearly proportional to the target reflectance values. For example, the 48% curve is much closer to the 99% curve than to the 1% curve, rather than approximately midway. This motivates the use of an empirical radiometric calibration rather than a physical approach, which would require knowledge of sensor nonlinearity characteristics.

### 5.1.2 Riegl VZ-400

Observations necessary to radiometrically calibrate a Riegl VZ-400 instrument belonging to the University of Houston in the same manner as the Leica HDS3000 were obtained in three separate campaigns in 2012 and 2013 as part of other research tasks. However, the instrument was not available when collecting the lidar information used in this dissertation, and a loaned VZ-400 instrument was used in its place. Rather than collect an extensive set of calibration measurements with the loaned instrument, the manufacturer supplied onboard radiometric calibration measurements with the loaned instrument, the manufacturer supplied onboard radiometric calibration was adjusted and used. The onboard radiometric calibration technique

is reviewed, its performance evaluated, and the method used to adjust the onboard calibration presented in the following sections.

#### 5.1.2.1 Technique

Each Riegl V-line TLS system is delivered with a factory supplied empirical radiometric calibration that uses an onboard LUT to relate raw peak amplitudes to calibrated amplitudes (Pfennigbauer and Ullrich, 2010). The calibrated amplitude is the logarithm of the ratio of the measured optical power  $P_{echo}$  to a minimum detectable optical power level  $P_{DL}$  and is given as

$$A_{dB} = 10 \log \left( \frac{P_{echo}}{P_{DL}} \right), \quad (5.1)$$

where  $A_{dB}$  is in decibels (dB). Optical power levels incident on the detector are varied in order to span the instrument's dynamic range, resulting in a LUT of calibrated amplitudes corresponding to any subsequently measured raw peak amplitude. Note that the calibrated amplitudes are related to actual measured optical power levels, meaning they should be free of nonlinear sensor response characteristics (Pfennigbauer et al., 2013). To generate reflectance measures independent of distance, calibrated amplitude values from observations of a nearly 100% reflective diffuse target are stored in an additional LUT for a series of target ranges. The reflectance is then computed in dB as the difference between the calibrated amplitude of a measured target and the stored calibrated amplitude of the white reference target at the same range,

$$\rho_{dB} = A_{dB} - A_{dB,Ref} = 10 \log \left( \frac{P_{echo}}{P_{DL}} \right) - 10 \log \left( \frac{P_{Ref}}{P_{DL}} \right) = 10 \log \left( \frac{P_{echo}}{P_{Ref}} \right). \quad (5.2)$$

Note that  $\rho_{dB}$  can be converted back to a power ratio and multiplied by 100 to produce relative reflectance values in the more traditional percentage domain as

$$\rho_{\%} = 100 \times 10^{\left(\frac{\rho_{dB}}{10}\right)}. \quad (5.3)$$

### 5.1.2.2 Evaluation

Using data previously acquired with a different VZ-400 TLS than used in this dissertation, the performance of the onboard factory calibration technique defined in Equations (5-1) through (5-3) is evaluated with respect to observations of the 20%, 50% and 99% Spectralon panels in Figure 5.2. The reported hemispherical reflectance values of the targets at the 1550 nm VZ-400 laser wavelength are 30%, 62% and 99%. The Spectralon panels were observed at normal incidence at 37 ranges spanning 2-260 m in June 2012, and at 62 ranges spanning 2-400 m on two occasions in May 2013 (referred to as 2013a and 2013b). The curves plotted in Figure 5.2 display an anomaly centered at ~10 m, which corresponds to optical defocusing at near ranges (Fang et al., 2015), and exhibit increasing fluctuation beyond 200 m. Although the reflectance values are relatively stable between 20 and 200 m range, which is where the majority of outcrop observations used in this

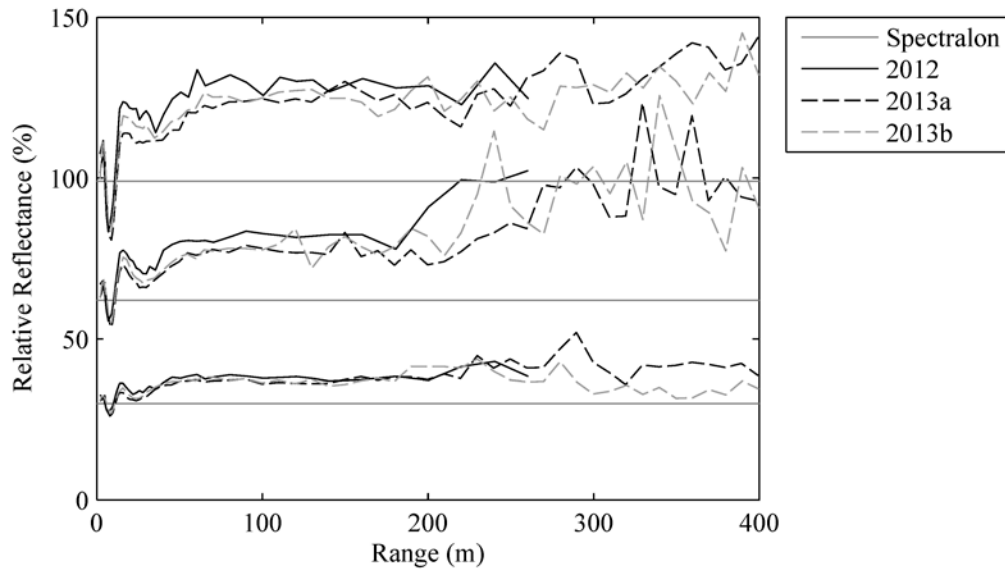


Figure 5.2: Reflectance produced by the VZ-400 factory calibration compared to the quoted Spectralon panel reflectance.

dissertation exist, they are biased with respect to the Spectralon reflectance values.

### 5.1.2.3 Adjustment

Most of the bias in the onboard radiometric calibration can be removed by inserting the calibrated amplitudes reported by the instrument for the 99% Spectralon panel measurements into Equation (5-2) for the term  $A_{db,Ref}$ , thereby forming an updated radiometric calibration exactly corresponding to the method used by the onboard factory calibration. An example using the May 2013b dataset is given in Figure 5.3. The root mean square error (RMSE) between the adjusted reflectance values and the 30% and 62% Spectralon panels is 1.6% and 2.5% for the ranges spanning 5-140 m, which is the range interval required for calibrating the outcrop data analyzed in this dissertation. Note that an adjusted curve for the observations of 99% Spectralon is not given, as these observations are assumed errorless in the adjustment.

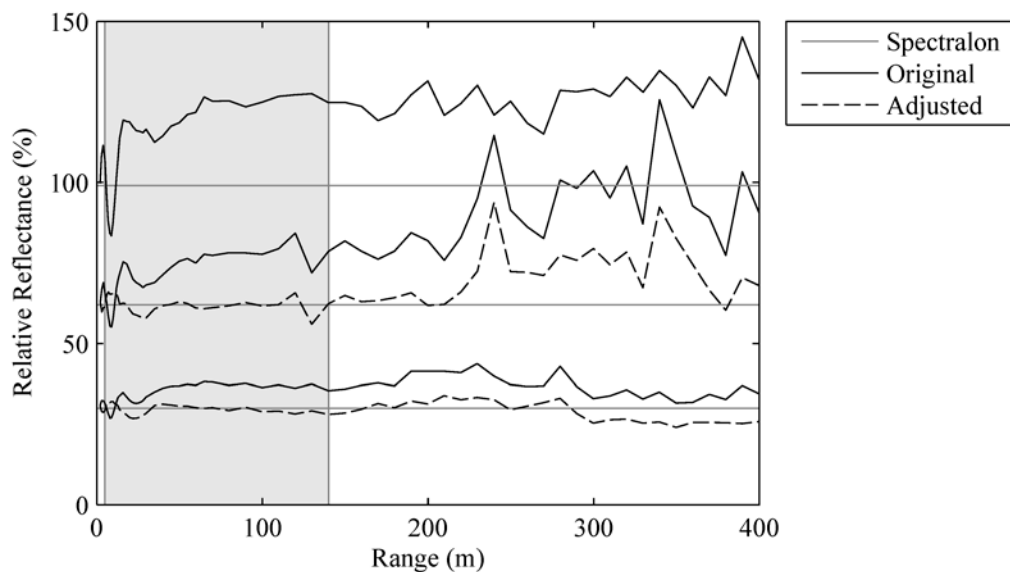


Figure 5.3: Factory radiometric calibration adjustment using an updated calibrated amplitude for the white reference. The 2013b dataset is shown. The shaded area indicates the range interval of interest.

By using a spline interpolator, a sparse set of observations of the 99% Spectralon panel is sufficient to model the calibrated amplitudes required to adjust the factory calibration. This is illustrated in Figure 5.4, where a spline curve generated from 10 measurements of the 99% Spectralon panel from the 2013b calibration campaign in the range interval 5-140 m is overlaid on the complete data containing 33 measurements. Use of the spline interpolated curve produced RMSE values of 1.7% and 2.6% between the adjusted reflectance values and the 30% and 62% Spectralon panels, which is almost identical to the prior results that used the complete set of measurements. Therefore, the onboard radiometric calibration of the Riegl VZ-400 used in this dissertation was adjusted using calibrated amplitudes generated from relatively sparse observations of the 99% Spectralon panel consisting of 12 ranges between 5 and 140 m. Observations of the 62% and 30% Spectralon panels were also collected to confirm the performance of the adjustment, with resultant RMSE values of 1.8% and 1.0%.

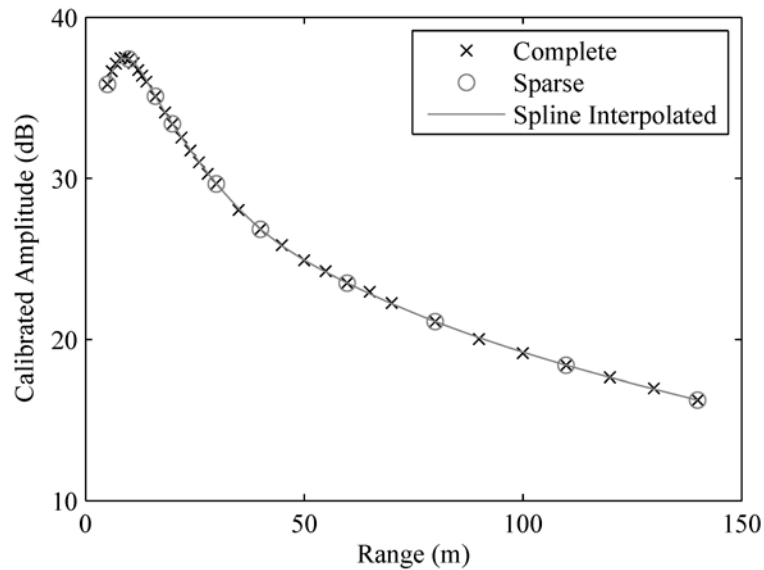


Figure 5.4: Spline interpolation of sparse calibrated amplitudes to reconstruct complete curve.

### **5.1.3 Calibration Uncertainty**

The curves generated from the multiple VZ-400 calibration campaigns shown in Figure 5.2 illustrate the uncertainty in radiometrically calibrated TLS products due to the following:

1. unknown target hotspot characteristics that can produce systematic offsets,
2. heterogeneity in calibration target composition,
3. variable transmit power and receiver sensitivity as a function of temperature and receiver noise,
4. long term sensor temporal stability, and
5. variable atmospheric conditions that influence the transmission of optical power, producing both random and systematic error.

These uncertainties make direct identification of target material by matching lidar-derived reflectance values with pre-existing or in situ passive spectral reflectance measurements a challenging task (Hartzell et al., 2014, 2015). However, work in Hartzell et al. (2015) has shown that radiometrically calibrated reflectance from TLS observations of non-specular extended targets can be self-consistent to within 5%, which corresponds with the calibration results in the range interval of interest (5-140 m).

## **5.2 Hyperspectral Image Radiometric Calibration**

To begin, a mean frame was computed from each set of dark current frames and subtracted from its corresponding outcrop image to remove subtle image banding produced by inconsistent detector signal in the absence of incident photons. Bad lines, which are random distinct stripes in image bands due to detector non-uniformity not accommodated by the factory supplied non-uniformity correction tables, still remained in many bands. The bad

lines were detected and replaced using a method similar to that found in Han et al. (2002), wherein lines with a certain percentage of pixels consistently brighter or darker than pixels in adjacent lines are identified as bad lines and replaced by the average of the adjacent lines. The outcrop HSI images were then converted from DN to reflectance using the EL method. Mean spectra were computed from image pixels containing the 2% and 99% reflectance Spectralon targets (placed at the base of the outcrop in each image) and used to solve for the required gain and offset values for each image wavelength band. Finally, noisy bands in the spectrum extremities of the VNIR (<411 nm, >850nm) and SWIR (<922 nm, >2447 nm) images and the SWIR bands subject to atmospheric water absorption (1334-1460 nm, 1788-1958 nm) were removed from each HSI data cube.

After completion of the steps outlined in the prior paragraph, the full shade images contained a vertical brightness gradient with respect to the outcrop, being much brighter at the top than the bottom (Figure 5.5). The gradient is correlated with the distance from direct sunlight, which increases from the top of the outcrop to the bottom, and is roughly exponential when compared to the maximum sun images. This suggests the gradient is due to extinction of light scattered from the direct solar radiation, which should decrease exponentially with distance when traveling through a continuous scattering and absorbing medium (the atmosphere) according to Beer's Law (Eismann, 2012). The gradient was removed from each band of the full shade images by first fitting an exponential curve via least squares to data points defined by the ratio of the mean of each maximum sun image line (i.e., the mean of each image row was computed) to the corresponding full shade image line means. Each line of the full shade band was then multiplied by the appropriate point on the best-fit exponential curve of ratio values. The change between an original and adjusted full

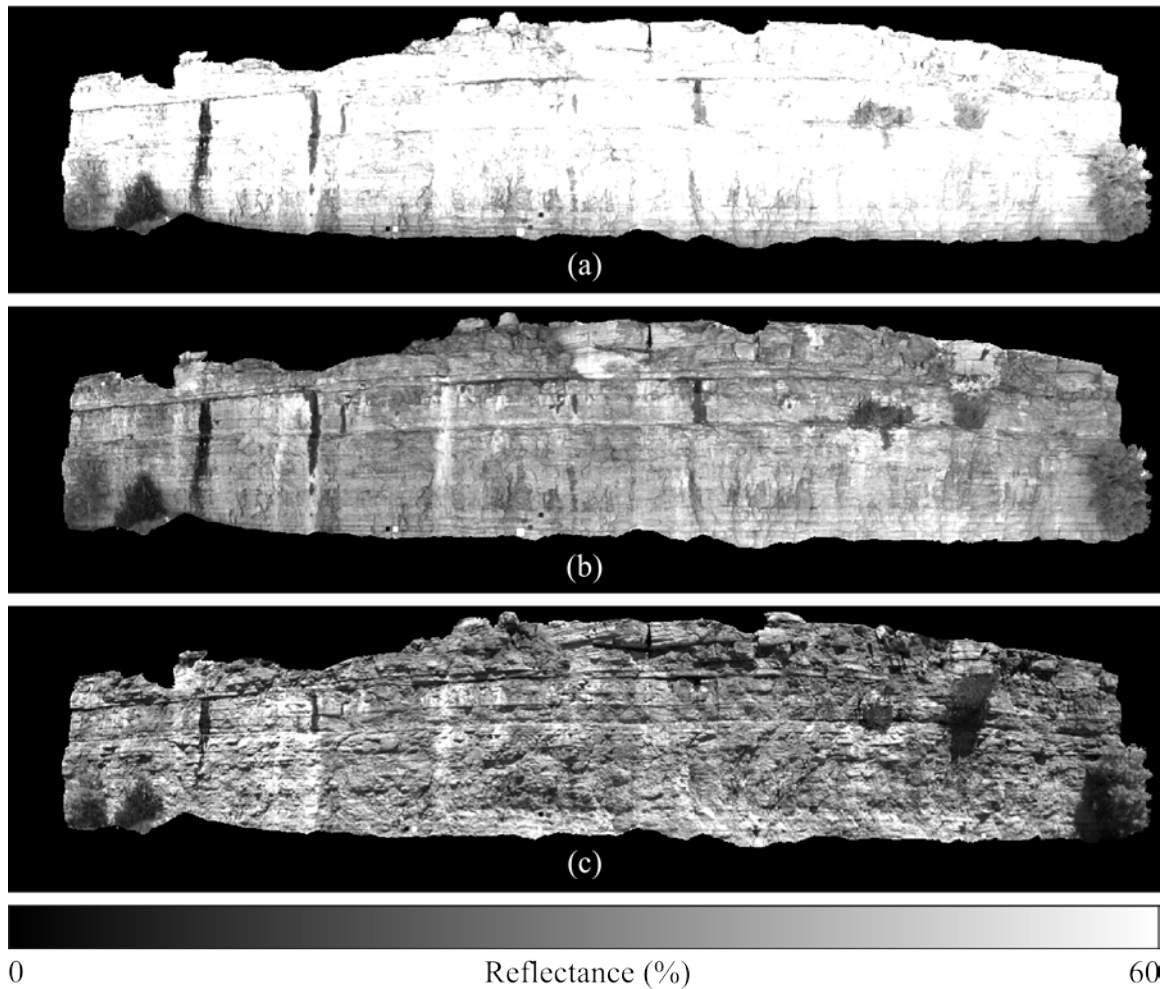


Figure 5.5: (a) Original calibrated SWIR-shade 1549 nm band; (b) adjusted SWIR-shade 1549 nm band; (c) SWIR-sun 1549 nm band.

shade image is shown in Figure 5.5(b). Note that the adjusted full shade image is free of most shadow and topographic effects, making the outcrop material features more visible than in the corresponding maximum sun image (compare parts (b) and (c) of Figure 5.5). However, the original and adjusted full shade HSI pixel spectra are much different than their corresponding maximum sun counterparts. Therefore, the bands of the adjusted full shade HSI are used to quantify the band-wise spatial quality of the shadow restoration results found in Chapter 7, but not for any measures dealing with spectral shape or magnitude.

Finally, readers familiar with standard remote sensing image correction techniques will note the absence of a topographic cosine correction applied to the HSI. A topographic correction does “flatten” the appearance of the HSI as expected, but also introduces random speckled error in the images as a result of imperfect surface normal estimates. The introduction of this additional random error negatively influences the shadow restoration algorithms detailed in Chapter 7 and a topographic correction was therefore not applied to the HSI.

## Chapter 6

### Active and Passive Data Fusion

The combination of the radiometrically calibrated lidar and HSI data, i.e., fusion, is realized by projecting object space lidar point coordinates  $(X, Y, Z)$  through a camera model into image pixel space coordinates  $(u, v)$ . To date, most of the terrestrial HSI applied to geologic studies has been collected with panoramic linear array sensors that rotate around a vertical axis intersecting the camera optical centerline, thus forming a standard cylindrical model (Schneider and Maas, 2006; Kurz et al., 2011). The optical centerlines of the VNIR and SWIR cameras used in this dissertation, however, are offset from the rotation axis by ~20 cm. Furthermore, both cameras can be inclined vertically (Figure 6.1) prior to horizontal rotation in order to maximize coverage of vertical structures at close proximity. A more appropriate camera model is found in Scheibe et al. (2009), where the offset optical axis is explicitly accommodated. The camera models developed for this dissertation are geometrically similar to those presented in Scheibe et al. (2009), with the following differences:

1. The camera vertical rotation angle is explicitly included in the model rather than being considered a geometric imperfection.
2. Knowledge of either the horizontal rotation angle at each linear array exposure station or the angular increment between successive linear array exposures is not required.

The chapter begins with a derivation of the camera model and calibration of several fixed interior orientation (IO) parameters. The method and quality of the solutions for the

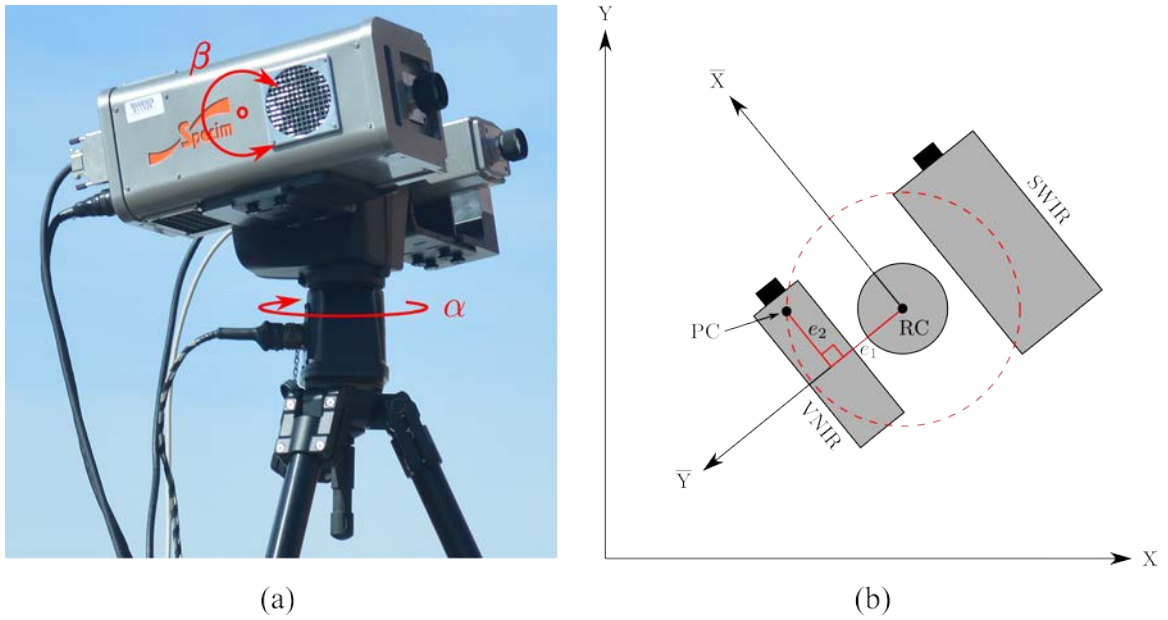


Figure 6.1: (a) VNIR and SWIR (foreground) HSI cameras and rotation stage. (b) Illustration of the disk swept by the VNIR camera projection center (PC) as it revolves around the rotation center (RC). Linework is not to scale.

remaining camera IO and exterior orientation (EO) parameters necessary to fuse each HSI with the lidar point cloud are then detailed, followed by a review of several image products that utilize the camera model.

## 6.1 Camera Model

A camera model is a mathematical construct that describes the physical orientation of the sensor in 3D object space (EO) and the interior geometry of the camera and image coordinate systems (IO) such that any object space location can be transformed into image space. The VNIR camera model is derived in the following subsections by defining the transformations necessary to project a 3D object space coordinate to a 2D pixel coordinate pair. Four coordinate systems are used: object ( $X Y Z$ ), camera ( $\bar{X} \bar{Y} \bar{Z}$ ), image ( $x' y'$ ) and pixel ( $u v$ ). See

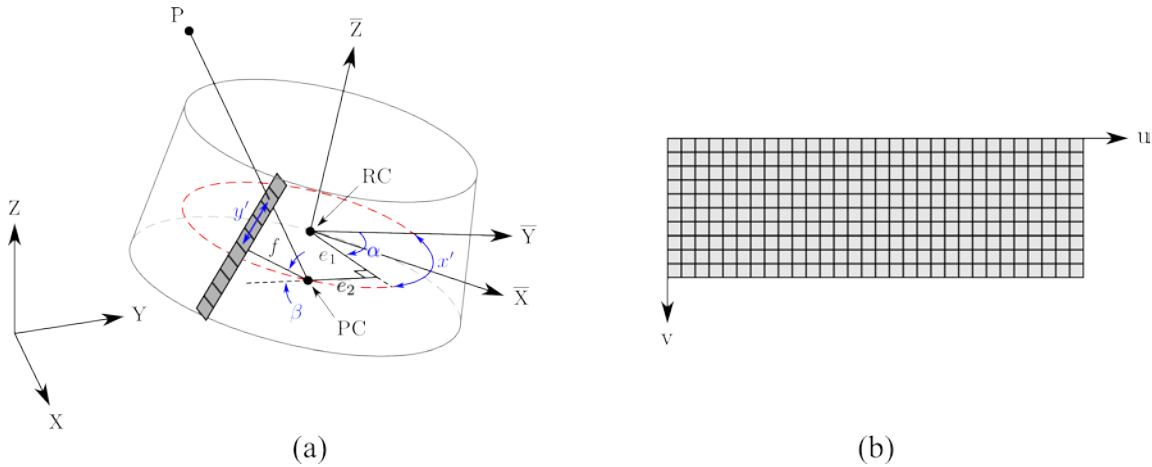


Figure 6.2: (a) Object ( $X Y Z$ ), camera ( $\bar{X} \bar{Y} \bar{Z}$ ) and image ( $x' y'$ ) coordinate systems. (b) Pixel ( $u v$ ) coordinate system. Linework is not to scale.

Figures 6.1 and 6.2. The SWIR camera model is similar and therefore is not explicitly derived here.

### 6.1.1 Basic Model

#### 6.1.1.1 Object Space to Camera Space

Object space is defined by an arbitrary Cartesian coordinate system. Examples include the local coordinate system defined by a TLS scanner position or a georeferenced projection such as the Universal Transverse Mercator (UTM) system. We define camera space to be a Cartesian coordinate system fixed in object space with an origin at the intersection of the horizontal rotation axis and the circular disk swept by the rotating camera projection center (PC), see Figures 6.1 and 6.2. The camera coordinate system is oriented with the  $\bar{Z}$ -axis coincident with the rotation axis and pointing upwards, the  $\bar{X}$ -axis parallel to the line formed by the orthogonal projection of the camera optical axis at the first exposure station onto the disk swept by the rotating PC and the  $\bar{Y}$ -axis forming a right-handed system. The object

space coordinates of a point P  $(X, Y, Z)$  are transformed into camera space coordinates  $(\bar{X}, \bar{Y}, \bar{Z})$  with a 6-parameter rigid-body transformation,

$$\begin{bmatrix} \bar{X} \\ \bar{Y} \\ \bar{Z} \end{bmatrix} = \mathbf{R} \begin{bmatrix} X - X_0 \\ Y - Y_0 \\ Z - Z_0 \end{bmatrix}, \quad (6.1)$$

where  $X_0, Y_0$  and  $Z_0$  are the object space coordinates of the camera space origin and  $\mathbf{R}$  is a 3D rotation matrix derived from the  $\omega, \phi$  and  $\kappa$  rotation angles about the X, Y and Z axes given as

$$\mathbf{R} = \begin{bmatrix} \cos \kappa \cos \phi & \sin \kappa \cos \omega + \cos \kappa \sin \phi \sin \omega & \sin \kappa \sin \omega - \cos \kappa \sin \phi \cos \omega \\ -\sin \kappa \cos \phi & \cos \kappa \cos \omega - \sin \kappa \sin \phi \sin \omega & \cos \kappa \sin \omega + \sin \kappa \sin \phi \cos \omega \\ \sin \phi & -\cos \phi \sin \omega & \cos \phi \cos \omega \end{bmatrix}. \quad (6.2)$$

$\mathbf{R}$  is defined here using axis rotation, as opposed to point rotation, with a  $\kappa$ - $\phi$ - $\omega$  rotation order and positive counter-clockwise angles when viewing along an axis toward the origin.

#### 6.1.1.2 Camera Space to Image Space

The transformation of a 3D point from camera space to image space consists of separate horizontal and vertical components. Image coordinates are defined by the horizontal distance  $x'$  along the exterior of a disk with a radius equal to the camera focal length (coinciding with the disk swept by the camera projection center) and the vertical distance  $y'$  along the linear array as shown in Figure 6.2.

If we assume a camera rotation speed and linear array exposure rate such that square pixels are created, i.e., we are neither oversampling and creating a horizontally stretched image, nor undersampling and creating a horizontally compressed image, then  $x' = f\alpha$ , where  $f$  is the camera focal length and  $\alpha$  is the total angle the camera has rotated from its starting position (Figure 6.2). The solution for  $\alpha$  is dependent on the interior orientation

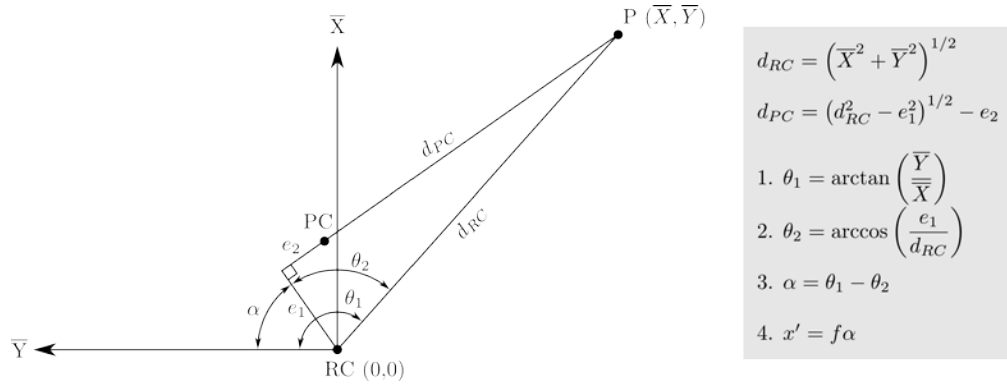


Figure 6.3: Transformation from camera space to horizontal image space ( $x'$ ). The computation of  $d_{PC}$  is shown for subsequent use in the vertical transformation computations in Figure 6.4. Linework is not to scale.

parameter  $e_1$ , which, together with  $\alpha$  and  $e_2$ , defines location of the camera projection center with respect to the  $\bar{X}$  and  $\bar{Y}$  axes. The complete solution for  $x'$  is given in Figure 6.3.

The solution for  $y'$  follows the standard pinhole camera model and is given in Figure 6.4. It requires the interior orientation parameter,  $\beta$ , which is the angle between the camera optical axis and the  $\bar{X}$ - $\bar{Y}$  plane.

### 6.1.1.3 Image Space to Pixel Space

Image space coordinates ( $x', y'$ ) are transformed to pixel space coordinates ( $u, v$ ) by

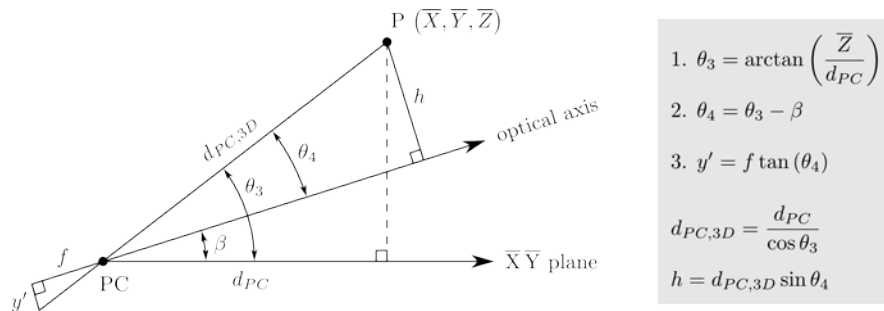


Figure 6.4: Transformation from camera space to vertical image space ( $y'$ ). Computations for  $d_{PC,3D}$  and  $h$  are required for the linear array tilt corrections given in Figure 6.5. Linework is not to scale.

dividing  $x'$  and  $y'$  by the linear array pixel pitch (physical CCD pixel size) as

$$u = \frac{x'}{pitch} \text{ and} \quad (6.3)$$

$$v = \frac{array\ size}{2} - \frac{y'}{pitch}. \quad (6.4)$$

Since  $y'$  values can be either positive or negative (above or below the center of the vertical linear array), the origin of the vertical pixel values is shifted to the top of the array in Equation (6.4).

### 6.1.2 Additional Parameters

The VNIR camera model summarized in the prior section assumes ideal geometric relationships, such as the linear array being perfectly orthogonal to the  $\bar{X}$ - $\bar{Y}$  plane and no lens distortion. The following sections review additional parameters that are added to the basic model in image space in order to correct geometric and optical imperfections. The additional parameters that follow are not exhaustive, as some imperfections are not recoverable due to high correlation with other model parameters. For example, a principal point offset along the linear array could not be recovered due to high correlation with the camera vertical inclination angle  $\beta$ .

#### 6.1.2.1 Linear Array Tilt - $\gamma$

Linear array tilt refers to the rotation of the linear array about the optical axis, which violates the model assumption of orthogonality with respect to the  $\bar{X}$ - $\bar{Y}$  plane when viewing the linear array along the optical axis. This is a result of manufacturing imperfections in the rotation stage and mounting hardware as well as sag due to camera weight. Corrections to the horizontal and vertical image space coordinates for  $\gamma$  are derived in Figure 6.5.

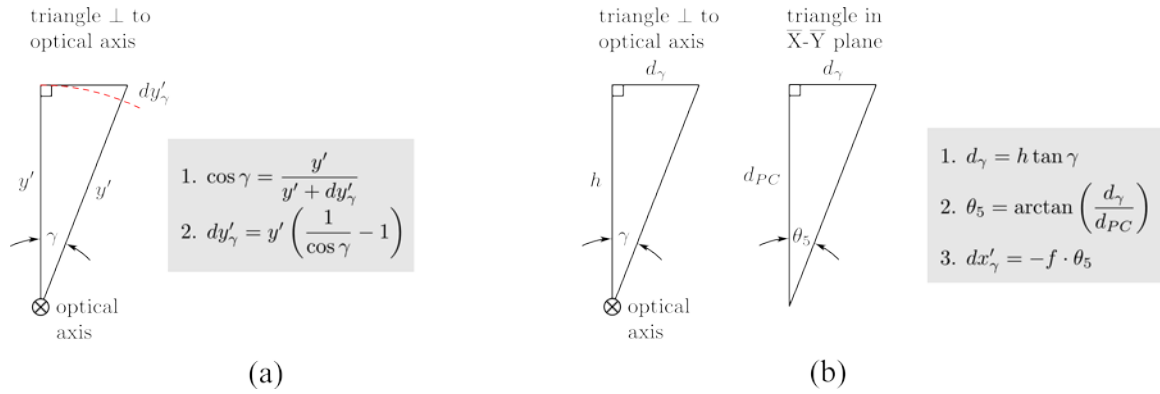


Figure 6.5: (a) Vertical and (b) horizontal components of linear array tilt additional parameter in image space.

### 6.1.2.2 Pixel Affinity - $S$

The base camera model assumes a dimensionally consistent image, i.e., one that appears neither horizontally stretched nor compressed. This requires the camera rotation and exposure rates to be chosen such that the horizontal angle traversed between successive exposures,  $\Delta\theta$ , is equal to the vertical field of view seen by each pixel in the linear array. This is impossible to achieve in practice as the camera rotation rate is not infinitely adjustable. Therefore, a scale factor  $S$  is required to adjust  $x'$  prior to conversion to pixel space. The additional parameter equation is

$$dx'_S = Sx'. \quad (6.5)$$

### 6.1.2.3 Radial Lens Distortion - $k_1$ and $k_2$

Radial lens distortion only impacts the vertical image coordinates in a linear array camera sensor. Inserting  $y'$  as the radial distance, a standard polynomial expression for radial lens distortion is  $dy'_r = k_0y' + k_1y'^3 + k_2y'^5 + k_3y'^7$  (Luhman et al., 2011). The fourth term is rarely necessary unless the lens distortion is severe and is not used. The first term is highly

correlated with the interior orientation parameters  $f$  and  $e_2$  and was not recoverable. The final lens distortion additional parameter equation is

$$dy'_r = k_1 y'^3 + k_2 y'^5, \quad (6.6)$$

with  $k_1$  and  $k_2$  the required additional parameters. It is noted that a second zero crossing,  $r_0$ , of the distortion curve is often introduced to avoid the numerical correlation with  $f$  (Schneider and Maas, 2006; Luhman et al., 2011), which results in  $dy'_r = k_1 y' (y'^2 - r_0^2) + k_2 y' (y'^4 - r_0^4)$ . However, this method did not produce any noticeable improvements herein when compared to allowing  $f$  and  $e_2$  to absorb the linear portion of the distortion curve.

### 6.1.3 Model Summary

The final image space coordinates that accommodate the relevant additional parameters are given as

$$x'_{AP} = x' + dx'_\gamma + dx'_S \text{ and} \quad (6.7)$$

$$y'_{AP} = y' + dy'_\gamma + dy'_r. \quad (6.8)$$

Note that  $x'_{AP}$  and  $y'_{AP}$  are the actual values inserted into Equations (6.3) and (6.4) when converting from image space to pixel space.

## 6.2 Model Calibration and Image Registration

### 6.2.1 Model Calibration

The camera model contains 14 parameters that must be solved in order to project 3D object space coordinates into pixel space. Of these, only three are assumed stable and able to be permanently fixed by calibration; the remaining parameters are unique to each image collection, see Table 6.1. A 3D array of 35 targets encircling the VNIR and SWIR cameras

Table 6.1: Camera model parameter summary.

<b>Group</b>	<b>Parameters</b>
Exterior Orientation	$X_0, Y_0, Z_0, \omega, \phi, \kappa$
Interior Orientation	$\beta, f, *e_1, e_2$
Additional Parameters	$\gamma, S, *k_1, *k_2$

\*Stable parameter

was observed in July 2014 to validate the camera model and calibrate the three fixed parameters. The targets consisted of 6 inch diameter checkerboard patterns printed on 8.5 inch by 11 inch foam board and were placed at ranges from 4 to 28 m from the cameras. The target 3D locations were obtained from a Riegl VZ-400 TLS scan, with point densities ranging from 60 points/cm<sup>2</sup> for very close targets to 1.3 points/cm<sup>2</sup> for the most distant targets. Target pixel densities ranged from 62 to 1.2 pixels/cm<sup>2</sup> and 3.6 to 0.1 pixels/cm<sup>2</sup> for the near and far VNIR and SWIR images, respectively.

Camera model observation equations expressing pixel space coordinates as a function of observed 3D point coordinates and the unknown model parameters were used in a least squares adjustment to solve for the model parameters through space resection of a single image. Residual standard deviations of one pixel or less were achieved for both the VNIR and SWIR models with simple closest point picking of the target centers in object space and pixel space. Given the small size and approximate normal distribution of the residuals, see Figure 6.6, modeling of the target centers for increased precision was not deemed necessary. Note that the larger VNIR residuals are a natural result of the increased pixel resolution of the VNIR HSI compared to the SWIR, i.e., an equivalent object space error in picking a target center is magnified when expressed at the finer spatial scale of the VNIR pixels compared to the SWIR.

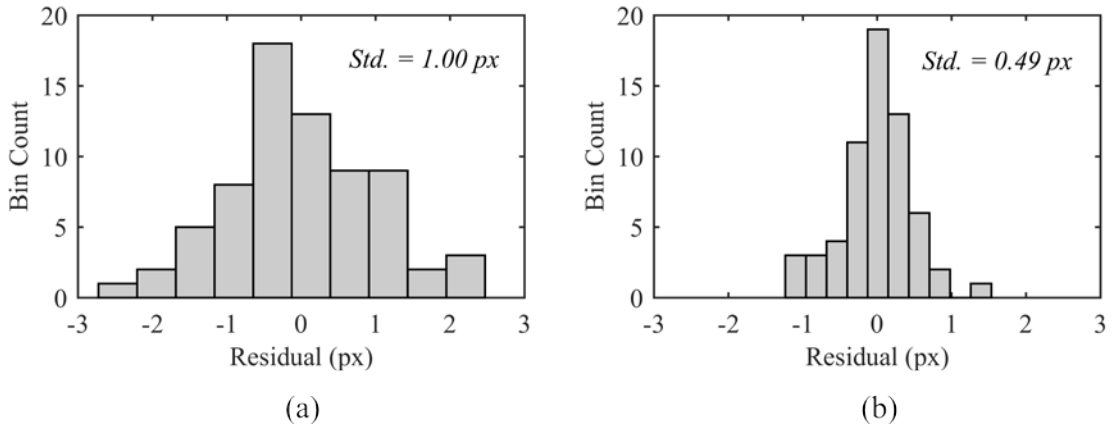


Figure 6.6: (a) VNIR calibration residuals. (b) SWIR calibration residuals.

### 6.2.2 Image Fusion

The camera IO and EO parameters necessary to fuse, i.e., register, each panoramic HSI with the TLS point cloud are solved in the same manner as the calibration method above. The a priori calibrated values for  $e_1$ ,  $k_1$  and  $k_2$  were held fixed in each least squares adjustment, which has the benefit of increasing the adjustment redundancy. No less than 19 points, evenly spaced along the base, middle and top of the outcrop, were selected in each HSI and their corresponding locations identified in the TLS point cloud. The image and object space coordinates were extracted via automated methods from signalized targets placed at the base of the outcrop, while those points in the middle and top of the outcrop were manually selected through identification of common features in the HSI and point cloud. Adjustment standard deviations were less than 0.3 pixel for the SWIR images and less than 0.9 pixel for the VNIR images.

## 6.3 Fusion Products

With the IO and EO parameters solved, the six HSI were co-registered to a common master pixel coordinate system. This eases the comparison of corrected shadow pixels to their fully illuminated counterparts existing in different HSI images and also allows the VNIR and SWIR imagery to be stacked into a single data cube, although this should be done with caution since the VNIR and SWIR images are not captured simultaneously and thus exhibit different shadow patterns. The active reflectance information was also rasterized to the common pixel system and segmented to assist in the shadow restoration algorithms detailed in Chapter 7.

### 6.3.1 Co-Registered HSI

The SWIR-sun HSI was chosen to be the master image. The first step in co-registering a slave image to the master image is to obtain 3D object space coordinates corresponding to each master HSI pixel. This requires an inverse solution to the camera model defined in Section 6.1, i.e., we are given pixel coordinates  $(u, v)$  and must solve for their corresponding object space  $(X, Y, Z)$  coordinates. A direct solution is not possible unless a photogrammetric approach employing multiple convergent images is used; however, the 3D vector passing through the camera projection center and exiting the camera, i.e., a camera ray, can be computed for individual images for each  $(u, v)$  pixel coordinate. The intersection of the camera ray and the 3D mesh in object space provides the required corresponding 3D object space coordinate. Each camera ray was tested for intersection with each triangle of the mesh using the method defined in (Möller and Trumbore, 1997) and the intersection closest to the camera stored. To speed computation, the mesh was partitioned into voxels defined by the

camera ray azimuth and zenith angles and only those triangles in the same voxel as the camera ray in question tested for intersection. Note that the inverse camera model used to generate the camera rays will not be derived here, as it is simply a mathematical manipulation of the previously defined camera model.

The 3D object space coordinates corresponding to the master image pixels were then projected into the slave image using the camera model directly, thereby establishing the relationship between the slave and master images. When registering the SWIR images, a 2D cubic interpolation of pixel brightness values was used in a band-by-band fashion to extract the slave image spectra. This mitigated the spatial artifacts and blurring that occurs in techniques that do not approximate the underlying continuous image in the resampling process, such as nearest neighbor or weighted average methods. Note that resampling is necessary, even between SWIR images of the same spatial resolution, because the slave and master pixels do not have a 1:1 correspondence due to the camera being moved between the different image acquisitions. When registering the VNIR images, the master pixel “corner” coordinates were projected into the slave images and the mean weighted spectrum falling within the box created by the pixel corners used to create the registered image. In contrast to the SWIR imagery, no blurring was evident in this technique due to the much higher resolution of the VNIR HSI in comparison to the SWIR.

The use of the mesh outcrop surface to define the 3D object space coordinates, rather than a synthetic surface such as a plane or a cylinder, has the advantage of producing images that are “trimmed” to the area of interest defined by the mesh. Pixel camera rays that do not intersect the mesh are assigned a null value, which eliminates the need to define a boundary mask for subsequent HSI image processing.

### 6.3.2 Rasterized and Segmented Active Reflectance

Raster images of the active reflectance were created by projecting each TLS point through the camera model utilizing the master image IO and EO parameters. Since the point cloud was generated from multiple TLS instrument setups not collocated with the HSI camera, it was necessary to test the visibility of each point with respect to the camera prior to projecting the point through the camera model. This was accomplished by testing the ray from each TLS point to the camera for intersection with the mesh surface. Using only those points not occluded with respect to the camera, the mean active reflectance for each pixel was computed to generate 532 nm and 1550 nm active reflectance images. Figure 6.7 shows the active reflectance images compared to the closest wavelength band in the corresponding VNIR and SWIR maximum sun HSI.

Several shadow restoration methods examined in Chapter 7 require selection of pixels, or regions of pixels, of similar material existing in both sun and shade. Active reflectance was used to assist in the selection, but was first segmented in order to limit the number of potential matches when searching for pixels of similar material and also for direct use when regions of similar materials are required. In contrast to the spatially heterogeneous results produced by traditional clustering techniques that operate on individual pixel brightness values, such as K-means, spatially connected regions (i.e., segments or blobs) are desirable since both spatial and spectral proximity are relevant indicators of common material location. This requires an algorithm that can tolerate a level of stochastic variability in adjacent active reflectance pixel brightness values while maintaining sensitivity to a mean bias in brightness at larger spatial distances. The mean shift algorithm by Comaniciu and Meer (2002) was chosen to meet these needs.

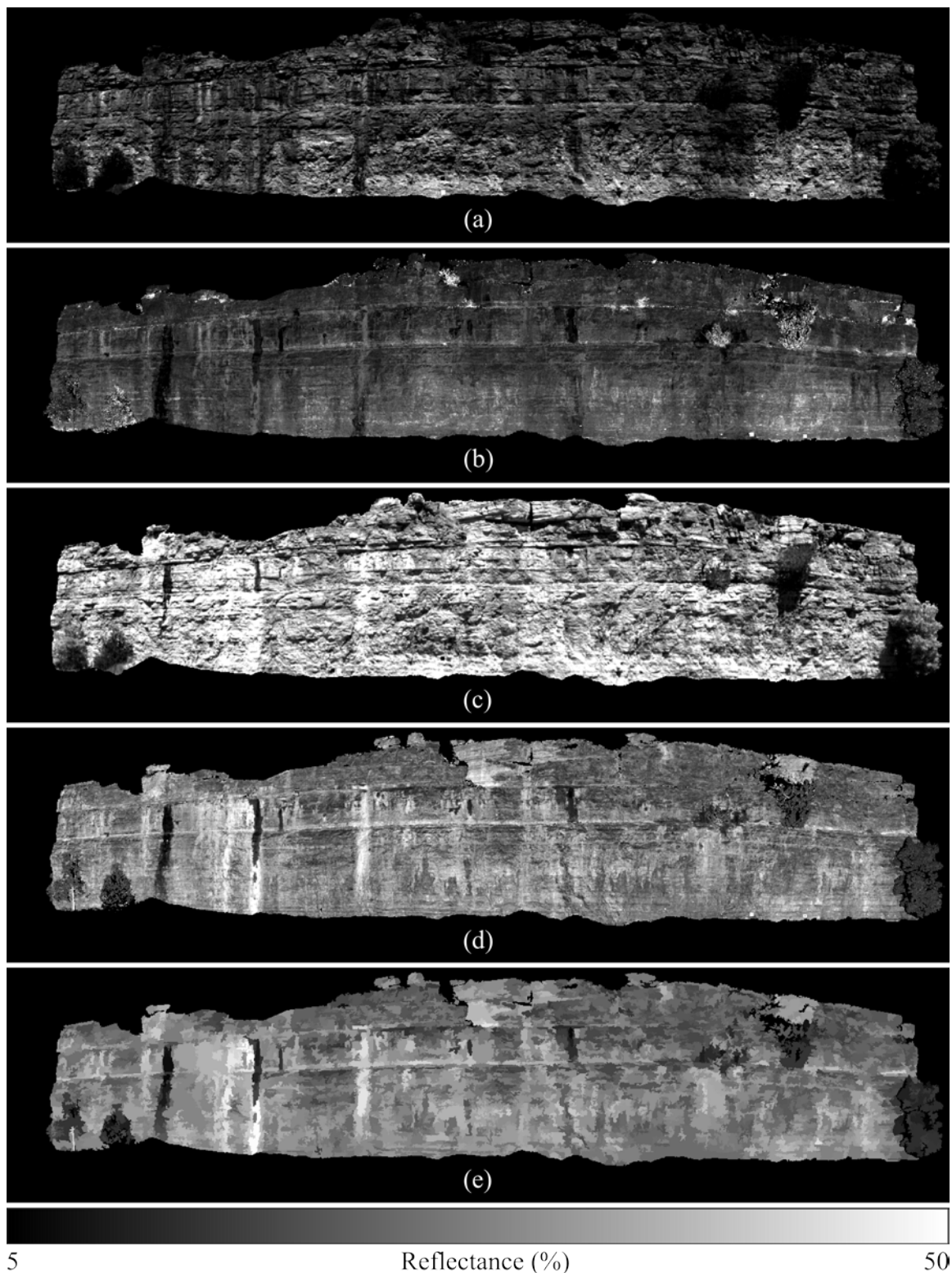


Figure 6.7: 532 nm passive (a) and 532 nm active (b) reflectance images. 1549 nm passive (c) and 1550 nm active (d) reflectance images. Mean shift segmented 1550 nm active reflectance image is shown in (e) using spatial and spectral (8-bit image) bandwidths of 20 and 1, respectively.

The mean shift algorithm is a nonparametric gradient ascent method that identifies the local modes of the underlying brightness density of an image (it treats image pixel brightness values as samples of a probability density function) and segments those pixels that are within each local mode's "basin of attraction". A kernel density estimator, i.e., Parzen window, can be used to estimate the brightness density at each pixel. However, by using a kernel that is the gradient of a density estimation kernel, a vector that is aligned with the direction of maximum increase in density is produced instead. The computed vector is used to successively shift the kernel until the gradient vector converges to zero at a local density mode (the gradient of a density mode is zero). The pixel from which the kernel originated is designated to exist within the basin of attraction of the converged local density mode and its brightness value replaced by the local mode's value. Repeated for each pixel, this has the effect of filtering the image. User input to the algorithm is limited to defining spatial (pixel) and spectral (brightness level) kernel bandwidths, which control the amount of smoothing. For the active reflectance images used in this dissertation, spatial bandwidths between 10 and 40 pixels and spectral bandwidths between 1 and 3 brightness levels (8-bit range) were used; higher values over-smoothed the images. Final segmentation of the filtered image is achieved by merging local attraction basins that are closer together in the spatial and spectral domains than the original bandwidths specified for the filtering operation. The algorithm was implemented using a MATLAB MEX wrapper around C++ source code available for download from the Rutgers University Robust Image Understanding Laboratory at <http://coewww.rutgers.edu/riul/research/code/EDISON/index.html>. A sample segmented 1550 nm active reflectance image created using spatial and spectral bandwidths of 20 and 1 is given in Figure 6.7(e).

## **Chapter 7**

### **Hyperspectral Image Shadow**

#### **Detection and Restoration**

With the fusion of the active and passive data products complete, the co-registered spatial and spectral information can be applied to shadow detection and restoration tasks. The chapter begins with a review of a fully 3D ray tracing shadow detection method that leverages the accurately georeferenced and very high resolution spatial information provided by the GNSS and TLS sensors. The influence of including active reflectance information in several existing shadow restoration algorithms is then examined, followed by an investigation of a technique that directly combines the active TLS and passive HSI spectral information. The analysis concludes with application of SAM, MD and ML classifiers to original and restored HSI images to illustrate the impact of restored spectral shape and magnitude characteristics on classification tasks.

#### **7.1 Shadow Detection**

Given the high resolution TLS spatial information and sub-pixel image registration results, a ray tracing technique was used with a fully 3D mesh surface (rather than a 2.5D DSM) to determine image pixel occlusion with respect to the sun direction. For each HSI exposure time, the local solar azimuth and zenith angles were computed following the method found in Reda and Andreas (2004). Using the inverse camera model in the same manner as reviewed in Section 6.3.1, rays were projected from the center of each pixel to the mesh surface and the nearest 3D point of intersection stored. A ray was then projected from

each mesh intersection point in the direction of the solar azimuth and zenith angles and again tested for intersection with the mesh surface. Those pixels with occluded solar rays were assigned as shadow pixels, resulting in a binary shadow image. Additional raster products containing fractional shadow assignments were also computed by projecting multiple (4, 9, 16 and 25) evenly spaced points from each pixel. Sample portions of a fractional shadow image based on four projected points per pixel are shown in Figure 7.1.

The shadow detection accuracy is difficult to quantify since it requires visual identification of exact shadow edges in the imagery, a task complicated by the dual influence of shadow and material differences on pixel brightness values. However, a visual comparison of well-defined shadow features suggests pixel-level accuracy across the surface of the outcrop. Several examples are given in Figure 7.1. This qualitative assessment is indirectly validated by a reduction in over- and under-corrected pixel brightness values produced by a scalar shadow restoration algorithm when using the fractional, rather than binary, shadow detection results. In particular, it was found that the majority of improvement is realized with four points per pixel. These observations are discussed further in Section 7.2.2.2.3. Finally, it is noted that the shadow detection method is not robust for vegetation, whose complex structure is not adequately modeled by the mesh surface in several locations.

In order to restore the shadowed pixel spectra using the algorithms examined in this dissertation, identification of distinct shadow areas is required. This is a problem for the SWIR-partial and VNIR-partial shadow images where close to 60% of the image pixels are shadowed according to the binary shadow detection method (compared to approximately 30% for SWIR-sun and VNIR-sun), and the shadows are almost completely contiguous, leading to identification of a few massive shadow regions covering most of the image; see

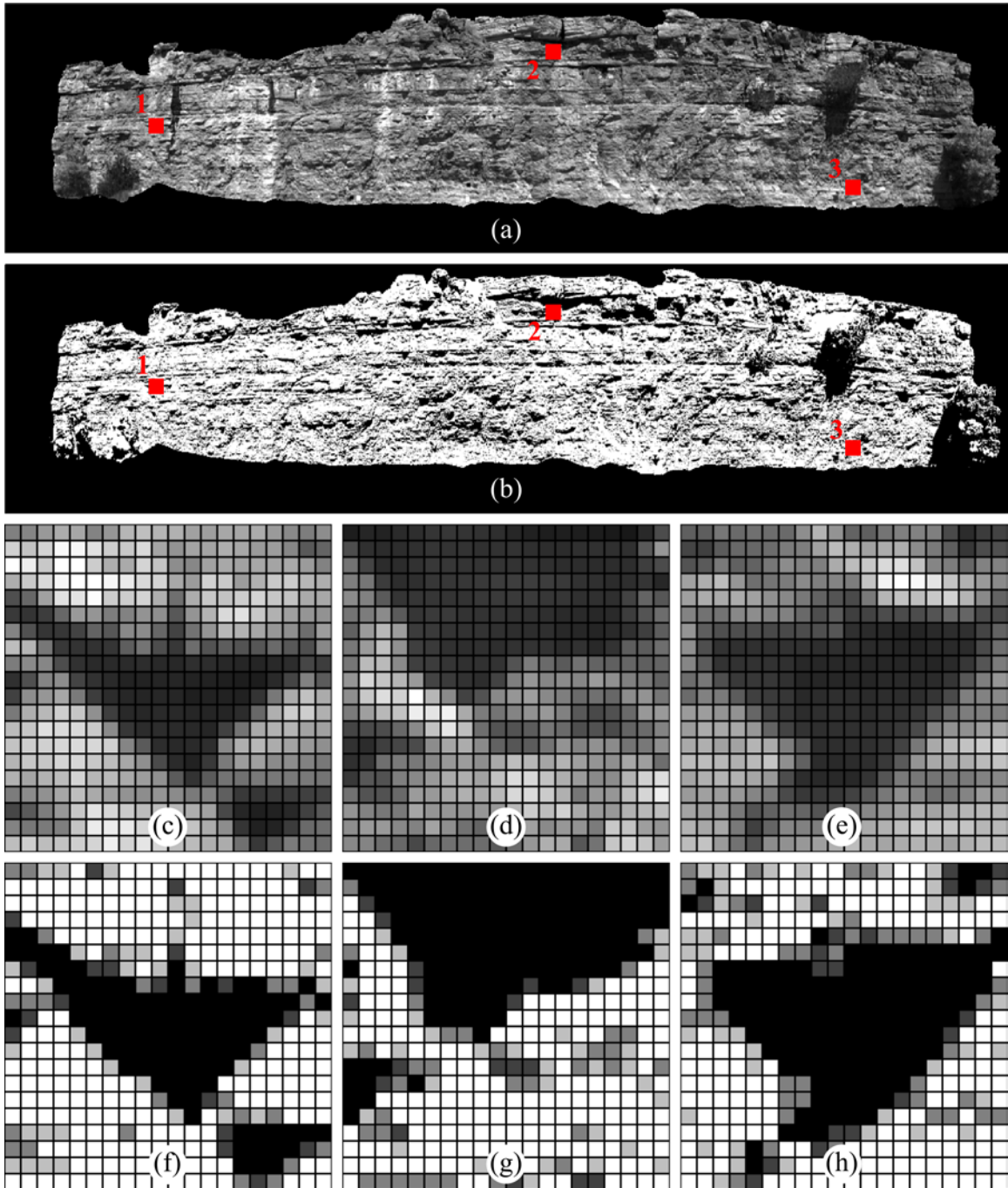


Figure 7.1: (a) SWIR-sun 1549 nm band. (b) Fractional (1/4 increment) shade determination. (c)-(e) Detail locations 1-3 as indicated in (a) and (b). (f)-(h) Matching shadow computation for detail locations 1-3, where the gray value corresponds to the shadow fraction (white = full sun and black = full shade).

Figure 7.2. These massive shadows do not always respond well to shadow restoration algorithms as there are differences in the inwelling spectrum across such large areal extents. The problem is exacerbated for the fractional shadow images, which contain even larger proportions of shadow pixels. Therefore, smaller sub-regions were identified by eroding the massive shadow regions to eliminate narrow connections of only a few pixels width. After the new regions were identified, the original shadow extents were backfilled to recapture the eroded pixels while maintaining pixel assignment to the new regions. A typical shadow “splitting” result is shown in Figure 7.2.

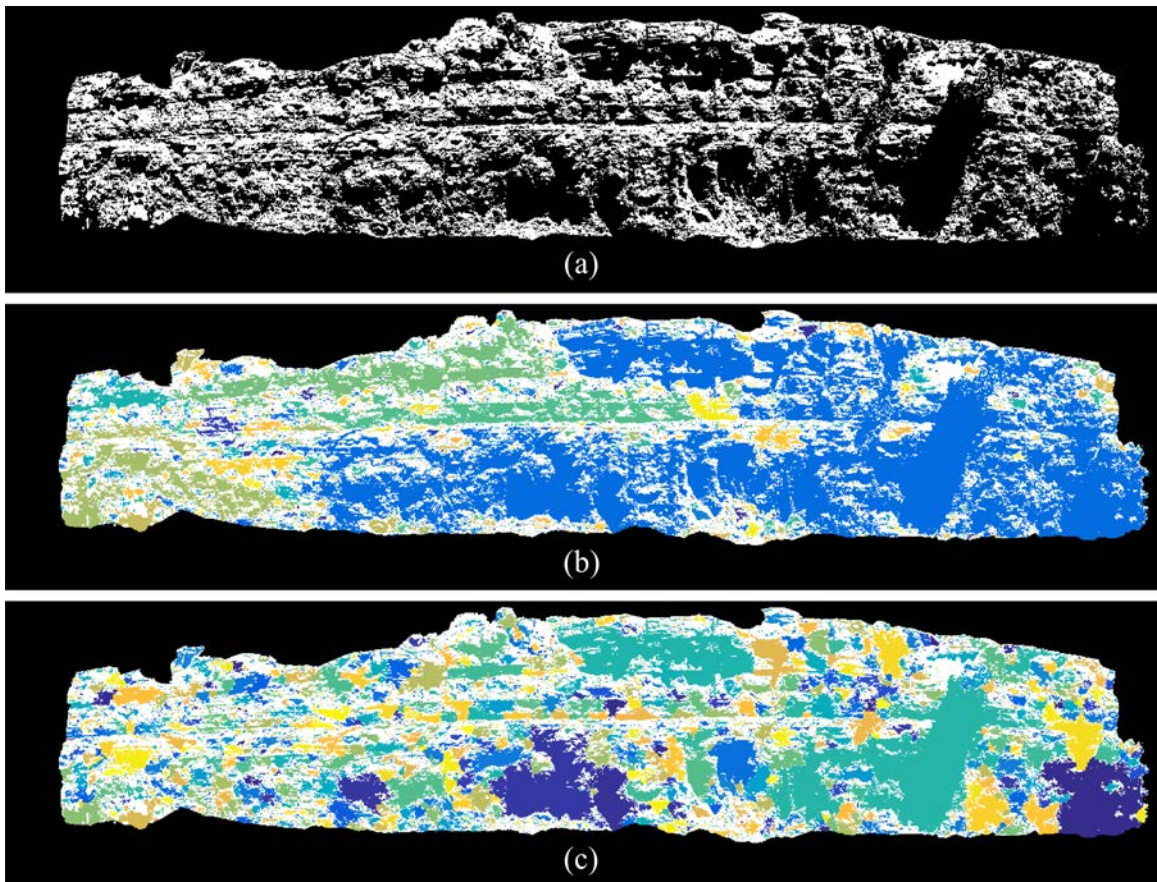


Figure 7.2: (a) SWIR-partial binary shade image. (b) Original shadow regions. (c) Split shadow regions. White indicates sunlit areas.

## 7.2 Shadow Restoration

Before proceeding with the shadow restoration techniques, the metrics used to quantify the restoration improvement are first defined. Several existing shadow restoration methods are then defined and their performance evaluated both with and without the inclusion of active reflectance information in the process. A direct combination of active reflectance information with passive HSI is then proposed and results reviewed. The section concludes with application of several classifiers to a selection of restored images and compared to results from corresponding maximum sun images.

### 7.2.1 Improvement Metrics

Metrics defining spectral shape and scale (magnitude), band correlation with a truth image, and classification consistency were chosen to quantify shadow restoration effectiveness. They are reviewed in the following sub-sections.

#### 7.2.1.1 Spectral Shape and Spectral Scale

Spectral shape is defined as

$$\text{spectral shape} = \frac{\mathbf{p}_1 \cdot \mathbf{p}_2}{\|\mathbf{p}_1\| \|\mathbf{p}_2\|} \quad (7.1)$$

where  $\mathbf{p}_1$  and  $\mathbf{p}_2$  are the pixel spectrum vectors being compared, and as  $\mathbf{p}_1$  approaches  $\mathbf{p}_2$  the metric approaches unity. Spectral shape is simply the cosine of the spectral angle, which is the basis of the SAM classifier that is often applied to imagery with variable illumination. This selection is deliberate, as changes in spectral shape illustrate the challenges in using SAM for identifying targets of common material in sun and shade conditions.

Spectral scale quantifies the mean scalar difference between two pixel spectrums and is defined as

$$\text{spectral scale} = \text{mean} \left( \frac{\mathbf{p}_1}{\mathbf{p}_2} \right), \quad (7.2)$$

where the division of spectrum vector  $\mathbf{p}_1$  by  $\mathbf{p}_2$  is performed wavelength-by-wavelength. As with spectral shape, the metric approaches unity as  $\mathbf{p}_1$  approaches  $\mathbf{p}_2$ . Spectral scale was chosen to measure spectrum magnitude differences in lieu of distance measures, e.g., Euclidean distance, as it captures the approximate scalar influence of shadows on pixel spectra.

In Equations 7.1 and 7.2 above,  $\mathbf{p}_1$  is a sunlit pixel in a partial sun image (e.g., SWIR-partial) and  $\mathbf{p}_2$  is a shaded pixel of similar material existing in the same image. After restoration of  $\mathbf{p}_2$ , the movement of both the spectral shape and scale towards unity indicates improvement in agreement with  $\mathbf{p}_1$ . Although the effectiveness of pixel spectrum restoration could be done by comparing shaded pixels from a partial shade image to sunlit pixels at the same location in the corresponding registered maximum sun image (e.g., SWIR-partial versus SWIR-sun), we chose to compute these metrics within, rather than between, images. This eliminates ambiguity associated with the distinct radiometric calibration applied to each image and any temporal differences in localized sky and topographic scattering characteristics existing between images. The method used to identify pixels of similar material in sun and shade within a single partial shade image is as follows:

1. Shadow pixel locations in the partial shade image to be restored are transferred to the corresponding maximum sun image. Of these locations, those that correspond with a sunlit pixel in the maximum sun image are identified.

2. Sun pixel locations in the partial shade image to be restored are transferred to the corresponding maximum sun image. Of these locations, those that correspond with a sunlit pixel in the maximum sun image are identified.
3. Every pixel combination in the two sets of identified sunlit pixels in the maximum sun image are then compared and those with a spectral shape metric greater than 0.9995 and a spectral scale metric between 0.95 and 1.05 are designated as containing similar materials.

These steps produce pixel pairs with very similar spectral characteristics when exposed to an inwelling sun spectrum. However, each pixel pair also contains one pixel located in the sun and one pixel located in the shade in the corresponding partial shade image, thus enabling shadow restoration effectiveness to be quantified using data from within each partial shade image. To constrain the number of pixel combinations subject to comparison (step 3 above), only pixel pairs falling within a common active reflectance segment (see Section 6.3.2) were compared; vegetation pixels were also excluded to avoid temporal changes between images. Over 1,000 and 5,000 pixel pairs were identified in the SWIR and VNIR images, respectively.

The distributions of the spectral shape and spectral scale metrics in the subsequent analyses are presented in the form of boxplots indicating the median, a median notch that approximates a 5% significance level for differences between medians (McGill et al., 1978), the interquartile range (IQR), and whiskers extending outward from each side of the IQR box by a length of  $1.5 \times \text{IQR}$ . The boxplot representation enables efficient comparison between multiple results (compared to overlapping histograms) and uses median and IQR metrics that

are appropriate for the predominantly skewed distributions. For a cleaner display, data points beyond the whiskers (sometimes referred to as outliers) are not shown on the boxplots.

#### 7.2.1.2 Band Correlation

Band correlation quantifies the similarity between two HSI bands and is defined as

$$\text{band correlation} = \frac{\text{cov}(\mathbf{b}_1, \mathbf{b}_2)}{\sigma_{\mathbf{b}_1} \sigma_{\mathbf{b}_2}}, \quad (7.3)$$

where  $\mathbf{b}_1$  is a vector of all pixel brightness values in a single band in one of the adjusted full shade images and  $\mathbf{b}_2$  is the corresponding vector of band values from an original or restored partial shade image. The adjusted full shade images (see Section 5.2) are used for comparison given their very uniform appearance due to the absence of solar shadowing. The application of the band correlation metric to partial shade bands before and after shadow restoration quantifies the “eye-test” naturally applied to a corrected band, i.e., random speckle or poorly corrected shadow regions that are easily identified visually will produce lower correlation values. To ease interpretation, a mean band correlation computed from the collection of all image band correlation values is used.

#### 7.2.1.3 Classification Consistency

The final metric is comparison of classified pre- and post-restoration partial shade HSI to that of the maximum sun HSI using SAM, MD and ML classifiers. Whereas the spectral shape, spectral scale and band correlation metrics are presented within the analysis of each restoration method, a limited number of image classification results are presented together in Section 7.2.4. In particular, the relative absence of change in classification between sunlit pixels in a maximum sun image and their corresponding restored shade pixels in a partial shade image is examined.

## 7.2.2 Existing Restoration Methods

### 7.2.2.1 Pixel-Based Restoration

As reviewed in Chapter 1, a number of shadow restoration methods that solve for the inwelling shadow spectrum require identification of common material pixels in the sun and shade. This is difficult to automate in practice, and current literature resorts to manual pixel selection. We investigate whether the TLS-derived active reflectance information, which is highly resistant to solar shadowing, can assist in identifying sun and shade pixels of similar material at a level sufficient for effective shadow restoration.

For testing purposes, we simplify the pixel-level methods found in the literature, e.g., Friman et al. (2011) and Zhang et al. (2013), to exclude fractional sky-view computations and the ratio of direct to diffuse sky irradiance and simply compute the inwelling shadow irradiance spectrum in order to estimate the reflectance of the shadowed pixels. Given a pixel in the sun and a pixel in the shade that refer to a common material, coupled with the fact that the reflectance property of a material is invariant to whether it exists in sun or shade, we can write

$$\rho = \frac{\pi L_{sun}}{E_{sun}} = \frac{\pi L_{shade}}{E_{shade}}, \quad (7.4)$$

where  $\rho$  is reflectance,  $L$  is the radiance measured by the camera and  $E$  is irradiance on the outcrop surface, with each quantity being wavelength specific. Note that although reflectance is available from sunlit pixels in the radiometrically calibrated HSI, the cameras used in this dissertation do not report the measured radiance in physical units of  $W \cdot m^{-2} \cdot sr^{-1}$ ; rather, the information is in dimensionless DN values. However, since the DNs are proportional to

the measured radiance, we can rearrange the first and third terms of Equation 7.4 to produce an expression that is at least proportional to  $E_{shade}$ ,

$$E_{shade} = \frac{\pi L_{shade}}{\rho} \propto \frac{DN_{L,shade}}{\rho} = DN_{E,shade}. \quad (7.5)$$

where  $DN_{E,shade}$  is a dimensionless scalar that is proportional to the proper  $E_{shade}$  term (note that  $\pi$  is implicitly absorbed by  $DN_{E,shade}$ ). With a method for obtaining  $DN_{E,shade}$  and observations of  $DN_{L,shade}$  in adjacent pixels in the shadow region of interest, we can solve for  $\rho$  in the adjacent shaded pixels as

$$\rho_{adjacent\ shade} = \frac{DN_{L,adjacent\ shade}}{DN_{E,shade}}, \quad (7.6)$$

thus restoring the shadowed area to reflectance.

Using the binary shadow determination information, matching pixels in the SWIR-partial HSI were selected for each distinct shadow area by comparing every shade pixel with every sun pixel, with the combinations constrained to exist within a common active reflectance segment in order to limit the number of combinations and enforce reasonable spatial proximity. The sun/shade pixel set with the closest lidar active reflectance values was then selected. This produced random restoration results with restored shadow areas appearing darker, brighter, or approximately correct compared to immediately adjacent sunlit areas; original and restored bands from the SWIR-partial HSI are shown in Figure 7.3. Similar results were obtained when using one or both of the 532 and 1550 nm active reflectance bands. The poor results are not surprising, as this method is attempting pixel-level unsupervised classification of material with very limited spectral information.

Under the assumption that shadowed spectra can be roughly approximated as a scaled version of sunlit spectra for the same material, the spectral shape between each pixel set was

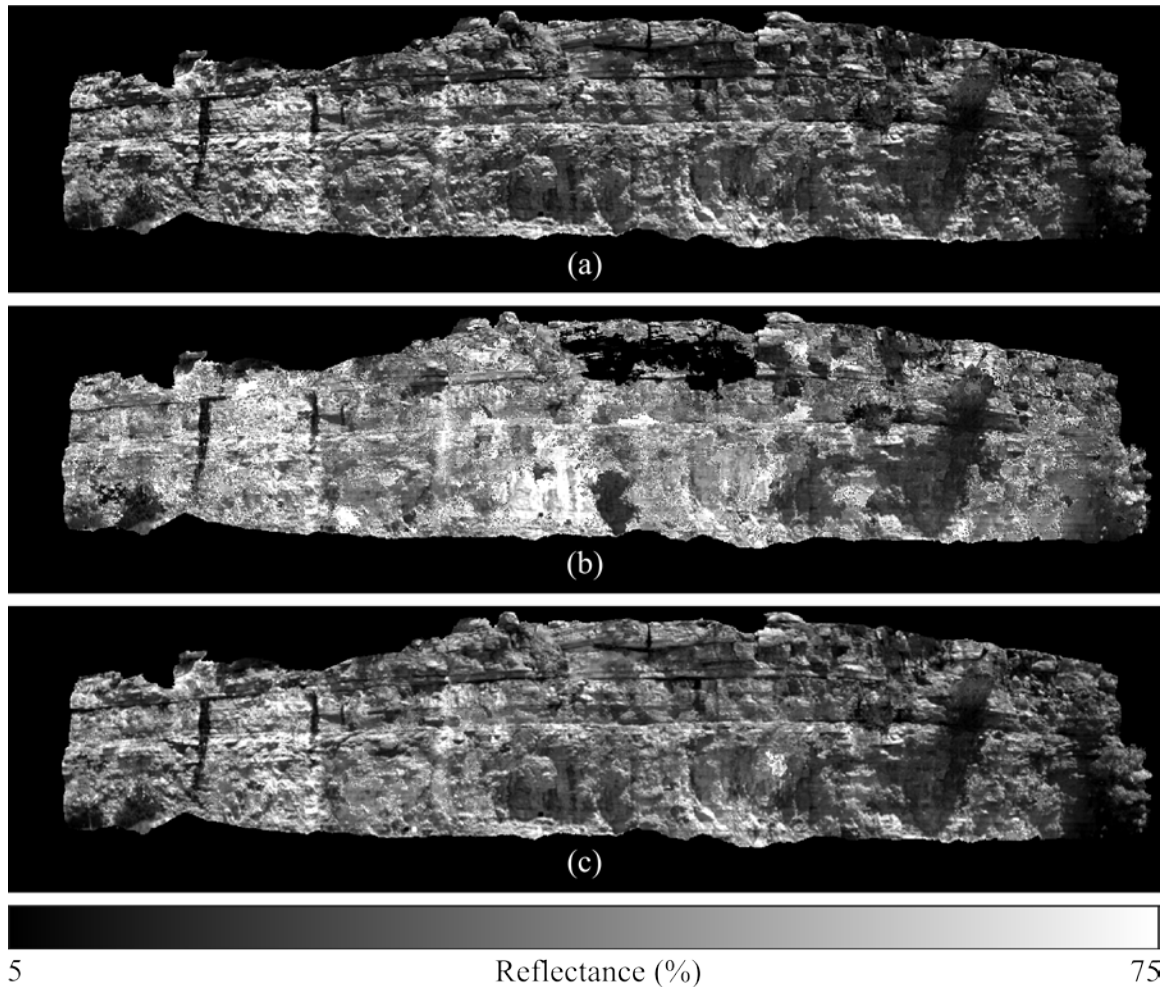


Figure 7.3: (a) Original SWIR-partial 1549 nm band. (b) Shadows corrected via matching pixels selected using the 532 nm and 1550 nm active reflectance information. (c) Shadows corrected via matching pixels selected using active reflectance information and the spectral shape metric.

computed and the shortest distance in the space spanned by the spectral shape and active reflectance difference used to select matching pixels for each shadow area. This reduced the random nature of the restoration errors, but the errors are biased on the dark side (part (c) of Figure 7.3). The reason for the bias is not clear, but may result from the fact that shadow spectra are not a simple scaled version of sun spectra, thus introducing a systematic error when using spectral shape as a material identification metric between the sun and shade.

The following additional avenues were explored to improve the results:

1. The 1550 and 532 nm active reflectance images were employed individually and in combination when creating the segmented active reflectance image used to constrain the sun and shade pixel pair comparisons.
2. A number of different spatial and spectral bandwidth parameters were tested when creating the segmented active reflectance image with the mean shift algorithm.
3. Different weights were assigned to spectral shape versus active reflectance when computing the shortest distance spanned by the two metrics.
4. The shadow and sun regions were eroded in order to eliminate partially shaded pixels along the shadow boundaries from the matching algorithm.

However, none of these efforts yielded significant improvement. Given the poor results, we discard this method and do not compute the metrics quantifying the marginal shadow improvement. Rather, we turn our focus to statistical shadow restoration methods that use regions of similar material pixels in the sun and shade.

#### 7.2.2.2 Region-Based Restoration

We begin by reviewing the mean scale and linear correlation correction methods for shadow restoration. Methods for selecting the regions of similar material in the sun and shade, both with and without active reflectance information, are then detailed. This enables the value of including active reflectance information in the restoration algorithms to be evaluated.

##### 7.2.2.2.1 *Methods*

#### **Mean Scale Correction**

The concept of finding matching sun and shade pixels to compute the inwelling shadow spectrum presented in the prior section can be generalized in two ways. First, rather than

limiting the matching material identification to individual sun and shade pixels, regions of similar materials within the sun and shade can be identified, thereby reducing the impact of random errors on the selection process. Second, the difference between sunlit and shadowed areas of a region of common material can be approximated by a simple scale factor (Fredembach and Finlayson, 2006). For a single HSI band, the mean scale correction is given as

$$DN_{restored\ shade} = DN_{shade} \left( \frac{\mu_{sun\ region}}{\mu_{shade\ region}} \right), \quad (7.7)$$

where  $\mu_{sun\ region}$  and  $\mu_{shade\ region}$  are mean values computed from sun and shade regions of similar material and  $DN_{shade}$  is an original pixel brightness value in the shaded area being corrected. Note that Equation 7.7 can be applied to images with pixel values in DN or in reflectance, with reflectance used in this dissertation. Since pixels with fractional shadow assignments are easily incorporated, both the binary and 1/4 fractional shade detection products were tested with this method.

### **Linear Correlation Correction**

As reviewed in Chapter 1, numerous statistical shadow restoration methods beyond a simple scalar factor exist in the remote sensing literature. We examine the linear correlation correction method, also referred to as the mean and variance transform, based on several studies that report its performance to be favorable in comparison to other standard methods such as histogram matching and gamma correction techniques (Sarabandi et al., 2004; Dare 2005; Zhou et al., 2009). The linear correlation correction for restoring shadowed pixel brightness within a single HSI band is given as

$$DN_{restored\ shade} = \frac{\sigma_{sun\ region}}{\sigma_{shade\ region}} (DN_{shade} - \mu_{shade\ region}) + \mu_{sun\ region} \quad (7.8)$$

where  $\sigma$  is the standard deviation of a sun or shade region and all other terms are as defined for Equation 7.7. As with the mean scale correction, the linear correlation correction can be applied to images in units of DN or reflectance, with the current analysis limited to reflectance.

#### 7.2.2.2.2 *Similar Material Region Selection*

In order to evaluate the value of active reflectance information in the restoration methods, the required regions of similar material existing in the sun and shade are identified using either the segmented active reflectance information or spatial proximity only. When using the segmented active reflectance information, the matching sun and shade regions are selected (and the shadow restoration algorithms applied) in the following two ways:

1. The union of all segments intersecting a shadow area, where the matching sun and shade regions are created from the combination of multiple contiguous active reflectance segments that intersect the shadow area of interest.
2. Segment by segment, where the matching sun and shade regions are restricted to exist within a common segment.

These selection methods are illustrated in parts (a) and (b) of Figure 7.4, where the red box indicates the shadow area, the rectangles represent active reflectance segments, the solid fill indicates the selected portion of the shadow region and the diagonal hatching indicates the selected sun region. Note that segmented 532 nm active reflectance is used for region selection in the VNIR HSI and segmented 1550 nm active reflectance for the SWIR HSI.

For comparison, the following two spatial-only region selection methods are used:

1. A buffer of pixels along the far edge of the cast shadow as in Li et al. (2005), pushing both into the sunlit and shadowed areas, are used to define the matching regions.
2. The complete shadow area and a buffer of sunlit pixels around the entire boundary of the shadow area are used to define the matching regions.

These methods are illustrated in parts (c) and (d) of Figure 7.4.

Prior to evaluating the relative performance of the different region selection and shadow restoration methods, it is necessary to optimize (approximately) the parameters used to select similar regions. For the active reflectance based methods, this consists of varying the spatial and spectral ranges in the mean shift algorithm used to create the segmented images. Spatial pixel distances of 10, 20, 30 and 40 and spectral brightness distances (8-bit imagery) of 1, 2 and 3 were used. For the purely spatial methods, the number of buffered pixels was varied with values of 2, 4, 8 and 16 used. Each of the three region based shadow restoration algorithms (mean scale with binary shadows, mean scale with 1/4 fractional shadows and linear correlation correction) were run using the matching sun and shade regions generated from variable parameter sets defined above. In almost every case the parameters producing the best spectral shape, spectral scale or mean band correlation were not the same for a given restoration method. For the analysis in this dissertation, the parameters producing the best

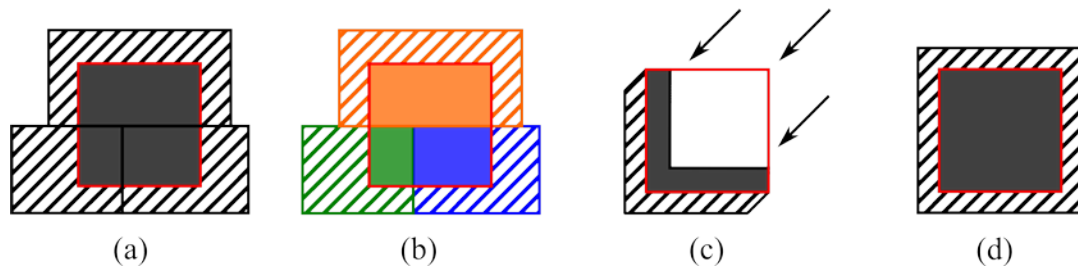


Figure 7.4: Region selection methods: (a) union of active reflectance segments, (b) active reflectance segments, segment by segment, (c) cast shadow far edge buffer (arrows indicate solar ray direction) and (d) shadow boundary buffer.

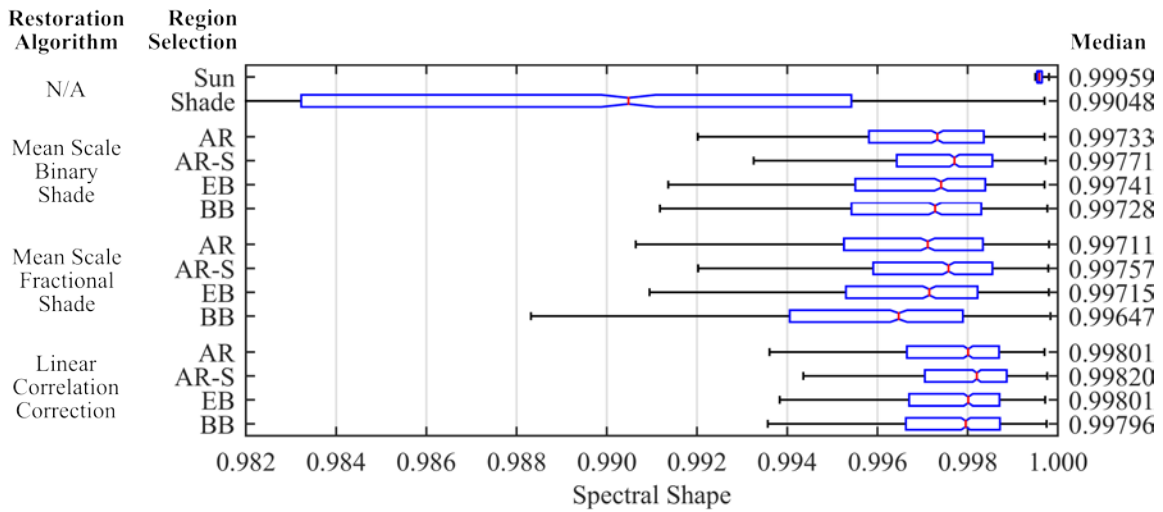
spectral shape metrics were selected since a small difference in spectrum shape is often more relevant to a material difference than a small difference in spectrum magnitude, particularly when employing a SAM classifier.

#### 7.2.2.2.3 *Results*

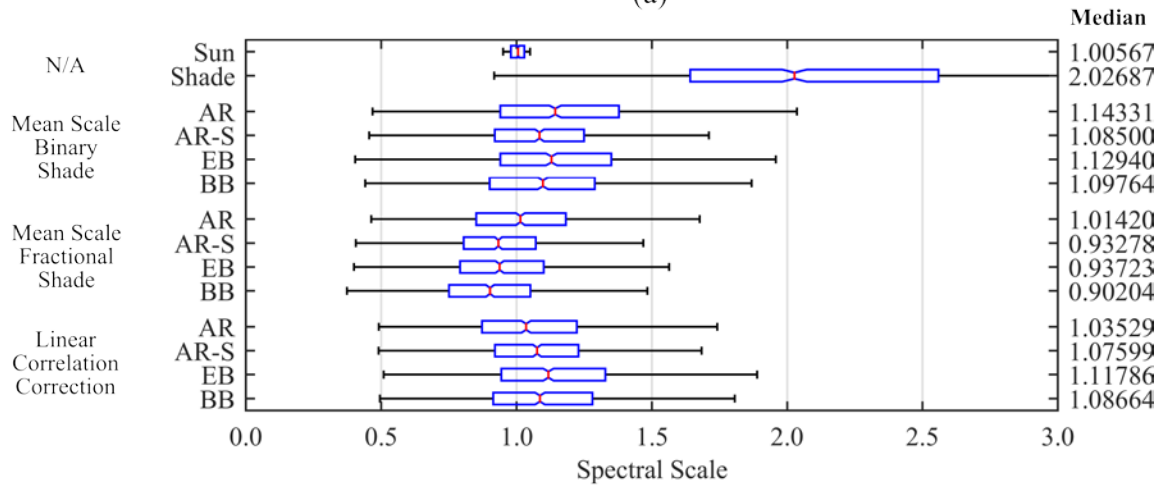
The spectral shape, spectral scale and mean band correlation results for the original and restored SWIR-partial HSI are summarized in Figure 7.5. The metrics computed from the maximum sun and unrestored partial shade images are shown at the top of each graph for reference. In general, all the restoration methods and region selection techniques successfully improved the shadowed pixel spectra, with the linear correlation correction method producing the best results. The mean improvement for all restoration methods in median and IQR (defined by the percentage by which the restored median and IQR values move toward the reference (sun) median and IQR values) is 77% and 80% for the spectral shape metric, and 92% and 66% for the spectral scale metric.

We examine spectral shape first, recalling that the region selection parameters were optimized for this metric. The use of active reflectance for region selection has a small positive influence on spectral shape restoration for all three restoration methods, but only when applying the active reflectance information in a segment by segment manner. However, using the active reflectance in a segment by segment fashion produces spatial discontinuities in the form of jigsaw patterns following the segment boundaries when applying the mean scale method (compare parts (b) and (c) in Figure 7.6) and mottling when applying the linear correlation correction method (compare parts (d) and (e) in Figure 7.6).

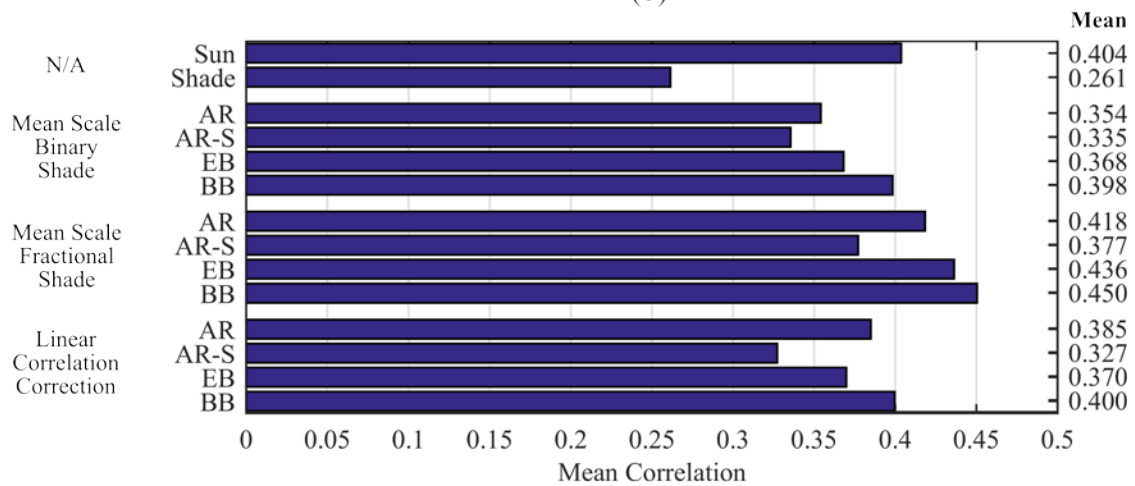
The spectral scale results do not exhibit a trend between region selection methods. With respect to restoration methods, the only visible trend is the slightly lower values generated



(a)



(b)



(c)

Figure 7.5: SWIR-partial HSI shadow restoration metrics. AR=Active Reflectance, AR-S=Active Reflectance-Segment by segment, EB=Edge Buffer, BB=Boundary Buffer.

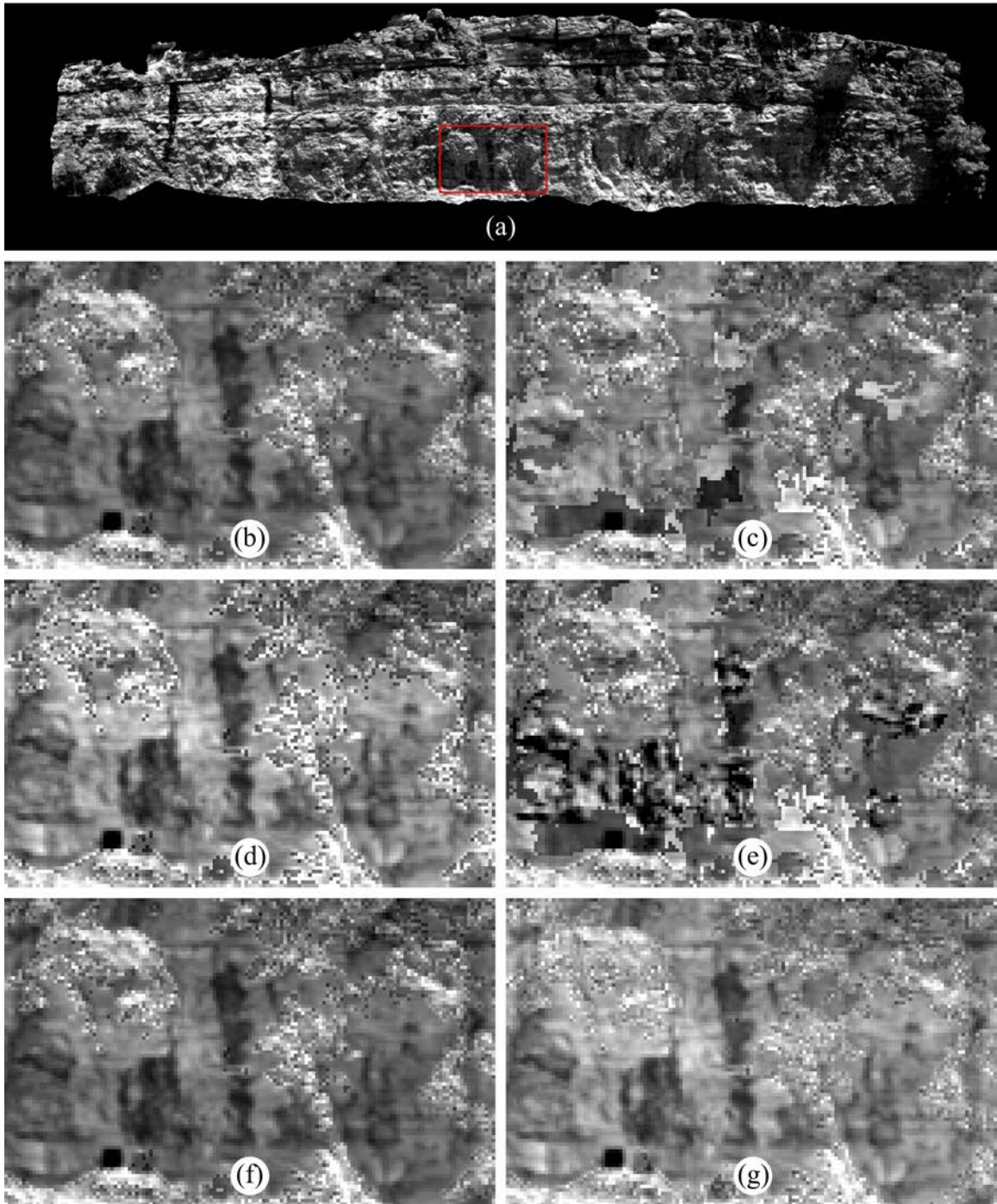


Figure 7.6: (a) Detail location. Shadow restoration: (b) mean scale, (c) mean scale, segment by segment, (d) linear correlation correction, (e) linear correlation correction, segment by segment, (f) mean scale with binary shade and (g) mean scale with fractional shade.

by the fractional shade mean scale method. This systematic difference is due to the use of fractional, rather than binary, shade values, which alters both the computation and application of the mean scale factor.

For mean band correlation, use of active reflectance information for region selection has an overall negative influence on the restoration methods, with the exception of the linear correlation correction method. In particular, the application of the restoration methods in a segment by segment fashion based on active reflectance information is always the lowest. This is due to the jigsaw and mottling artifacts previously discussed. Note that the mean scale restoration method using fractional shade values produces the highest band correlation values for all region selection methods. This is a result of the slightly “smoother” band images that are produced in comparison to the methods using the binary shadow computation. This is illustrated in parts (f) and (g) of Figure 7.6. The smoothness reflects an improvement in the amount of correction applied to each pixel in a spatial sense, and is an indirect validation of the shadow detection accuracy at the sub-pixel, i.e., fractional, level.

As noted in Section 7.1, fractional shadow images produced by testing 4, 9, 12 and 16 evenly spaced points per pixel were created. Figure 7.7 shows the mean band correlation and median of the spectral shape metric, both as a function of shadow fraction resolution, for each region selection method using the mean scale restoration algorithm. The same region selection parameters used to generate the data plotted in Figure 7.5 were used here. Although the mean band correlation continues to increase with finer shadow fractions, the majority of improvement is achieved with the 1/4 shadow fraction product. Recalling that the SWIR camera pixel size on the outcrop is 55 mm at the nearest camera/outcrop range, the results suggest the point cloud registration and georeferencing, HSI image fusion, and surface mesh

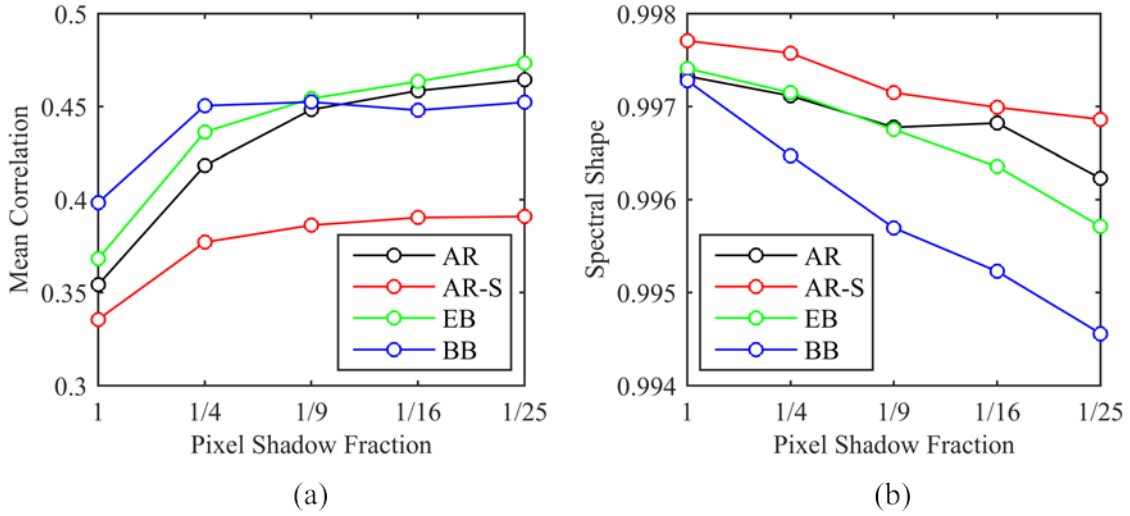
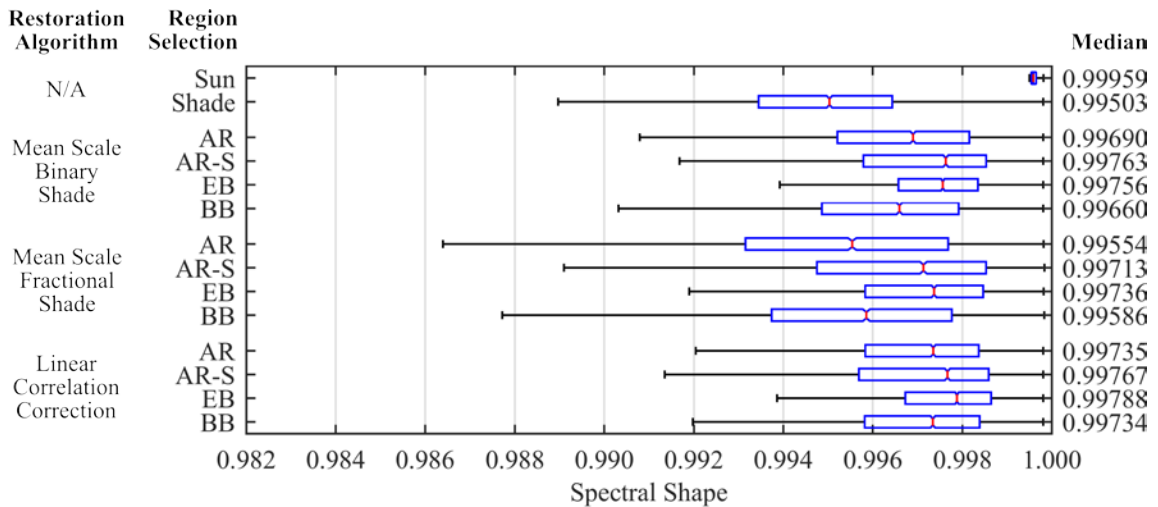


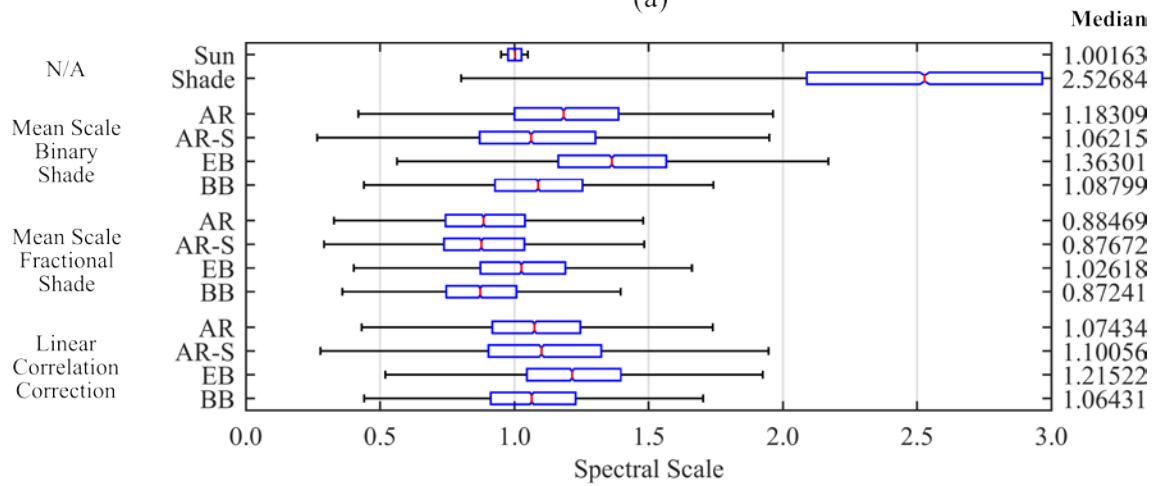
Figure 7.7: Mean correlation (a) and spectral shape median (b) with respect to pixel shadow fraction computation for the SWIR HSI.

product are sufficient for shadow detection at a surface resolution of 2-3 cm. The spectral shape metric, however, exhibits a continued downward trend with increasing shadow fraction resolution; see Figure 7.7(b). This motivates the use of the 1/4 shadow fraction products in the analysis herein in order to obtain the majority of mean correlation improvement while minimizing the spectral shape degradation. The results are very similar for the VNIR and are not shown.

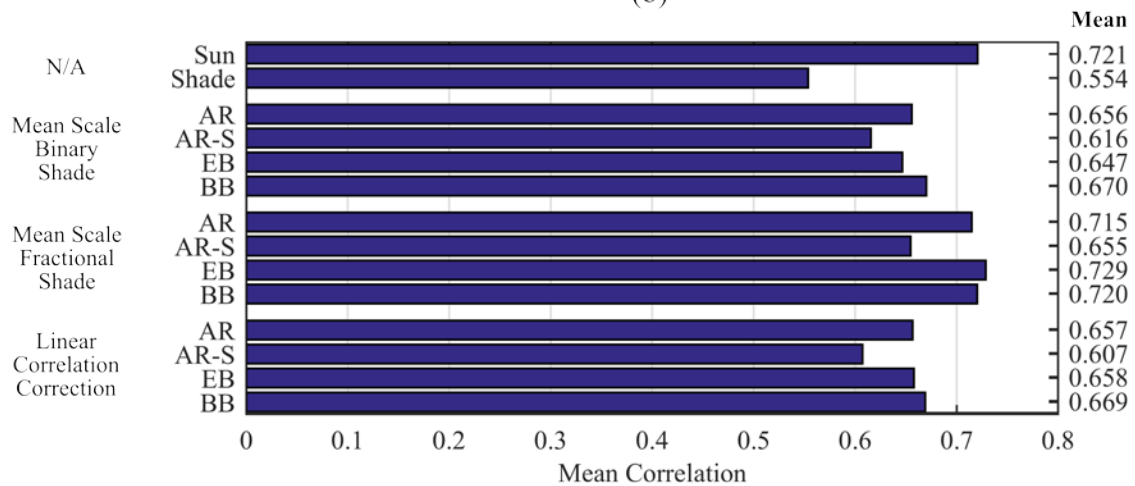
The VNIR restoration results are summarized in Figure 7.8. The mean restoration improvement for all methods is 45% and 2% for the spectral shape median and IQR, and 92% and 64% for the spectral scale median and IQR. Note that the overall improvement in restored spectral shape is much weaker than for the SWIR. To some extent this is due to the much smaller differences in spectral shape between the sun and shade compared to the SWIR (compare part (a) in Figures 7.5 and 7.8), leaving less room for improvement. There is also no clear evidence that using active reflectance information is beneficial compared to purely spatial methods for region selection in the restoration algorithms; for spectral shape and



(a)



(b)



(c)

Figure 7.8: VNIR-partial HSI shadow restoration metrics. AR=Active Reflectance, AR-S=Active Reflectance-Segment by segment, EB=Edge Buffer, BB=Boundary Buffer.

mean band correlation, the active reflectance region selection methods are always surpassed by one of the purely spatial methods. The reason for the inability of active reflectance information to improve region selection in the VNIR HSI versus some limited success in the SWIR HSI may be due in part to the smaller amount of spectral variation in the rock outcrop at the 532 nm lidar laser wavelength (active and passive reflectance  $1\sigma$  values of 5.9% and 9.7%) versus the 1550 nm laser wavelength (active and passive reflectance  $1\sigma$  values of 7.2% and 15.7%). With less brightness variation, the segmented 532 nm active reflectance information may be unable to discriminate material differences as well as the 1550 nm active reflectance.

#### 7.2.2.3 Summary Conclusions

Improvement in the spectral shape and scale characteristics of shadowed pixel spectra in comparison to sunlit pixels of similar material was successfully demonstrated for terrestrial VNIR and SWIR HSI. The influence of active reflectance information on determining regions of similar materials is marginal. Algorithms employing regions (rather than pixels) of similar material showed improved spectral shape restoration in the SWIR HSI when using regions defined by active reflectance and applied in a segment by segment fashion compared to purely spatial region selection methods. However, this improvement was not realized when restoring VNIR shadows, potentially due to the reduced amount of spectral variation in the rock outcrop at 532 nm versus 1550 nm, and also comes at the cost of reduced band correlation in the restored SWIR HSI.

## 7.2.3 Proposed Direct Scale Method

### 7.2.3.1 Single Wavelength

Rather than incorporating the active reflectance information into existing shadow restoration techniques where it is used indirectly to assist in identifying similar material regions in the sun and shade, the active reflectance can be used to directly adjust the passive pixel spectra. The direct adjustment is a simple scale factor derived from the ratio of the active to passive reflectance measures at the active reflectance wavelength (i.e., the TLS laser wavelength) which is then applied to the entire passive spectrum of the subject pixel. This is illustrated in Figure 7.9, where sample original and directly scaled pixel spectra from a single pixel location are shown and compared to the spectrum of a sunlit pixel of similar material. Note that the direct adjustment is applied to all pixels in the HSI, both those in the shade and in the sun.

Since the direct scale factor is applied uniformly to the pixel spectrum, there is no change

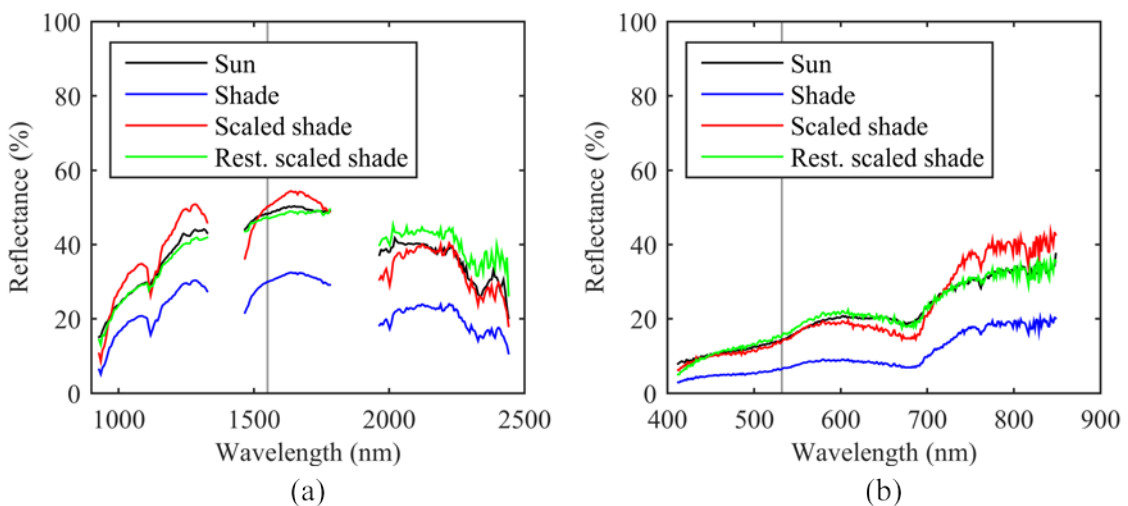


Figure 7.9: Sample comparison of (a) SWIR and (b) VNIR passive and direct scaled pixel spectra. The vertical lines indicate the TLS laser wavelengths.

to spectrum shape and thus no improvement in the spectral shape metric. However, there is distinct improvement in spectrum scale, beyond that able to be achieved by the indirect restoration methods previously examined. These two observations are illustrated in parts (a) through (d) in Figures 7.10 (SWIR) and 7.11 (VNIR), where the spectral shape and spectral scale metrics for the matched pixel pairs are presented in the form of overlapping histograms, rather than boxplots, to better illustrate the changes. The spectral scale histogram IQR widths for the directly scaled HSI are reduced by 39% and 32% over their restored passive counterparts for the SWIR and VNIR matched pixel pairs, respectively. In addition to an improvement in spectral scale over indirect methods, band correlation is dramatically improved in the SWIR, from approximately 0.4 to 0.6 (a 45% improvement), resulting from the removal of uncompensated topographic induced solar irradiance differences and the error associated with imperfect pixel shadow determination; see Figure 7.12(a). This is not the case for the VNIR, however, where the direct scale adjustment has a lower band correlation compared to indirectly corrected images and even compared to the original uncorrected image at the wavelength extremities of the HSI. See Figure 7.12(b). There are a few potential reasons for this. First, the full shade HSI that is used as the benchmark in correlation computation contains “shadows” in areas with very low sky-view fractions, such as in crevasses and directly underneath ledges. Due to the differences in inwelling spectra, the scaled VNIR HSI is overly brightened in these areas at wavelengths distant from the 532 nm scaling location, thus reducing the correlation. Second, the active reflectance band captures a slightly different image of the outcrop than the corresponding passive HSI 532 nm band due to hotspot differences as discussed in Chapter 2.

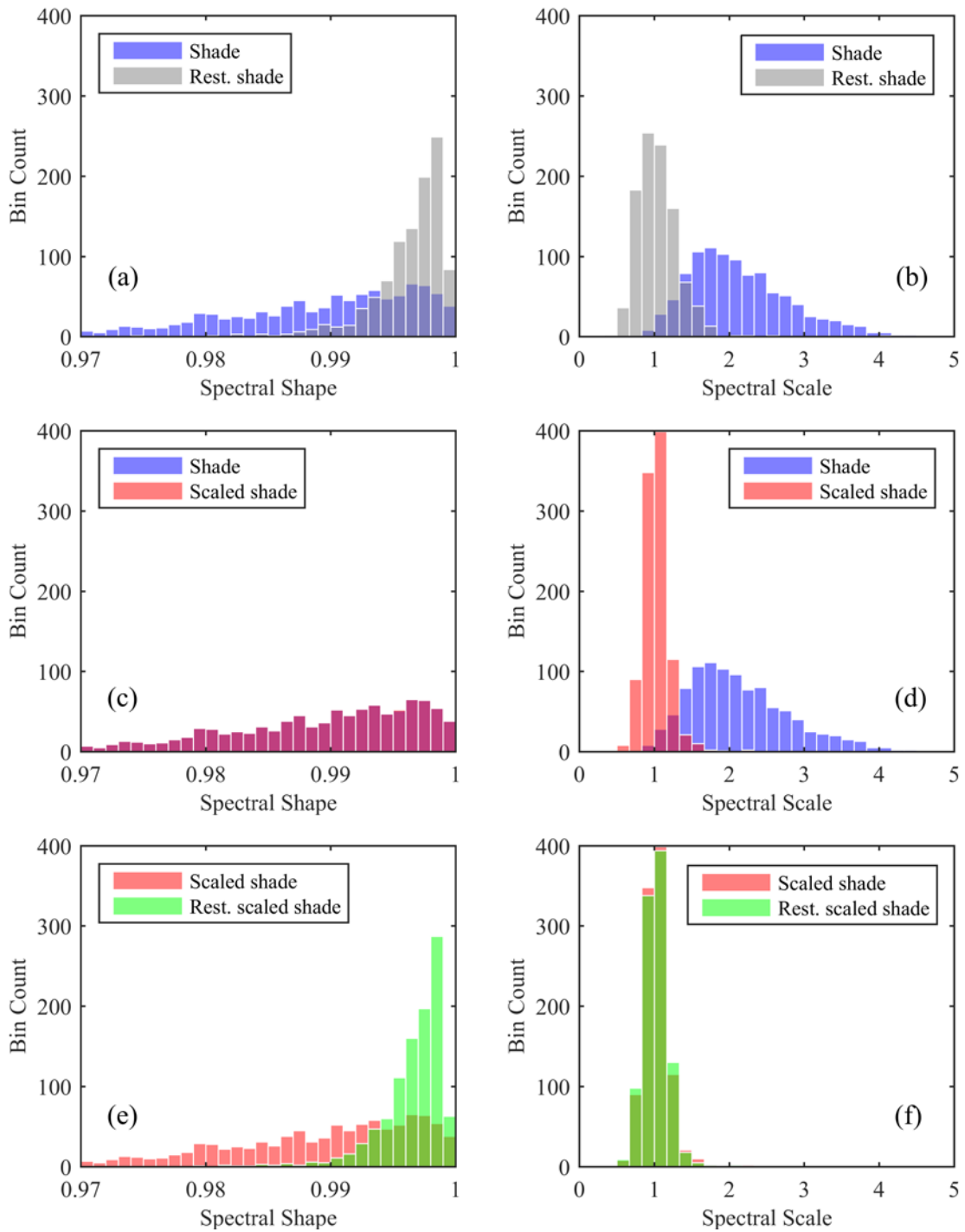


Figure 7.10: Spectral shape and spectral scale metrics illustrating the influence of indirect, direct and combined direct and indirect shadow restoration methods for the SWIR HSI.

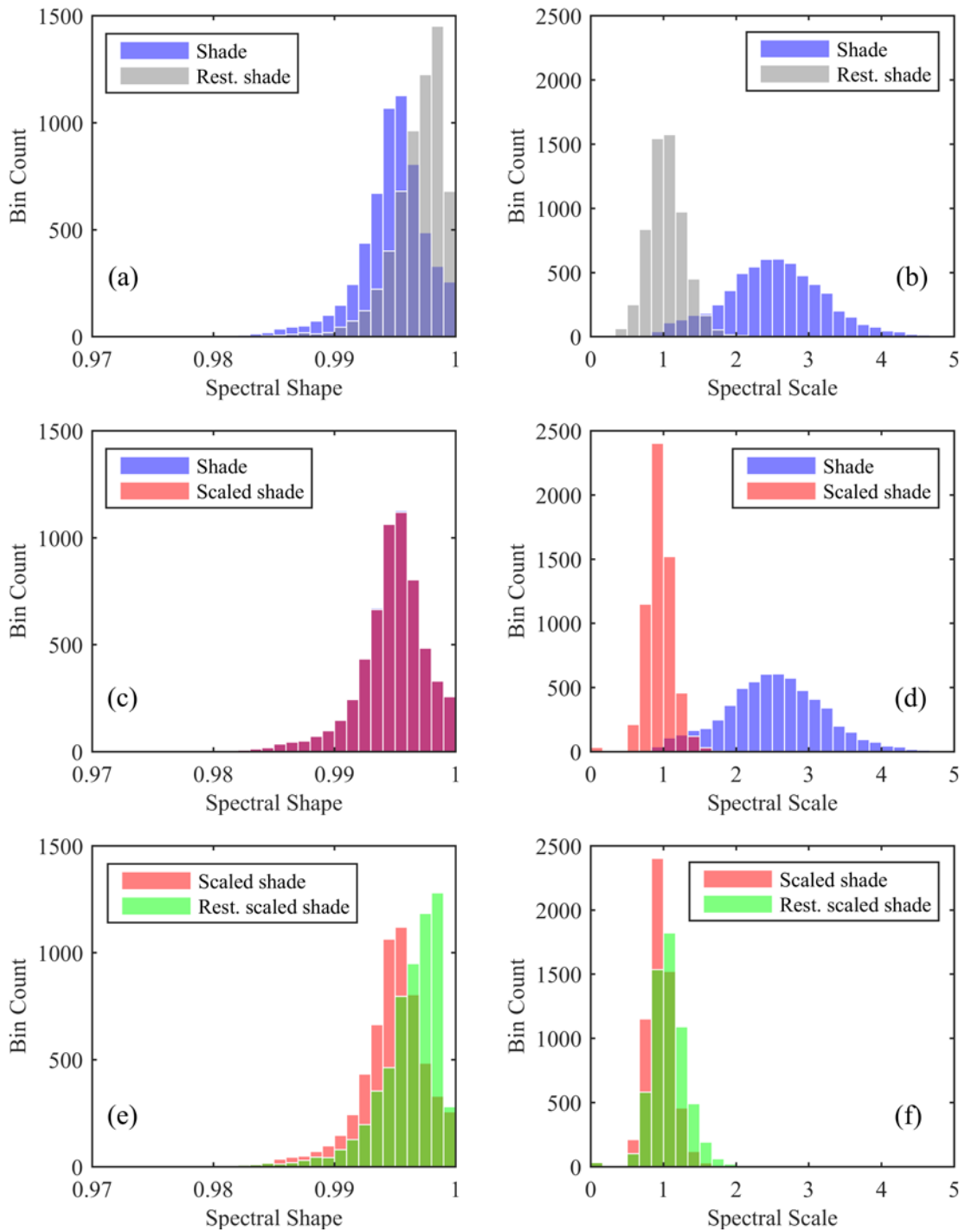


Figure 7.11: Spectral shape and spectral scale metrics illustrating the influence of indirect, direct and combined direct and indirect shadow restoration methods for the VNIR HSI.

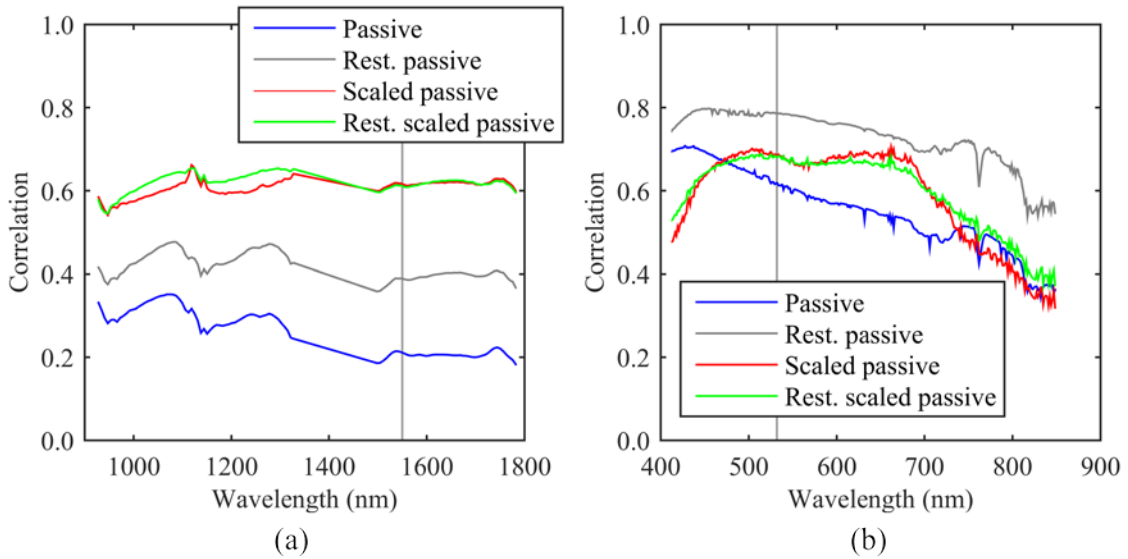


Figure 7.12: (a) Band correlation of passive, restored passive, scaled and restored scaled SWIR-partial HSI. (b) Same as (a), but for the VNIR-partial HSI. The vertical gray lines indicate the TLS laser wavelengths.

The computed scale factors are most applicable at or very near the scaling wavelength, with large differences between the scaled and sunlit spectra occurring further from the scaling wavelength (see Figure 7.9). This motivates the application of one of the indirect region based restoration methods on top of a directly scaled HSI, thereby improving both spectrum magnitude and shape. This is illustrated in Figure 7.9 and in parts (e) and (f) of Figures 7.10 and 7.11. Note that the improvement in spectral shape is slightly less than achieved with purely indirect restoration methods, and the improvement in spectral scale is slightly less than with the purely direct scale application. The application of dual correction techniques also improves the band correlation of the directly scaled SWIR HSI in a few areas (Figure 7.12) whereas the VNIR correlation shows mixed results.

Finally, it is noted that directly scaling an HSI with active reflectance changes the optimal region selection parameters from those previously determined for the indirect region based restoration methods. For the data graphed in Figures 7.10, 7.11 and 7.12, indirect

restoration methods and parameters were qualitatively selected from the previously determined optimal set such that they also worked well for the dual correction technique. For the SWIR, the fractional shade mean scale method using segmented active reflectance (spatial bandwidth = 20 pixels, brightness bandwidth = 1) to select matching regions was chosen; for the VNIR, the fractional shade mean scale method with matching regions determined from a 2 pixel cast shadow edge buffer was used.

### 7.2.3.2 Multiple Wavelengths

Although the combination of a direct scale factor and indirect restoration methods combines positive aspects of both techniques, the indirect restoration methods are computationally heavy, requiring detection and restoration of each distinct shadow area. However, if multiple active reflectance wavelengths were available within the spectrum of a single HSI, an interpolated direct scale factor could be applied between the active reflectance wavelengths, thus easing computational loads while potentially restoring spectrum shape. A multiple wavelength direct adjustment was simulated using wavelengths selected according to those available in commercially available lidar systems and falling within the spectrum of each HSI camera; see Table 7.1. The shade spectrum for each matched shade/sun pixel pair used in the prior indirect restoration analyses was then iteratively scaled using a successively greater number of scaling wavelengths. The simulated scale factor was computed from the ratio of the sun to shade spectrum values at the selected wavelength. For spectrum locations between scaling wavelengths, the scale factors were linearly interpolated. The median and median notch values of the spectral shape and spectral scale metrics as a function of the number of scaling wavelengths are plotted in Figure 7.13, where we see improvements in both spectral shape and spectral scale.

Table 7.1: Common HSI and TLS laser wavelengths

<b>TLS Make &amp; Model</b>	<b>Laser Wavelength (nm)</b>
<i>VNIR Camera: 400-1000 nm</i>	
Leica HDS3000	532*
Callidus CPW 8000	658*
Trimble FX	690
ZF 5003i	785*
Trimble VX	870†
Leica HDS4400	905†
<i>SWIR Camera: 970-2500 nm</i>	
Riegl VZ-6000	1064*
Riegl VZ-400	1550*
N/A (Holmium doped fiber laser)	2050*‡

\*Used for multiple wavelength direct adjustment simulation

†Outside usable range in current HSI dataset

‡Not currently available, but potentially viable per Pfennigbauer and Ullrich (2011)

Figure 7.14 shows sample scaled shade spectra from the SWIR and VNIR matched sun/shade pixel pairs (the same spectra are shown in Figure 7.9) for one, two and three wavelength scale locations. Note that even with multiple wavelength scaling locations, the scaled shade spectra still differ from the sun spectrum shape. If we discard the physical premise that the influence of shade on material spectra is roughly scalar and employ a spectrum shift (i.e., a translation) computed at the selected wavelength locations instead, the agreement in shape appears to be improved (Figure 7.14). Results from applying a shift adjustment to the entire set of matched sun/shade pixel pairs are shown in Figure 7.13 where we see an improvement for the SWIR, but not for the VNIR. The lack of improvement in the VNIR is due to the relatively flat pixel spectra in the VNIR HSI, which are better suited to a scale factor when there are no direct wavelength locations at the spectrum extremes (see Figure 7.14). Note that the simulation does not consider the errors that would normally exist if the scale or shift values were derived from actual active reflectance information.

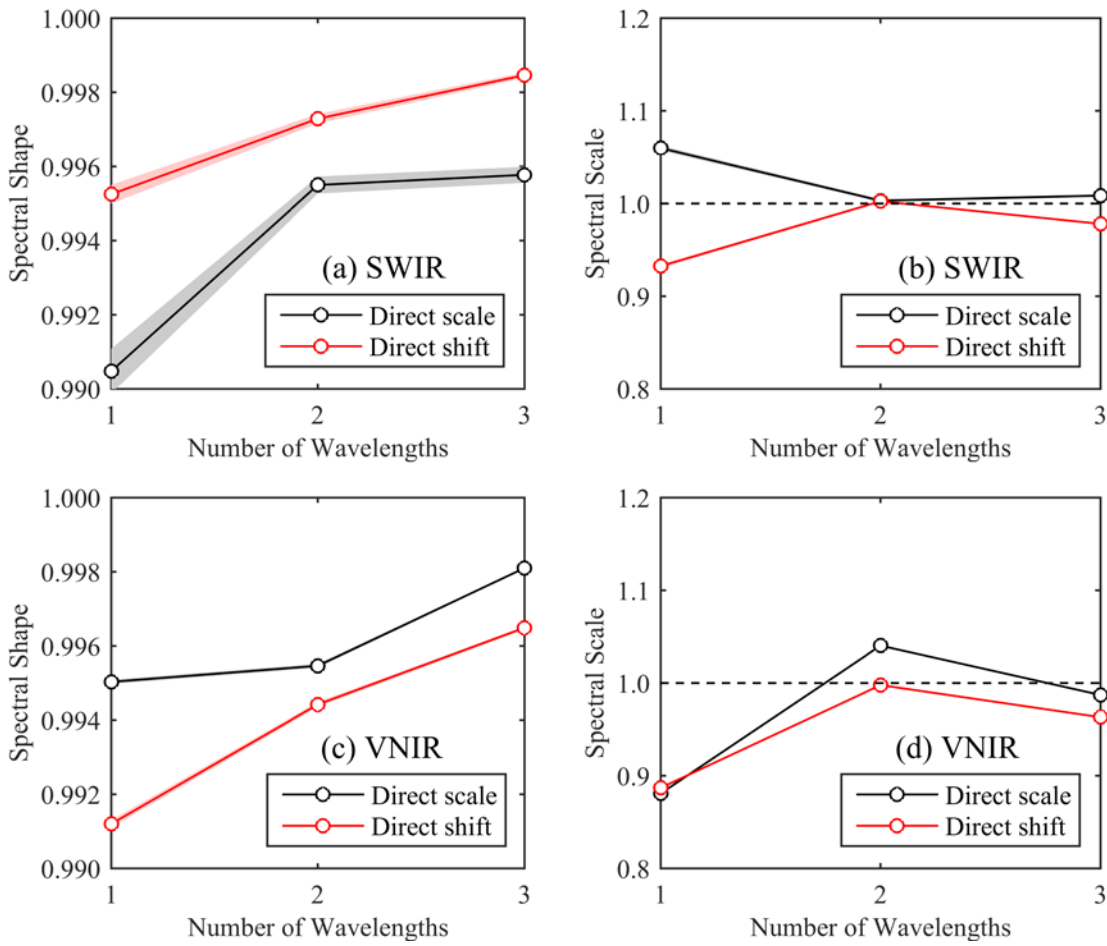


Figure 7.13: SWIR (a) spectral shape and (b) spectral scale median (solid lines) and median notch (bounding areas) versus number of direct adjustment wavelengths, limited to those wavelengths available in commercial lidar systems. VNIR metrics shown in (c) and (d).

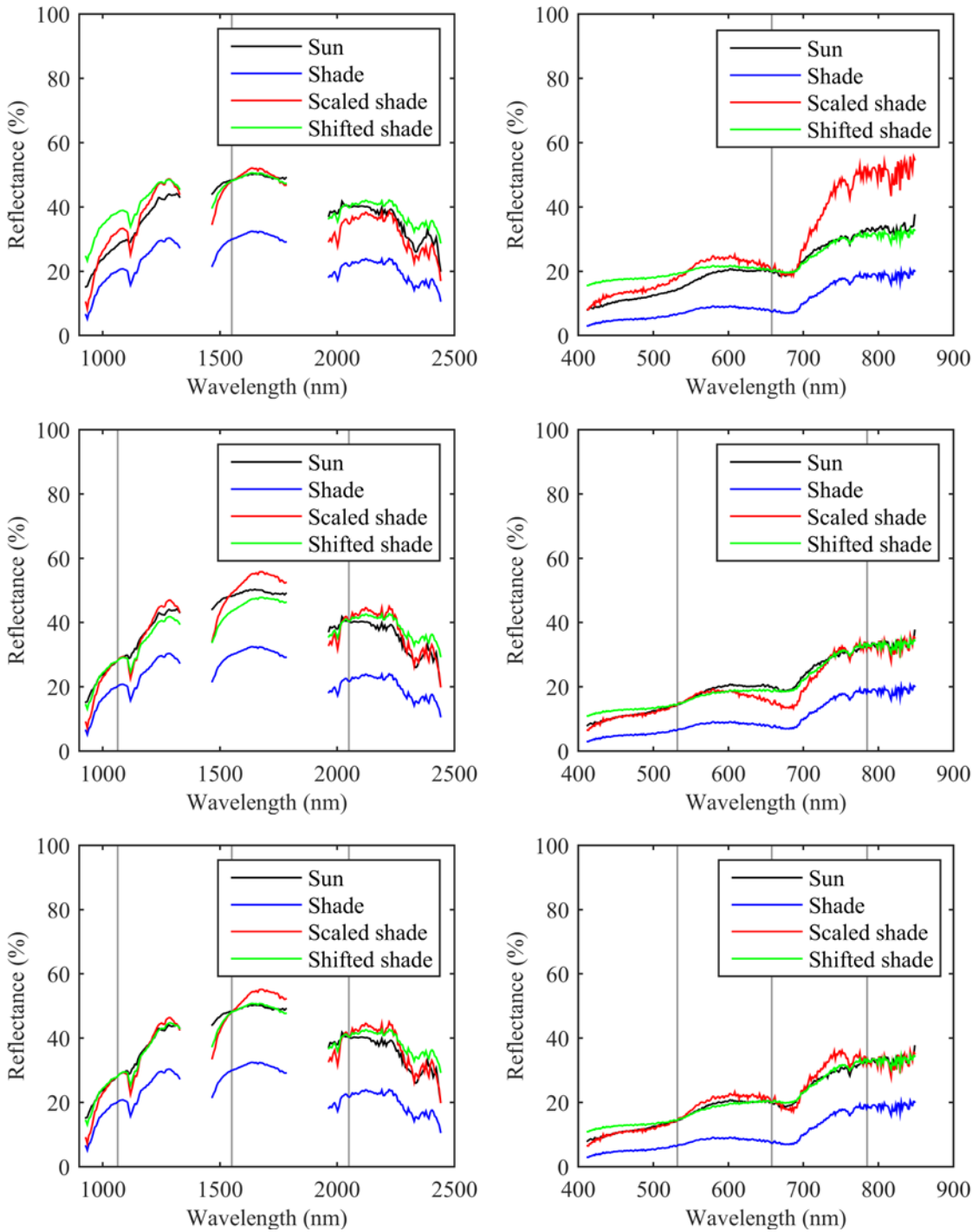


Figure 7.14: Comparison of direct scaled and direct shifted shade spectrum to matched sun spectrum using one, two and three wavelength locations. The left column is from the SWIR HSI; the right column is from the VNIR HSI.

Figure 7.15 illustrates the influence of additional scale or shift wavelength locations beyond those currently commercially available. The wavelength locations were uniformly distributed in the simulation. Although not practically realizable, the results indicate a ceiling on spectrum improvement as the number of wavelength locations is increased. The shift adjustment stabilizes more quickly than the scale adjustment, with the majority of improvement achieved with five uniformly spaced wavelengths. These results may be applicable to hyperspectral lidar systems, which currently only record backscattered laser

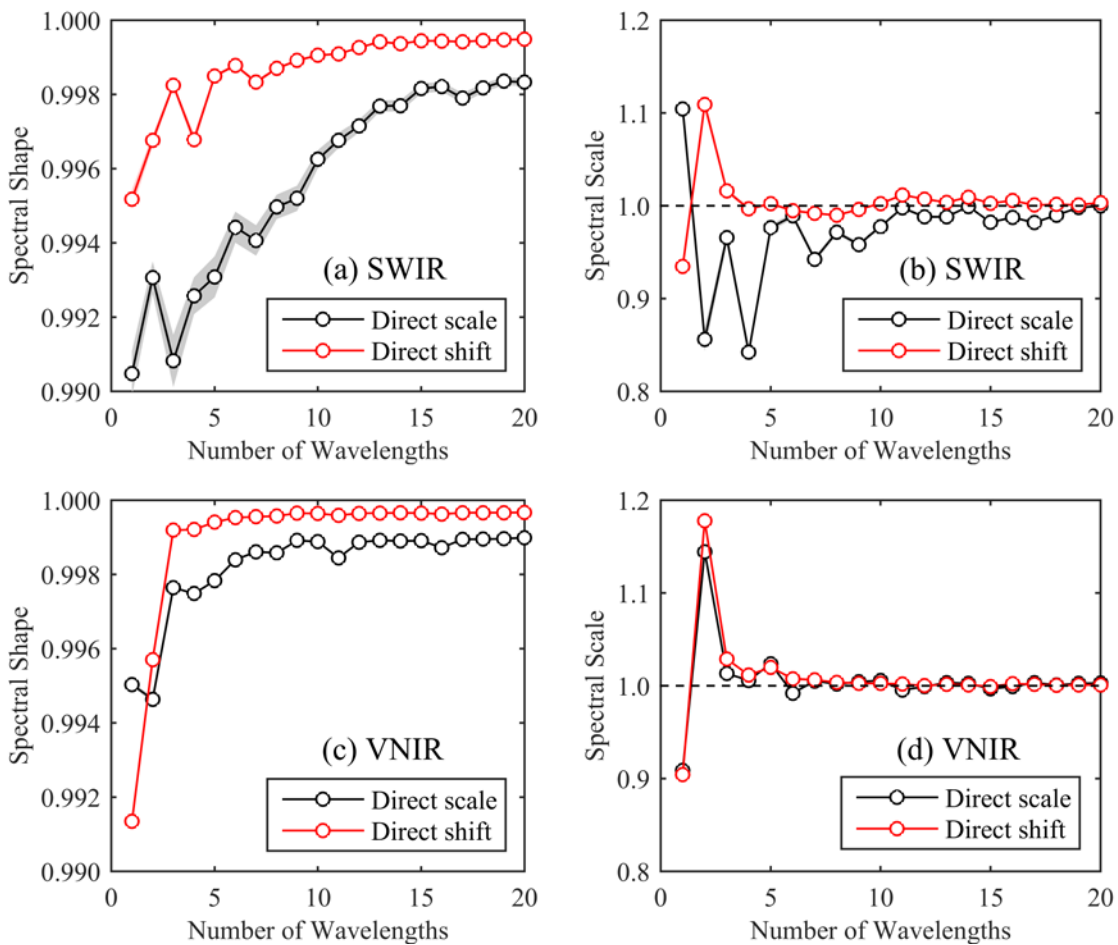


Figure 7.15: SWIR (a) spectral shape and (b) spectral scale median (solid lines) and median notch (bounding areas) metrics as a function of an increasing number of uniformly spaced direct adjustment wavelength locations. VNIR metrics are shown in (c) and (d).

intensity at a relatively small number of wavelengths (Hakala et al., 2012; Powers and Davis, 2012; Vauhkonen et al., 2013).

#### 7.2.3.3 Summary Conclusions

The proposed method of direct combination of a single active reflectance wavelength with passive HSI was shown to improve spectral scale agreement between matched sun and shade pixel pairs beyond that achieved by existing indirect shadow restoration methods. Band correlation was also greatly improved across the entire SWIR spectrum. Subsequent application of existing indirect shadow restoration methods on top of directly scaled HSI produced improvements in both spectral shape and scale. Multi-wavelength scale and shift corrections were simulated to illustrate the potential for restoring spectral shape (not just spectrum scale) through the fusion of active and passive spectral products at a lower computational cost than existing statistical restoration methods. Direct combination of active and passive spectral products should be treated with caution, however, as active and passive reflectance image products do not reside in the same domain.

#### **7.2.4 HSI Classification**

The analysis thus far has dealt with relatively small subsets of matched sun and shade pixels extracted from the partial shade images. In this final section of analysis, we generalize the spectrum restoration results to the entire image analysis area through application of SAM and MD classifiers, which illustrate the improvements in the spectral shape and spectral scale metrics, respectively. Results from a maximum (ML) classifier are also presented. The absence of change in pixel class assignment between the partial shade (original and restored) and maximum sun HSI is examined, with particular focus on those pixels with a solar

condition changing from shade to sun. Note that the same shadow restoration algorithms used for comparing the scaled and passive HSI in Section 7.2.3.1 are also used here. ENVI (Environment for Visualizing Images) software was used for all classification tasks.

#### 7.2.4.1 Classifiers

The SAM classifier evaluates the geometric angle, i.e., “spectral angle”, between each pixel spectrum and one or more reference spectra, where the angle is the arccosine of the spectral shape metric defined in Equation 7.1. Pixels are assigned to the class of the reference spectrum producing the smallest angle. If specific materials are of interest, the required reference spectra can be obtained from spectroradiometer measurements of samples taken from within the imaged scene, preexisting spectral libraries, or the spectra of manually identified pixels within the HSI image. Alternatively, spectrally “pure” endmember pixels can be extracted from the image under the assumption of linear spectral mixing. The latter method is used in this analysis and is briefly reviewed in the following section.

The MD classifier evaluates the geometric distance (Euclidean for this work) between each pixel spectrum and one or more reference spectra, with pixels assigned to the class of the nearest reference spectrum. In contrast to the SAM classifier, the MD classifier is very sensitive to spectrum magnitude and should therefore capture similar information as the spectral scale metric used in the prior analyses of the matched sun and shade pixel pairs.

Unlike the SAM and MD classifiers, the ML classifier considers sensor noise and randomness in HSI data. Instead of a single reference spectrum, each class is modeled as a multidimensional normal probability distribution function with the mean and covariance computed from a set of training pixels (Schowengerdt, 1983). Class assignment is determined by the probability distribution producing the maximum value for each pixel.

Feature reduction, often achieved through transformation of the HSI to a space that maximizes variance, is necessary prior to using the ML classifier to avoid singular covariance matrices caused by correlated HSI bands, with the added benefit of reducing the number of required training pixels. A subset of bands from a minimum noise fraction (MNF) transformation (Green et al., 1988) was used for this analysis.

#### 7.2.4.2 Endmember and Training Pixel Extraction

ENVI's Spectral Hourglass Wizard was used to extract endmember spectra from the HSI for use in the SAM and MD classifiers. The wizard consists of three basic steps:

1. Application of an MNF transformation to the HSI, which consists of whitening HSI band noise, followed by a standard principal component (PC) transformation.
2. Determination of pixel spectrum purity by repeatedly projecting the transformed pixel spectra onto random unit vectors in  $n$ -dimensional space, where  $n$  is a user-defined number of MNF bands with significant PC eigenvalues. Each time a pixel is projected to the extremes of a vector (relative to all other projected pixels) its pixel purity index is incremented.
3. Visual identification of pixels residing at the geometric extremes of scatterplots of the purest (highest index) pixels. These extreme pixels represent the endmember locations. Once identified, the endmember spectra are extracted from the original HSI image at the endmember pixel locations.

Candidate endmember pixels were restricted to those existing in the sun in both the partial shade and maximum sun images. This allowed unique endmember spectra to be extracted from each image from the same physical location, thereby accommodating any differences in illumination characteristics between the temporally spaced images that were

not removed by the EL radiometric calibration. Vegetation and calibration targets were also excluded via a manually delineated mask. Ten endmembers were identified in the SWIR HSI and seven in the VNIR (Figure 7.16). The spectra are not labeled in Figure 7.16 since there is no a priori knowledge of the material they represent; the plotted colors are sufficient to link the spectra to subsequent classification images.

The training pixel sets required for the ML classifier were also restricted to those pixels in the sun in both the partial shade and maximum sun images. The training sets were formed from the intersection of the common sun pixels and the SAM classification results, thus forming classes similar to those used in the SAM and MD analysis.

#### 7.2.4.3 Classification Results

Percentages of pixels whose classification remained the same between the partial shade and maximum sun SWIR and VNIR images for the SAM, MD and ML classifiers are given in Table 7.2. Specifically, classification agreement percentages for the total image analysis

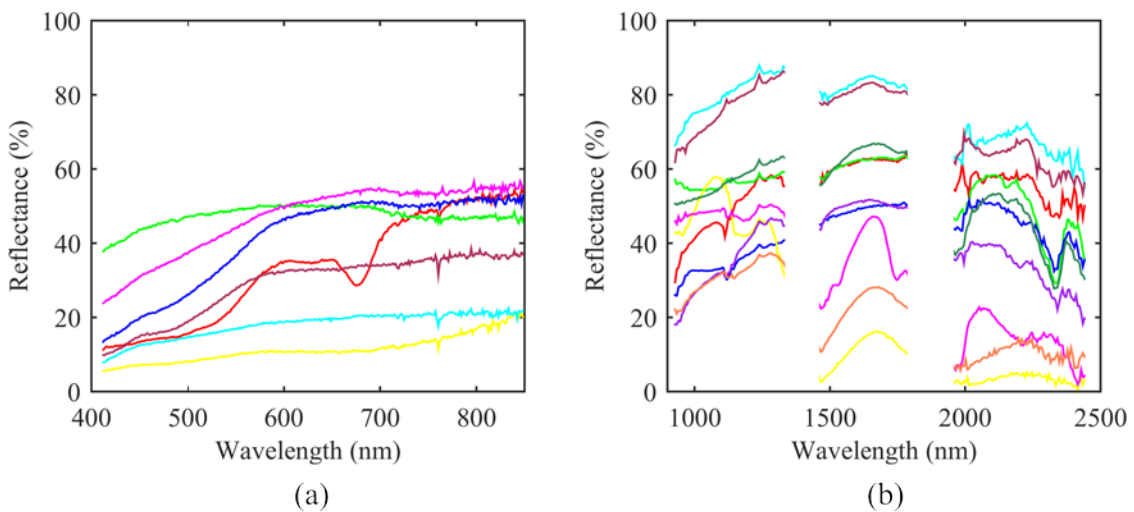


Figure 7.16: (a) VNIR and (b) SWIR endmembers. The spectra are not labeled since they do not refer to specific rock types.

Table 7.2: Percentages of pixels with unchanged class assignments generated by the SAM, MD and ML classifiers. Restored image percentages are shown in parentheses.

Classifier	Image Set	All Pixels*	Shade to Sun Pixels	Common Sun Pixels
<i>VNIR</i>				
SAM	passive	65 (70)	<b>53 (63)</b>	79
	scaled	65 (67)	<b>53 (55)</b>	80
MD	passive	57 (67)	<b>44 (62)</b>	73
	scaled	87 (75)	<b>83 (60)</b>	92
ML	passive	62 (67)	<b>48 (59)</b>	77
	scaled	51 (57)	<b>36 (46)</b>	69
<i>SWIR</i>				
SAM	passive	47 (59)	<b>33 (54)</b>	65
	scaled	48 (59)	<b>34 (53)</b>	66
MD	passive	56 (61)	<b>47 (57)</b>	66
	scaled	72 (77)	<b>64 (72)</b>	83
ML	passive	53 (53)	<b>45 (46)</b>	63
	scaled	47 (51)	<b>34 (41)</b>	63

\*Less shadowed pixel locations in the maximum sun images

area, for pixels that changed from shade to sun conditions, and for pixels that remained in the sun are given. Results are shown for the passive and directly scaled HSI both before and after shadow restoration, with the restored results given in parentheses. Since shadowed pixels in the maximum sun images were not subject to restoration, they are excluded from the total image analysis area numbers. Note that the percentages for the total image analysis area are derived from those pixels changing from shade to sun and those which remain in the sun; as such, they do not offer unique information (they are roughly midway between the other percentages) and are reported for reference only. The maximum sun SAM, MD and ML classification results for the VNIR and SWIR HSI are given in Figures 7.16 and 7.17 for reference as well.

The SAM results follow similar trends seen in the prior analyses of the matched sun and shade pixel pairs. For those pixels that change from shade to sun exposure, application of the

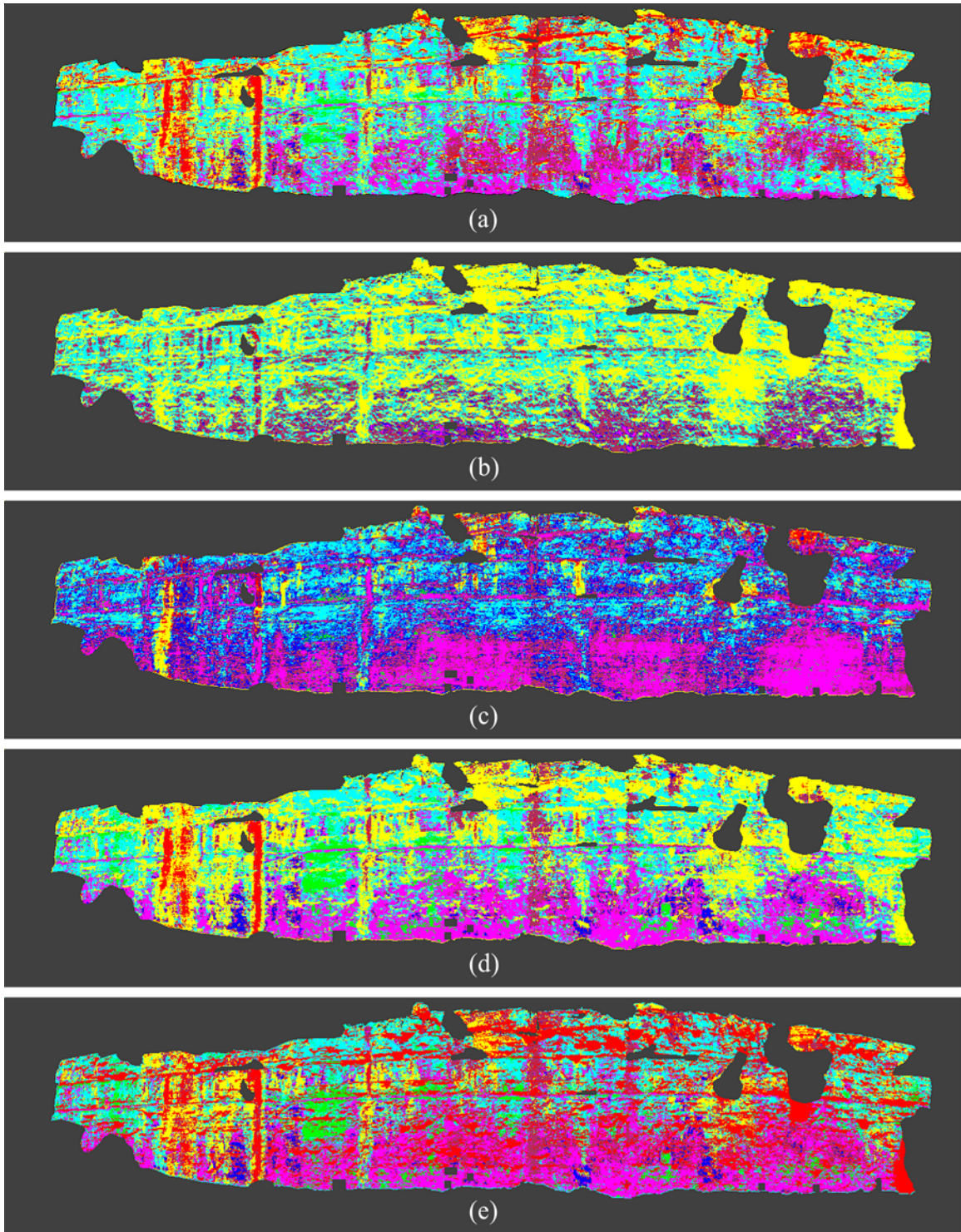


Figure 7.17: Classified VNIR maximum sun images corresponding to endmember spectra given in Figure 7.15: (a) SAM (same for passive and scaled), (b) passive MD, (c) scaled MD, (d) passive ML and (e) scaled ML.

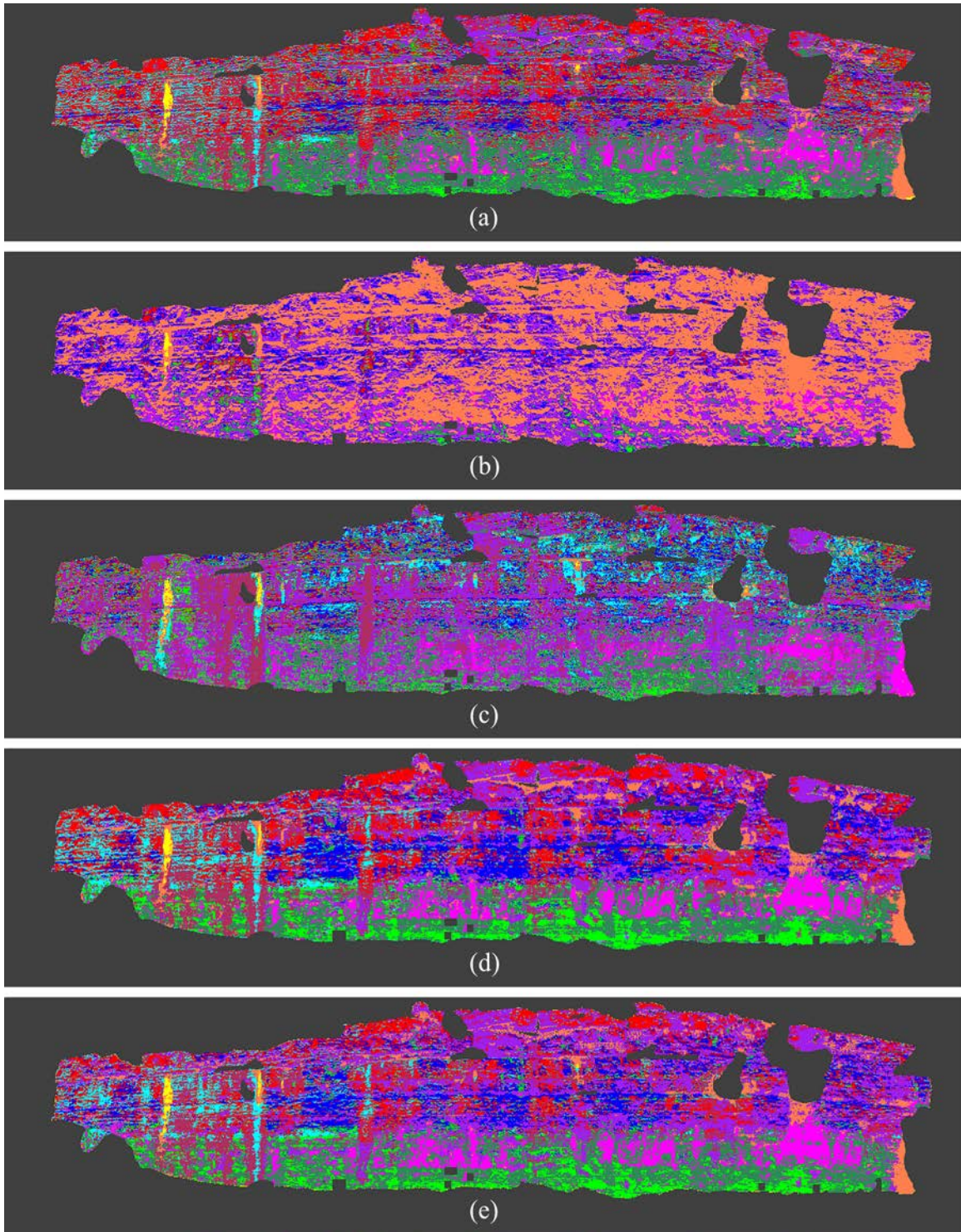


Figure 7.18: Classified SWIR maximum sun images corresponding to endmember spectra given in Figure 7.15: (a) SAM (same for passive and scaled), (b) passive MD, (c) scaled MD, (d) passive ML and (e) scaled ML.

shadow restoration algorithm boosts class stability by up to 20% for the SWIR HSI, and up to 10% for the VNIR. Note that for the unrestored images the results are almost identical between the passive and scaled images, which is expected since scaling a spectrum does not change its shape.

For the MD classification, the shadow restoration algorithm improves class stability for pixels changing from shade to sun in all cases except for the scaled VNIR HSI, which exhibited a very high agreement of 83% before restoration. The scaled HSI results are improved by 17-39% over the passive HSI, even without restoration. This supports prior analysis centering on the data presented in Figure 7.10, where the application of scale factors derived from rasterized active reflectance significantly improves the spectral scale metric over that achieved with the standard shadow restoration algorithms.

The ML classifier was applied to the first 15 bands of an MNF transformation of each image. For the pixels changing from shade to sun, the restored images show an increase in class agreement. However, the scaled HSI results are always less than the passive HSI results. This is an interesting result, as it suggests that application of the active reflectance scale factor to the HSI has removed, rather than added, information in the MNF transformed space. However, the results may be improved with a more informed method of class and training pixel selection in lieu of the current reliance on the SAM results.

The class stability for those pixels which are sunlit in both image exposures, i.e., the common sun pixels, provides context to the relatively low class agreement between those pixels changing from sun to shade conditions. Class stability in the restored shadows would not be expected to exceed that of the common sun pixels since the statistics used in the shadow restoration algorithms are derived from sunlit pixel information. The agreement

percentages are moderate, only exceeding 80% in two cases. Class agreement for the common sun pixels for the SAM classifier are of particular interest since simple changes in illumination levels caused by different sun angles should not influence the classification results. This is not the case however, with agreement reaching only 80% and 65% for the VNIR and SWIR imagery. This suggests that scattering from surrounding surfaces varies significantly across the outcrop as a function of sun angle, a characteristic that the standard method of EL radiometric calibration (used in this dissertation) cannot accommodate. This motivates the investigation of RTM or multi-wavelength scaling solutions for more reliable recovery of scene reflectance spectra in high resolution terrestrial HSI.

## Chapter 8

### Conclusions and Recommendations

#### 8.1 Conclusions

Shadow pixels were detected in terrestrial HSI by projecting each image pixel to a mesh surface in 3D object space and then testing the projected points for occlusion with respect to the solar position at the time of HSI acquisition. Pixel-level shadow detection accuracy was visually observed and indirectly validated by consistently superior correlation with non-shadowed (full shade) HSI bands when using sub-pixel shadow detection as opposed to binary pixel shadow detection. The positive results affirm that structural shadow detection in high resolution terrestrial HSI is achievable using fused TLS spatial data with standard field collection procedures.

Statistical mean scale and linear correlation correction restoration methods were applied in a band by band fashion to each distinct shadow area in partially shaded SWIR and VNIR HSI. The restoration methods performed similarly, with mean improvements in spectral shape and spectral scale medians of 77% and 92% for the SWIR HSI and 45% and 92% for the VNIR HSI. The use of lidar active reflectance information to assist in identifying regions of common material existing in the sun and shade, which is required for the restoration methods, was tested against purely spatial methods and found to have a small positive influence on spectral shape in the SWIR HSI, but at the cost of spatial artifacts. Active lidar reflectance was not found to improve the VNIR restoration results, potentially due to the smaller amount of spectral variance at the 532 nm active reflectance wavelength used for

identifying common regions in the VNIR HSI compared to the 1550 nm wavelength used for the SWIR HSI.

A method for directly scaling passive HSI spectra with the ratio of the active to passive reflectance products at their common wavelength was proposed to improve the spectral scale, i.e., magnitude, of the restored shadow spectra. A 40% improvement in spectral scale IQR over that achieved with the standard restoration methods was demonstrated for both the SWIR and VNIR HSI. Since a scale factor does not alter spectral shape, the direct scale results were combined with the statistical restoration methods and the results shown to produce improvements in both the spectral shape and spectral scale metrics.

The proposed scalar method of combining the active and passive spectral products is attractive in its simplicity. Shadow detection is eliminated, identification of common materials in the sun and shade is not required, and the computational load is reduced to a simple scale factor. However, a single scale factor does not restore spectral shape, and is thus not a true restoration technique given the differences in incident spectral irradiance between sunlit and shadowed surfaces. The use of multiple active reflectance wavelengths with an interpolated scale or shift was proposed as a solution to this deficiency. Simulations were applied to the SWIR and VNIR HSI using laser wavelengths available in existing commercial lidar sensors as well as a more general simulation using uniformly spaced wavelengths. Spectral scale and spectral shape were both improved, with the simulation employing uniform wavelength locations achieving the majority of improvement with only five wavelengths. However, beyond the fact that the simulations did not incorporate estimated error in the active reflectance adjustments, it is important to realize that scaling

passive HSI with active reflectance products transforms the HSI to a different domain, potentially reducing the effectiveness of standard passive spectral libraries for HSI analysis.

Finally, several classification algorithms were applied to the original and restored partial shade HSI and compared to classification results obtained from the maximum sun HSI. The classification comparison supported conclusions from the prior analysis based on matched sun and shade pixel pairs, indicating improvements in spectral shape and scale. Perhaps most interesting was the low agreement, less than 80%, produced by the SAM classifier between pixels that remained in the sun in both the partial shade and maximum sun HSI. This suggests that scattering from surrounding topography cannot be considered negligible in sunlight conditions for geologic outcrop analysis.

## **8.2 Recommendations**

This dissertation has shown the feasibility of shadow detection and restoration in high resolution terrestrial HSI using fused TLS spatial and spectral information. However, there are several areas where practical improvements can be made in current data collection and processing workflows, and at least a few avenues of research into more robust restoration techniques exist.

With respect to practical improvements, it is recommended that the HSI cameras be rigidly mounted on top of a TLS instrument rather than their current deployment on a separate tripod mounted rotation stage. Fixed rotation and translation transformation parameters between the camera and TLS coordinate systems can then be determined, which will eliminate the tedious work of identifying matched object and image space points currently required in order to solve the camera EO registration parameters for each HSI.

Capturing the spatial and spectral information from very nearly the same location will also eliminate the occlusion analysis required when rasterizing active reflectance products to the HSI pixel coordinate system as well as the occasional voids that currently exist in the rasterized active reflectance images.

Optimization of the ray tracing computation code, which is used for shadow determination, occlusion analysis when rasterizing the active lidar reflectance, and co-registering the HSI to a common pixel coordinate system, is also recommended. The current implementation uses MATLAB for data parsing and scene voxelization and a C++ MEX file for the geometric intersection computations, with code execution taking several hours for each occlusion analysis task. Movement of the entire code base to C++, and potentially executing the geometric intersection computations on a graphics processing unit (GPU), is recommended. This is particularly relevant if future work is to involve computing sky view fractions, which require extensive ray tracing computations for each pixel.

Investigation into techniques for more robust radiometric calibration and rasterization of the active lidar reflectance data is also recommended. For radiometric calibration, the practicality of removing the non-Lambertian scattering characteristics with respect to incidence angle should be assessed. The method recently demonstrated by Carrea et al. (2016) using Oren and Nayar's (1995) scattering model appears promising, but may require modification of current data collection workflows in order to observe outcrop surfaces from several angles. For rasterized active reflectance, investigation of the influence of the camera pixel response function and the non-point nature of lidar spot size is recommended. A pixel response function defines the contribution of location within a single pixel to the overall pixel brightness (Fumo et al., 2015) and may be relevant for imagery where pixel sizes are

large compared to lidar spot sizes, e.g., the SWIR camera used in this dissertation. Lidar spot size and power profile shape may be important for imagery where the pixel and lidar spot sizes are of similar magnitude and the lidar spot illuminates multiple pixels.

In terms of broad research avenues investigating more robust recovery of scene reflectance spectra in terrestrial HSI, the use of RTM-based methods in lieu of statistical restoration is a natural extension of this work. Current RTM solutions cannot accommodate horizontal viewing perspectives and, at best, incorporate 2.5D DSMs for determining occlusion and scattering by adjacent objects. However, their basis on realistic models of atmospheric scattering and absorption and their broad acceptance in airborne HSI analysis merits their extension to terrestrial HSI.

Although RTM-based restoration of terrestrial HSI is more rigorous than statistical methods given its basis on physical principles, it is computationally expensive and still subject to artifacts caused by shadow determination errors. The application of multiple active reflectance scale factors to passive HSI has neither of these drawbacks, but was only able to be simulated in this dissertation. Additional research to determine the effectiveness of multi-wavelength spectrum scaling on pixel spectrum restoration with real data, and whether similar information can be extracted from such scaled HSI compared to standard passive HSI is therefore recommended. Even with reduced spectral fidelity, the simplicity and speed of the method is attractive, with potential application to real-time data collection.

In summary, it is hoped that the work in this dissertation will serve as a foundation for further investigation into robust and efficient terrestrial HSI restoration techniques. The complex illumination environments captured by close-range, high resolution HSI makes

recovery of shadowed surface reflectance spectra a challenging task, but the value of accurate image based spectroscopy is high.

## References

- Adeline, K., Paparoditis, N., Briottet, X., and Gastellu-Etchegorry, J.P., 2013a. “Material Reflectance Retrieval in Urban Tree Shadows with Physics-Based Empirical Atmospheric Correction.” *In: Joint Urban Remote Sensing Event 2013*. São Paulo, Brazil, 279–283.
- Adeline, K.R.M., Chen, M., Briottet, X., Pang, S.K., and Paparoditis, N., 2013b. “Shadow Detection in Very High Spatial Resolution Aerial Images: A Comparative Study.” *ISPRS Journal of Photogrammetry and Remote Sensing*, 80, 21–38.
- Adler-Golden, S.M., Matthew, M.W., Anderson, G.P., Felde, G.W., and Gardner, J.A., 2002. “An Algorithm for De-Shadowing Spectral Imagery.” *In: Proceedings of the 11th JPL Airborne Earth Science Workshop*. Pasadena, California, 203–210.
- Alexander, J., 1992. “A Discussion on the Use of Analogues for Reservoir Geology.” *Geological Society, London, Special Publications*, 69 (1), 175–194.
- Bergstrand, E., 1949a. “Velocity of Light and Measurement of Distance by High-Frequency Light Signalling.” *Nature*, 163, 338.
- Bergstrand, E., 1949b. “Measurement of Distances by High Frequency Light Signalling.” *Bulletin géodésique*, 11 (1), 81–92.
- Biavati, G., Di Donfrancesco, G., Cairo, F., and Feist, D.G., 2011. “Correction Scheme for Close-Range Lidar Returns.” *Applied Optics*, 50 (30), 5872–82.
- Brazile, J., Richter, R., Schläpfer, D., Schaepman, M.E., and Itten, K.I., 2008. “Cluster Versus Grid for Operational Generation of ATCOR’s Modtran-Based Look Up Tables.” *Parallel Computing*, 34 (1), 32–46.
- Briese, C., Höfle, B., Lehner, H., Wagner, W., Pfennigbauer, M., and Ullrich, A., 2008.

- “Calibration of Full-Waveform Airborne Laser Scanning Data for Object Classification.” *In: Proceedings of SPIE 6950, Laser Radar Technology and Applications XIII*. Orlando, Florida, 69500H–69500H–8.
- Buckley, S.J., Enge, H.D., Carlsson, C., and Howell, J.A., 2010. “Terrestrial Laser Scanning for use in Virtual Outcrop Geology.” *The Photogrammetric Record*, 25 (131), 225–239.
- Buckley, S.J., Howell, J.A., Enge, H.D., and Kurz, T.H., 2008. “Terrestrial Laser Scanning in Geology: Data Acquisition, Processing and Accuracy Considerations.” *Journal of the Geological Society*, 165 (3), 625–638.
- Buckley, S.J., Kurz, T.H., Howell, J.A., and Schneider, D., 2013. “Terrestrial Lidar and Hyperspectral Data Fusion Products for Geological Outcrop Analysis.” *Computers & Geosciences*, 54, 249–258.
- Burton, D., Dunlap, D.B., Wood, L.J., and Flaig, P.P., 2011. “Lidar Intensity as a Remote Sensor of Rock Properties.” *Journal of Sedimentary Research*, 81 (5), 339–347.
- Carrea, D., Abellan, A., Humair, F., Matasci, B., Derron, M.-H., and Jaboyedoff, M., 2016. “Correction of Terrestrial LiDAR Intensity Channel Using Oren–Nayar Reflectance Model: An Application to Lithological Differentiation.” *ISPRS Journal of Photogrammetry and Remote Sensing*, 113, 17–29.
- Carrere, V. and Abrams, M.J., 1988. “An Assessment of AVIRIS Data for Hydrothermal Alteration Mapping in the Goldfield Mining District, Nevada.” *In: Proceedings of the Airborne Visible/Infrared Imaging Spectrometer (AVIRIS) Performance Evaluation Workshop*. Pasadena, California, 134–154.
- Clark, R.N., 1999. “Chapter 1: Spectroscopy of Rocks and Minerals, and Principles of Spectroscopy.” *In: A.N. Rencz, ed. Manual of Remote Sensing, Volume 3, Remote*

- Sensing for the Earth Sciences. New York, NY: John Wiley & Sons, 3–58.
- Clark, R.N., Swayze, G.A., Livo, K.E., Kokaly, R.F., King, T.V.V., Dalton, J.B., Vance, J.S., Rockwell, B.W., Hoefen, T., and McDougal, R.R., 2002. “Surface Reflectance Calibration of Terrestrial Imaging Spectroscopy Data: a Tutorial Using AVIRIS.” *In: Proceedings of the 10th Airborne Earth Science Workshop*. Pasadena, California.
- CloudCompare v.2.6.1, 2015. Software. Retrieved from <http://www.cloudcompare.org>.
- Comaniciu, D. and Meer, P., 2002. “Mean Shift: a Robust Approach Toward Feature Space Analysis.” *IEEE Transactions on Pattern Analysis and Machine Intelligence*, 24 (5), 603–619.
- Corey, R., 1995. “Coherent Backscattering of Light.” *American Journal of Physics*, 63 (6), 560.
- Dare, P.M., 2005. “Shadow Analysis in High-Resolution Satellite Imagery of Urban Areas.” *Photogrammetric Engineering & Remote Sensing*, 71 (2), 169–177.
- Eismann, M.T., 2012. Hyperspectral Remote Sensing. Bellingham, WA: SPIE.
- Fang, W., Huang, X., Zhang, F., and Li, D., 2015. “Intensity Correction of Terrestrial Laser Scanning Data by Estimating Laser Transmission Function.” *IEEE Transactions on Geoscience and Remote Sensing*, 53 (2), 942–951.
- Franceschi, M., Teza, G., Preto, N., Pesci, A., Galgaro, A., and Girardi, S., 2009. “Discrimination Between Marls and Limestones Using Intensity Data From Terrestrial Laser Scanner.” *ISPRS Journal of Photogrammetry and Remote Sensing*, 64 (6), 522–528.
- Fredembach, C. and Finlayson, G., 2006. “Simple Shadow Removal.” *In: 18th International Conference on Pattern Recognition*. Hong Kong, 832–835.

- Friman, O., Tolt, G., and Ahlberg, J., 2011. "Illumination and Shadow Compensation of Hyperspectral Images Using a Digital Surface Model and Non-Linear Least Squares Estimation." *In: Proceedings of SPIE Remote Sensing 2011*. Prague, 81800Q–81800Q–8.
- Fumo, P., Waldron, E., Laine, J.-P., and Evans, G., 2015. "Pixel Response Function Experimental Techniques and Analysis of Active Pixel Sensor Star Cameras." *Journal of Astronomical Telescopes, Instruments, and Systems*, 1 (2), 028002.
- Goetz, A.F., Vane, G., Solomon, J.E., and Rock, B.N., 1985. "Imaging Spectrometry for Earth Remote Sensing." *Science*, 228 (4704), 1147–1153.
- Goetz, A.F.H., 2009. "Three decades of Hyperspectral Remote Sensing of the Earth: A Personal View." *Remote Sensing of Environment*, 113, S5–S16.
- Green, A.A., Berman, M., Switzer, P., and Craig, M.D., 1988. "Transformation for Ordering Multispectral Data in Terms of Image Quality With Implications for Noise Removal." *IEEE Transactions on Geoscience and Remote Sensing*, 26 (1), 65–74.
- Hakala, T., Suomalainen, J., Kaasalainen, S., and Chen, Y., 2012. "Full Waveform Hyperspectral LiDAR for Terrestrial Laser Scanning." *Optics Express*, 20 (7), 7119–7127.
- Han, T., Goodenough, D.G., Dyk, A., and Love, J., 2002. "Detection and Correction of Abnormal Pixels in Hyperion Images." *In: IEEE International Geoscience and Remote Sensing Symposium*. Toronto, 1327–1330.
- Hartzell, P., Glennie, C., Biber, K., and Khan, S., 2014. "Application of Multispectral LiDAR to Automated Virtual Outcrop Geology." *ISPRS Journal of Photogrammetry and Remote Sensing*, 88, 147–155.

- Hartzell, P.J., Glennie, C.L., and Finnegan, D.C., 2015. "Empirical Waveform Decomposition and Radiometric Calibration of a Terrestrial Full-Waveform Laser Scanner." *IEEE Transactions on Geoscience and Remote Sensing*, 53 (1), 162–172.
- Hecht, J., 2010. "Short History of Laser Development." *Optical Engineering*, 49 (9), 1–23.
- Höfle, B. and Pfeifer, N., 2007. "Correction of Laser Scanning Intensity Data: Data and Model-Driven Approaches." *ISPRS Journal of Photogrammetry and Remote Sensing*, 62 (6), 415–433.
- Ientilucci, E.J., 2013. "SHARE 2012: Analysis of Illumination Differences on Targets in Hyperspectral Imagery." In: *Proceedings of SPIE, Algorithms and Technologies for Multispectral, Hyperspectral, and Ultraspectral Imagery XIX*. Baltimore, Maryland.
- Jelalian, A.V., 1992. Laser Radar Systems. Norwood, MA: Artech House.
- Joerg, P.C., Weyermann, J., Morsdorf, F., Zemp, M., and Schaepman, M.E., 2015. "Computation of a Distributed Glacier Surface Albedo Proxy Using Airborne Laser Scanning Intensity Data and In-Situ Spectro-Radiometric Measurements." *Remote Sensing of Environment*, 160, 31–42.
- Jutzi, B. and Stilla, U., 2006. "Range Determination with Waveform Recording Laser Systems Using a Wiener Filter." *ISPRS Journal of Photogrammetry and Remote Sensing*, 61 (2), 95–107.
- Kaasalainen, M. and Kaasalainen, S., 2008. "Aperture Size Effects on Backscatter Intensity Measurements in Earth and Space Remote Sensing." *Journal of the Optical Society of America A*, 25 (5), 1142–1146.
- Kaasalainen, S., Ahokas, E., Hyypä, J., and Suomalainen, J., 2005. "Study of Surface Brightness From Backscattered Laser Intensity: Calibration of Laser Data." *IEEE*

- Geoscience and Remote Sensing Letters*, 2 (3), 255–259.
- Kaasalainen, S., Hyypä, H., Kukko, A., Litkey, P., Ahokas, E., Hyypä, J., Lehner, H., Jaakkola, A., Suomalainen, J., Akujarvi, A., Kaasalainen, M., and Pyysalo, U., 2009. “Radiometric Calibration of LIDAR Intensity With Commercially Available Reference Targets.” *IEEE Transactions on Geoscience and Remote Sensing*, 47 (2), 588–598.
- Kaasalainen, S., Jaakkola, A., Kaasalainen, M., Krooks, A., and Kukko, A., 2011a. “Analysis of Incidence Angle and Distance Effects on Terrestrial Laser Scanner Intensity: Search for Correction Methods.” *Remote Sensing*, 3 (12), 2207–2221.
- Kaasalainen, S., Pyysalo, U., Krooks, A., Vain, A., Kukko, A., Hyypä, J., and Kaasalainen, M., 2011b. “Absolute Radiometric Calibration of ALS Intensity Data: Effects on Accuracy and Target Classification.” *Sensors*, 11 (11), 10586–602.
- Kashani, A., Olsen, M., Parrish, C., and Wilson, N., 2015. “A Review of LIDAR Radiometric Processing: From Ad Hoc Intensity Correction to Rigorous Radiometric Calibration.” *Sensors*, 15 (11), 28099–28128.
- Kazhdan, M. and Hoppe, H., 2013. “Screened Poisson Surface Reconstruction.” *ACM Transactions on Graphics*, 32 (3), 1–13.
- Kruse, F.A., 1988. “Use of Airborne Imaging Spectrometer Data to Map Minerals Associated with Hydrothermally Altered Rocks in the Northern Grapevine Mountains, Nevada, and California.” *Remote Sensing of Environment*, 24 (1), 31–51.
- Kurz, T.H., Buckley, S.J., Howell, J.A., and Schneider, D., 2011. “Integration of Panoramic Hyperspectral Imaging with Terrestrial Lidar Data.” *The Photogrammetric Record*, 26 (134), 212–228.
- Kurz, T.H., Buckley, S.J., and Howell, J.A., 2013. “Close-range Hyperspectral Imaging for

- Geological Field Studies: Workflow and Methods.” *International Journal of Remote Sensing*, 34 (5), 1798–1822.
- Kurz, T.H., Dewit, J., Buckley, S.J., Thurmond, J.B., Hunt, D.W., and Swennen, R., 2012. “Hyperspectral Image Analysis of Different Carbonate Lithologies (Limestone, Karst and Hydrothermal Dolomites): the Pozalagua Quarry Case Study (Cantabria, Northwest Spain).” *Sedimentology*, 59 (2), 623–645.
- Labsphere, 2013. Technical Guide, Reflectance Materials and Coatings. Retrieved from <http://www.labsphere.com/uploads/technical-guides/a-guide-to-reflectance-materials-and-coatings.pdf>.
- Lachérade, S., Miesch, C., Boldo, D., Briottet, X., Valorge, C., and Le Men, H., 2008. “ICARE: A Physically-Based Model to Correct Atmospheric and Geometric Effects from High Spatial and Spectral Remote Sensing Images Over 3D Urban Areas.” *Meteorology and Atmospheric Physics*, 102, 209–222.
- Lehner, H. and Briese, C., 2010. “Radiometric Calibration of Full-Waveform Airborne Laser Scanning Data Based on Natural Surfaces.” *International Archives of the Photogrammetry, Remote Sensing and Spatial Information Sciences 38 (Part 7B)*. 360–365.
- Li, Y., Gong, P., and Sasagawa, T., 2005. “Integrated Shadow Removal Based on Photogrammetry and Image Analysis.” *International Journal of Remote Sensing*, 26 (18), 3911–3929.
- Luhman, T., Robson, S., Kyle, S., and Harley, I., 2011. Close Range Photogrammetry. Dunbeath, Scotland: Whittles Publishing.
- McGill, R., Tukey, J.W., and Larsen, W.A., 1978. “Variations of Box Plots.” *The American*

- Statistician*, 32 (1), 12.
- Möller, T. and Trumbore, B., 1997. "Fast, Minimum Storage Ray-Triangle Intersection." *Journal of Graphics Tools*, 2 (1), 21–28.
- Murphy, R.J., Monteiro, S.T., and Schneider, S., 2012. "Evaluating Classification Techniques for Mapping Vertical Geology Using Field-Based Hyperspectral Sensors." *IEEE Transactions on Geoscience and Remote Sensing*, 50 (8), 3066–3080.
- Murphy, R.J., Schneider, S., Taylor, Z., and Nieto, J., 2014. "Mapping Clay Minerals in an Open-Pit Mine Using Hyperspectral Imagery and Automated Feature Extraction." *In: Vertical Geology Conference*. Lausanne, Switzerland.
- Nagao, M., Matsuyama, T., and Ikeda, Y., 1979. "Region Extraction and Shape Analysis in Aerial Photographs." *Computer Graphics and Image Processing*, 10 (3), 195–223.
- NOAA, 2012. "AGA Geodimeters, Models RD and FL". Retrieved from [http://celebrating200years.noaa.gov/distance\\_tools/geodimeters\\_4d\\_4l.html](http://celebrating200years.noaa.gov/distance_tools/geodimeters_4d_4l.html).
- Oren, M. and Nayar, S.K., 1995. "Generalization of the Lambertian Model and Implications for Machine Vision." *International Journal of Computer Vision*, 14 (3), 227–251.
- Pal, M. and Mather, P.M., 2004. "Assessment of the Effectiveness of Support Vector Machines for Hyperspectral Data." *Future Generation Computer Systems*, 20 (7), 1215–1225.
- Papetti, T.J., Walker, W.E., Keffer, C.E., and Johnson, B.E., 2007. "Coherent Backscatter: Measurement of the Retroreflective BRDF Peak Exhibited by Several Surfaces Relevant to Ladar Applications." *In: Proceedings of SPIE 6682, Polarization Science and Remote Sensing III*. San Diego, California, 66820E–66820E–13.
- Parrish, C.E., Jeong, I., Nowak, R.D., and Smith, R.B., 2011. "Empirical Comparison of

- Full-Waveform Lidar Algorithms : Range Extraction and Discrimination Performance.” *Photogrammetric Engineering & Remote Sensing*, 77 (8), 825–838.
- Pfennigbauer, M. and Ullrich, A., 2010. “Improving Quality of Laser Scanning Data Acquisition through Calibrated Amplitude and Pulse Deviation Measurement.” *In: Proceedings of SPIE 7684, Laser Radar Technology and Applications XV*. Orlando, Florida, 76841F–76841F–10.
- Pfennigbauer, M. and Ullrich, A., 2011. “Multi-Wavelength Airborne Laser Scanning, PowerPoint Presentation.” *International LiDAR Mapping Forum*. New Orleans, Louisiana.
- Pfennigbauer, M., Wolf, C., and Ullrich, A., 2013. “Enhancing Online Waveform Processing by Adding New Point Attributes.” *In: Proceedings of SPIE 8731, Laser Radar Technology and Applications XVIII*. Baltimore, Maryland, 873104–873104–9.
- Powers, M.A. and Davis, C.C., 2012. “Spectral LADAR: Active Range-Resolved Three-Dimensional Imaging Spectroscopy.” *Applied Optics*, 51 (10), 1468–1478.
- Rau, J., Chen, N., and Chen, L., 2002. “True Orthophoto Generation of Built-Up Areas Using Multi-View Images.” *Photogrammetric Engineering & Remote Sensing*, 68 (6), 581–588.
- Reda, I. and Andreas, A., 2004. “Solar Position Algorithm for Solar Radiation Applications.” *Solar Energy*, 76 (5), 577–589.
- Riegler LMS GmbH, 2015. RiSCAN PRO v. 2.1.2. Software.
- Roncat, A., Lehner, H., and Briese, C., 2011. “Laser Pulse Variations and their Influence on Radiometric Calibration of Full-Waveform Laser Scanner Data.” *International Archives of the Photogrammetry, Remote Sensing and Spatial Information Sciences* 38 (5/W12).

- Sarabandi, P., Yamazaki, F., Matsuoka, M., and Kiremidjian, A., 2004. "Shadow Detection and Radiometric Restoration in Satellite High Resolution Images." *In: IEEE International Geoscience and Remote Sensing Symposium, 2004*. Anchorage, Alaska, 3744–3747.
- Schaepman, M.E., Ustin, S.L., Plaza, A.J., Painter, T.H., Verrelst, J., and Liang, S., 2009. "Earth System Science Related Imaging Spectroscopy-An Assessment." *Remote Sensing of Environment*, 113, S123–S137.
- Scheibe, K., Huang, F., and Klette, R., 2009. "Calibration of Rotating Sensors." *In: X. Jiang and N. Petkov, eds. Computer Analysis of Images and Patterns*. Berlin, Germany: Springer, 157–164.
- Schläpfer, D., Richter, R., and Damm, A., 2013. "Correction of Shadowing in Imaging Spectroscopy Data by Quantification of the Proportion of Diffuse Illumination." *In: 8th SIG-IS EARSeL Imaging Spectroscopy Workshop*. Nantes, France.
- Schneider, D. and Maas, H.-G., 2006. "A Geometric Model for Linear-Array-Based Terrestrial Panoramic Cameras." *The Photogrammetric Record*, 21 (115), 198–210.
- Schowengerdt, R.A., 1983. Techniques for Image Processing and Classification in Remote Sensing. New York, NY: Academic Press.
- Shan, J. and Toth, C.K., eds., 2008. Topographic Laser Ranging and Scanning: Principles and Processing. 1st ed. Boca Raton, FL: CRC Press.
- Spectral Imaging Ltd., 2014. SWIR Spectral Camera Data Sheet, v.1-09.
- Tolt, G., Shimoni, M., and Ahlberg, J., 2011. "A Shadow Detection Method for Remote Sensing Images Using VHR Hyperspectral and LIDAR Data." *In: 2011 IEEE International Geoscience and Remote Sensing Symposium*. Vancouver, Canada, 4423–

4426.

- Tsai, V.J.D., 2006. "A Comparative Study on Shadow Compensation of Color Aerial Images in Invariant Color Models." *IEEE Transactions on Geoscience and Remote Sensing*, 44 (6), 1661–1671.
- Ullrich, A. and Pfennigbauer, M., 2011. "Echo Digitization and Waveform Analysis in Airborne and Terrestrial Laser Scanning." *In: 53rd Photogrammetric Week*. Stuttgart, Germany, 217–228.
- van der Meer, F.D., van der Werff, H.M.A., van Ruitenbeek, F.J.A., Hecker, C.A., Bakker, W.H., Noomen, M.F., van der Meijde, M., Carranza, E.J.M., Smeth, J.B. de, and Woldai, T., 2012. "Multi- and Hyperspectral Geologic Remote Sensing: A Review." *International Journal of Applied Earth Observation and Geoinformation*, 14 (1), 112–128.
- Vauhkonen, J., Hakala, T., Suomalainen, J., Kaasalainen, S., Nevalainen, O., Vastaranta, M., Holopainen, M., and Hyypä, J., 2013. "Classification of Spruce and Pine Trees Using Active Hyperspectral LiDAR." *IEEE Geoscience and Remote Sensing Letters*, 10 (5), 1138–1141.
- Vosselman, G. and Maas, H., eds., 2010. Airborne and Terrestrial Laser Scanning. 1st ed. Dunbeath, Scotland: Whittles Publishing.
- Wagner, W., 2010. "Radiometric Calibration of Small-Footprint Full-Waveform Airborne Laser Scanner Measurements: Basic Physical Concepts." *ISPRS Journal of Photogrammetry and Remote Sensing*, 65 (6), 505–513.
- Wagner, W., Ullrich, A., Ducic, V., Melzer, T., and Studnicka, N., 2006. "Gaussian Decomposition and Calibration of a Novel Small-Footprint Full-Waveform Digitising

- Airborne Laser Scanner.” *ISPRS Journal of Photogrammetry and Remote Sensing*, 60 (2), 100–112.
- Wolf, P.R. and Ghilani, C.D., 2001. Elementary Surveying. 10th ed. Upper Saddle River, NJ: Prentice Hall.
- Wolfe, W.L., 1998. Introduction to Radiometry. Bellingham, WA: SPIE.
- Xia, H., Chen, X., and Guo, P., 2009. “A Shadow Detection Method for Remote Sensing Images Using Affinity Propagation Algorithm.” *In: 2009 IEEE International Conference on Systems, Man and Cybernetics*. San Antonio, Texas, 3116–3121.
- Zhan, Q., Shi, W., and Xiao, Y., 2005. “Quantitative Analysis of Shadow Effects in High-Resolution Images of Urban Areas.” *International Archives of Photogrammetry and Remote Sensing* 36 (8/W27).
- Zhang, Q., Pa, V., and Plemmons, R.J., 2013. “Detecting Objects Under Shadows by Fusion of Hyperspectral and Lidar Data: A Physical Model Approach.” *In: IEEE WHISPERS*. Gainesville, Florida.
- Zhou, W., Huang, G., Troy, A., and Cadenasso, M.L., 2009. “Object-Based Land Cover Classification of Shaded Areas in High Spatial Resolution Imagery of Urban Areas: A Comparison Study.” *Remote Sensing of Environment*, 113 (8), 1769–1777.

